EVAPORATION OF ZINC

IMPURITIES AND THE EVAPORATION MORPHOLOGY OF ZINC SINGLE CRYSTALS

by

William Alfred John Carson, B.Sc.

A Thesis
Submitted to the School of Graduate Studies
in Partial Fulfilment of the Requirements
for the Degree
Doctor of Philosophy

McMaster University

May 1970

DOCTOR OF PHILOSOPHY (1970)
(Physics)

McMASTER UNIVERSITY
Hamilton, Ontario

TITLE: Impurities and the Evaporation Morphology of Zinc Single Crystals

AUTHOR: William Alfred John Carson, B.Sc. (The Queen's University, Belfast, N. Ireland)

SUPERVISOR: Professor M. B. Ives

NUMBER OF PAGES: (vi); 150

SCOPE AND CONTENTS:

In this thesis the results of optical and scanning electron microscopic investigations of the evaporation morphology of zinc single crystals are presented. Dislocation etch pits developed on (0001) zinc cleavage surfaces. A mechanism is proposed to account for enhanced evaporation at decorated dislocations. The observation of macroledges on pit faces is reported and attributed to impurity-induced bunching of monatomic ledges, the impurities having out-diffused from the bulk. A proposed model for evaporation of faceted surfaces is used to interpret the ledge morphology which developed when samples were evaporated in an oxygen environment. Finally, a correlation between the effects of bulk impurities and gaseous impurities on ledge morphology is demonstrated.

ACKNOWLEDGMENTS

The author is indebted to his supervisor, Dr. M. B. Ives, for suggesting the problem and for continuing guidance during the planning and conduct of this research. He wishes to express his appreciation to Dr. J. S. Kirkaldy and Dr. D. Walton for their help and stimulating discussions during the latter stages of this work.

He wishes to express appreciation to the Dominion Foundries and Steel Ltd., for permitting the use of their scanning electron microscope in this research. He acknowledges especially the assistance and cooperation of Mr. A. Cox of the research staff of this company. Thanks are extended to the staff of McMaster University for their help. In particular, thanks are due to Mrs. M. S. Baskin for assistance in the photographic work; to Mr. T. Bryden for his advice on the design of the U.H.V. system; Mr. D. S. Hodgson for invaluable assistance during the experimental work and Mr. R. Jarochowicz for his help in electron microscopy.

He acknowledges the receipt of a McMaster Graduate Scholarship, an Ontario Fellowship and the financial assistance of the National Research Council of Canada and the U.S. Office of Naval Research (in the form of research grants to Dr. M. B. Ives).

TABLE OF CONTENTS

LIST OF TABLES

LIST OF FIGURES

16. (a) Optical micrograph of evaporation pits when the partial pressure of oxygen was 1.5 x 10^{-7} torr (200x)

(b) S.E.M. of the ledge structure in a pit on the surface shown in (a) (2200x, β=35°)

17. (a) Optical micrograph of evaporation pits when the partial pressure of oxygen was 4.5 x 10^{-7} torr (500x).

(b) S.E.M. of the ledge structure in a pit on the surface shown in (a) (1200x, β=35°)

18. S.E.M. of macrokink "pile-up" in a flat-bottomed pit when oxygen partial pressure was 4.5 x 10^{-7} torr. (a) 600x, β=35°; (b) 1200x, β=35°).

19. S.E.M. of the detailed ledge structure in a point-bottomed pit when the oxygen partial pressure was 4.5 x 10^{-7} torr (12,000x, β=45°).

20. (a) Low magnification S.E.M. of evaporation pits when the oxygen partial pressure was 6.5 x 10^{-7} torr. (240x, β=35°)

(b) S.E.M. showing macrokink-ledge boundaries xx' and yy' in pit A (Fig. 20(a)) (1200x, β=35°).

(c) S.E.M. of detailed ledge structure in the pit shown in (b). (6,000x, β=35°).

21. (a) Interference micrograph of the evaporated surface when the oxygen partial pressure was 8 x 10^{-7} torr (200x).

(b) Interference micrograph of a typical pit on the surface shown in (a). (500x).

(c) and (d) S.E.M. of the mottled ledge structure of a pit, similar to that shown in (b). (c) 2400x, β=35°, (d) 12,000x, β=35°).

CHAPTER 1

INTRODUCTION

The development of a model for the evaporation of crystals has relied on parallel advances in the understanding of equilibrium surface structure, in the extension of these ideas to the structure of an evaporating surface, and in the use of structural surface models to generate mechanistic theories that agree with the phenomenology of evaporation. Numerous theoretical treatments have attempted to predict either the rate of evaporation from or the morphological development of an evaporating crystal surface. The present study was undertaken in order to obtain a better understanding of the latter.

A critical study of previous experimental observations reveals three important factors which control the evaporation morphology, viz. (i) crystal orientation, (ii) undersaturation of the vapor phase, and (iii) the nature and concentration of surface impurities. Although the effects of impurities would seem to be the most difficult to control and study, a thorough knowledge of their role is required if the evaporation mechanism is to be fully understood. In fact, the review in Chapter 2 will show that, in the majority of previous experimental studies, surface impurity effects were of primary importance. However, nothing definitive could be said concerning their nature or their role in evaporation kinetics. Therefore, under these circumstances, many conclusions which have been made about other aspects of the evaporation phenomenon could be called into question.

It would, therefore, seem important to study impurity effects under carefully controlled conditions. To do so, three requirements must be satisfied, (a) the bulk sample must be of high purity, (b) the surface to be studied must be atomically "clean" at the start of the experiment and (c) the environment into which evaporation takes place must be accurately known and be adaptable to strict control. In order to satisfy condition (b) the surface must be prepared in ultra-high vacuum as it is believed that monolayer coverage of a clean surface occurs in less than one second at 10^{-6} torr pressure but takes about 20 minutes at 10^{-9} torr pressure. It was decided that the best method was to cleave a suitable crystal in a vacuum of 10^{-9} torr or less. Zinc was chosen because of the ease by which it can be cleaved on the (0001) plane and also because it produces a high evaporation flux at relatively low temperatures. In order to satisfy condition (c) one must design a vacuum system capable of as low a base pressure as possible and with the ability to monitor the residual gas pressures continuously. This was achieved by the use of standard ultra-high vacuum techniques (1) and the addition of a fast-scan partial pressure analyser.

In the following sections, the results of vacuum evaporation experiments on (0001) zinc cleavage surfaces are presented. The morphological developments are theoretically described by a mechanistic theory which takes into account the presence of surface impurities. Enhanced evaporation at decorated dislocations is explained in terms of an increase in the local chemical potential resulting from a change in the surface curvature at an impurity precipitate. These sections are preceded by a review of evaporation theory and publications pertinent to this study.

CHAPTER 2

PREVIOUS STUDIES OF EVAPORATION PHENOMENA

2.1 Kinetics of Evaporation

The kinetics of evaporation of a pure metal may be described by the relationship

$$J_v = \alpha_v \frac{(p_e - p)}{(2\pi mkT)^{1/2}} \qquad (2.1)$$

where J_v is the evaporation flux in molecules per cm^2, p_e is the equilibrium vapor pressure at the temperature T°K, p is the experimental vapor pressure, m is the molecular mass, k is Boltzmann's constant and α_v is the evaporation coefficient. This expression, with $\alpha_v = 1$, was first proposed by Hertz (2) following an investigation of the evaporation kinetics of mercury in vacuo. Later, Knudsen (3) observed that the evaporation rate for impure mercury was only one-third the theoretical value and in order to allow for departures from ideal kinetics he introduced the evaporation coefficient, $\alpha_v \leq 1$. These ideas were first applied to solids by Langmuir (4) when he used equation (2.1) to determine the vapor pressure of tungsten. A great deal of the subsequent work in evaporation has involved the measurement of α_v for a number of materials. This work has been reviewed in detail by Knacke and Stranski (5) and more recently by Paul (6). Recent theoretical developments have shown α_v to be closely related to the evaporation mechanism and this point is thoroughly discussed in a review by Hirth and Pound (7). In general, however, clean metal surfaces which evaporate monatomically have been found to follow ideal evaporation kinetics.

2.2 Surface Roughening during Evaporation

At approximately the same time as Langmuir's work, many authors reported the observation of distinct features on surfaces which had undergone thermal evaporation. Networks of grain boundary grooves and surface striations were consistently reported. In one of the earliest experiments Rosenhain and Ewan (8) heated polished specimens of copper, silver and zinc in vacuum and observed the formation of grooves at grain boundaries. This effect was attributed to the equilibration of the surface tension of the boundary and the surface energies of the free surfaces.

Of greater interest was the development of surface striations, since it was noted that their formation depended critically on the experimental conditions. Elam (9) heated high purity copper to 900°C in a vacuum of 0.5 torr and observed "etch" features only when visible amounts of cuprous oxide were present. Elam concluded that, in order to obtain surface striations, oxygen must be present at the surface. When electrolytically polished samples of polycrystalline silver were heated to 920°C by Chalmers et al. (10), it was found that {111} facets, separated by high index planes, formed when the experiments were carried out in air or oxygen. On the other hand, no facets resulted when the surrounding medium was either high purity nitrogen or a low (10^{-4} torr) vacuum and in fact previously faceted surfaces were observed to return to their original morphology when heated under these conditions. Chalmers et al. concluded that oxygen adsorption had caused a significant modification in the surface energy anisotropy and that the faceted structure was the configuration of lowest energy. Since the amount of silver which had been evaporated was thought to be small, the mechanism by which the surface re-arrangement occurred was believed to be surface diffusion. However, an uncertainty arises because the vapor pressure of silver is known to increase considerably in the presence of oxygen.

The observations of Chalmers et al. have since been confirmed by a number of workers including Moore (11) and Lowe (12). However, there has been considerable debate concerning their interpretation and the problem will be discussed further in section 2.6.

2.3 Evaporation Etch Pits

In the paper by Chalmers et al., plate 4(d) shows the surface of a polycrystalline silver specimen which had been held at 950°C in vacuum for 1 1/2 hours. On closer examination of the surface, it is possible to observe dark features which appear to be deep pits. No mention was made of these pits and indeed their presence would have been quite unexpected at that time. Later Frank (13) suggested that dislocations which terminate in the surface may play an important role in surface phenomena. He proposed that the vapor growth of crystals at low under-saturations can only be explained if atom attachment occurs preferentially at the perpetuating surface step which is associated with a screw dislocation. However, the correspondence of etch pits to emergent dislocations was initially proposed by Shockley and Read (14) to account for chemical etch patterns observed by Lacombe and Beaujard (15) on high purity aluminum. Since that time, preferential chemical etching at dislocations has been observed on a wide variety of materials and is now firmly established (16).

Cabrera (17) discussed the contribution of the strain energy of the dislocation to the etching process and he showed that there exists a region of undersaturation such that dissolution should proceed preferentially at dislocations as opposed to perfect surfaces. Gilman et al. (18) demonstrated that the preferential etching of lithium fluoride by dilute ferric fluoride solutions agrees in all qualitative detail with Cabrera's conclusions subject to one modification. It is insufficient to preferentially create dissolution steps at dislocation sites to obtain a sharply defined etch pit. It is also necessary to have an ionic species present in the etching solution that adsorbs at advancing dissolution steps and "poisons" the dissolution process. The ferric ions in the aqueous solution serve this function in the etching of lithium fluoride.

Numerous workers have reported the observation of visible evaporation etch pits. However, in many cases any correlation between the pits and dislocations is extremely doubtful. Rather, local breakdown in previously adsorbed surface films often appeared to be the most likely explanation of their origin.

In a rather informative experiment, Winterbottom and Hirth (19) measured the evaporation coefficients and observed the concurrent morphological states of the (111), (110) and (100) surfaces of silver single crystals during vacuum ($\sim 10^{-7}$ torr) evaporation in the temperature range 700-800°C. Their results indicated that the evaporation process could be divided into two distinct time periods. During the initial stages, the evaporation coefficient was significantly less than unity and the surfaces were covered with macroscopic etch pits of density 10^6 cm^{-2} and shape characteristic of the crystallographic symmetry of the surface orientation. There was a tendency for pits to nucleate at macroscopic surface defects such as scratches produced by mechanical polishing. After the initial period, α_v approached unity and the surface developed a hill and valley structure as the pits enlarged and coalesced. The fact that (i) there was no correlation between the pits and chemical etch pits, and (ii) that their lifetime decreased with increasing temperature, indicated that a contaminant surface film must have been controlling the evaporation mechanism. This explanation was tested by shielding the surface whilst sealing the vacuum system (glass) and during the outgassing procedures. As the specimens were then markedly less susceptible to thermal pitting, it was concluded that long chain hydrocarbons, present as a consequence of inadequate trapping of vapor from the oil diffusion pump, poisoned the movement of ledges on the surface.

Similar macroscopic pits were observed by Russell and Haneman (20) on the (111), (110) and (112) surfaces of silicon crystals which had been heated in high vacuum (10^{-9} torr). Between 900 and 1100°C crystallographic macro-pits were observed but above 1250°C a relatively flat surface developed. Russell and Haneman suggested that the observed features were due to an initial surface coverage with SiO_2, as the macroscopic pits disappeared in the same temperature range as that in which other workers had shown that silicon surfaces could be cleaned on the atomic scale by heat-treatment alone.

Examples of thermal etch pits definitely forming at dislocations have mainly been confined to alkali halide evaporation studies. Ejima et al. (21) observed visible etch pits on LiF surfaces which had been heated to 700°C in a vacuum of 10^{-5} torr. By using a standard dislocation etchant, the pits were shown to represent edge dislocations. However, it should be stated that optically observable thermal etch pitting was only possible at intermediate undersaturations and when surface impurity poisons were present, in agreement with the observations of Gilman et al. (18) for chemical etch pit formation. The impurities were due to the residue left by the chemical polish which was employed prior to evaporation.

By means of gold decoration, monatomic steps may be revealed by electron microscopy (22). Recently, Keller (23) has observed spirals which he related to the intersections of screw dislocations with {001} NaCℓ vacuum cleavage surfaces which had been evaporated in high vacuum. The step spacing was ∿ 1000Å, a fact which would explain the difficulty of observing optically any surface structure following free evaporation of clean crystal surfaces.

2.4 Ledge Structure in Etch Pits

Apart from the observation of monatomic steps on alkali halide vacuum cleavage surfaces, evaporation ledge structure, when resolved, is normally found to consist of macroscopic steps.

Votava and Berghezan (24) observed multi-atomic spiral steps on the surfaces of cold rolled bars of electrolytic copper which had been heated to between 900° and 1000°C in a vacuum of from 1 to 4 x 10^{-4} torr.

They believed that these pits were formed at non-coherent, twin boundaries. Impurities, resulting from surface preparation, the crystal bulk and the poor vacuum, almost certainly contributed to the formation of these large steps.

At orientations close to the (0001) pole, Andrade and Randall (25) observed faceted pits on cadmium single crystal wires which had been evaporated at 250°C in a poor vacuum. By means of an optical goniometer they determined the pit faces to be composed of (0001) and $(10\bar{1}1)$ planes, with the latter providing a "step" height of $\sim 1\ \mu m$. They assumed that the evaporating surface had taken up the most stable configuration, in agreement with the theoretical predictions of Stranski et al. (26). The possible effects of environmental or bulk impurities were not considered.

Perhaps the most complete study of macroledge formation is to be found in the related field of chemical dissolution. Ramachandran and Ives (27) used high resolution electron microscopy to reveal the complex structure of surface ledges on {100} cleavages of lithium fluoride crystals after etching in dilute aqueous solutions of ferric chloride. The heights and densities of the surface ledges were studied as a function of the inhibitor content of the etchant, i.e. the ferric ion concentration. The ledge structure within dislocation etch pits was observed to change from a distribution of a small number of high ledges (height $\sim 400\text{Å}$) at low iron (< 1 ppm) concentrations, to a large number of low ledges at higher iron contents. The ferric ion concentration in the etchants varied from 0.1 ppm to 150 ppm. However, the ledge heights were unresolvable at concentrations greater than 2 ppm. It was thought that, when only small quantities of ferric ions were in solution, the flux of ions exchanging between adsorbed surface sites and the solution was small. Under such a condition, it was supposed that step motion would only be impeded at isolated sites. Once a step slowed down, other steps would pile up against it and a ledge form. The etch morphology would then comprise a small number of large ledges. At higher inhibitor contents, more deviations from uniform step arrays can be expected and more ledges will be produced. If the average rate of dissolution was not changed significantly, then these ledges would be smaller in height.

In the limit, at large enough inhibitor contents, a steady modifying action would be achieved, since each part of the dissolving surface is subject to a similar inhibitor flux. This would explain the attainment of smoother etch surfaces of lithium fluoride at high ferric ion concentrations.

Numerous other examples of the observations of macroscopic ledges are to be found in the literature (7). However, apart from a general reference to the presence of impurities, a detailed mechanism for their development and any discussion of their stability are generally absent.

2.5 Effect of Bulk Impurities

The effects of bulk impurities on evaporation kinetics have generally been overlooked. However, they could play an important role, particularly at temperatures close to the melting point when they may diffuse to the surface in sizable amounts. On several occasions it has been observed that a variation in crystal purity has markedly affected the evaporation morphology.

Young and Gwathmey (28) studied the ledge structure on copper single crystal spheres which had been heated to between 900 and 1080°C in a vacuum of 5 to 10 x 10^{-9} torr. Electropolished samples which had been grown from copper of 99.98% purity, developed low-index facets parallel to the (111), (110) and (100) planes around the respective poles. The facets were separated by "wavy" ledges (height ∿ 1 μm.) which they believed to be (111) planes. No indication was given as to how they determined these orientations. On other parts of the sphere, complicated ledge patterns were observed. In contrast, crystals grown from copper of 99.999% purity developed small (height ∿ 0.1 μm.) ledges only within short distances of the (111) and (100) poles. Little change was noted on high purity samples when the undersaturation was reduced by heating in a copper cup of 99.999% purity. However, when a 99.98% copper cup was used, facets and ledges similar to those on 99.98% copper samples were observed. When the samples were re-polished and again evaporated, the original features were observed. They therefore concluded that bulk impurities from the 99.98% copper cup had been transmitted to the evaporating surface where they affected the evaporation mechanism. As equilibrium conditions did not hold, they considered uncertain the possibility that the macroledges had formed in order to minimize the total surface free energy. Rather, the effect of sample purity on ledge height led them to suggest that when isolated steps are slowed down by impurities, macroledges are formed by the pile-up of following monatomic steps. Furthermore, if the "risers" were low index planes, they could be stabilized by surface energy constraints. However, no attempt was made to formulate a detailed model which would explain the dependence of ledge height on the surface impurity concentration.

A second way by which bulk impurities can affect the evaporation kinetics has been reported by Bolgov et al. (29). Thermovacuum etch pits developed on 99.99% nickel polycrystals when heated to between 900°-1050°C in a moderate vacuum for an extended period. As the addition of small amounts of boron promoted the appearance of etch figures in nickel, they suggested that the boron impurity which is only slightly soluble in nickel had segregated to dislocations (30) and caused an increase in the local evaporation rate. Vermilyea (31) had previously predicted that chemical etch pits can not be produced at a dislocation in a metal without prior segregation of impurities at the dislocation. Indeed, Gilman (32) has shown that cadmium decoration of dislocations in zinc single crystals promotes the formation of etch pits in a mixed aqueous solution of CrO_3 and Na_2SO_4. However, the increased reactivity in chemical etching may be an electrochemical effect. Whereas, for evaporation, it is a purely energetic effect. Further theoretical considerations of this problem are therefore necessary.

2.6 Effect of Vapor Phase Contamination

It was mentioned in Section 2.1 that thermal etching of solid surfaces can take place at elevated temperatures in gaseous atmospheres which are mildly reactive with the surface. The crystallography, defect nature, chemical reactivity, composition heterogeneity and the mobility of constitutional, atomic or molecular components of the surface, all contribute to the specific topographic characteristics developed.

A review of the early work on thermal etching has been made by Shuttleworth (33).

It is widely held that the etched surface takes up a configuration of minimum surface free energy, independent of the thermal etching mechanism. The reactive medium is supposed to either increase the surface energy anisotropy or catalyse surface rearrangement. However, in 1960, Hondros and Moore (34) reported that when silver is heated in air to 900°C under equilibrium conditions, a striation free surface results. They argued that, as the surface became smooth when net evaporation was prevented, the faceted surface observed at the same temperature but with net evaporation was not an equilibrium one. They concluded that evaporation was necessary to initiate thermal faceting of silver in an oxygen atmosphere and they postulated that surface striations developed through the movement of evaporation steps across the surface and the formation of a large complex step by the time-dependent impurity adsorption mechanism, postulated by Frank (35). They suggested that oxygen was the adsorbed impurity, because although silver oxide is unstable at 200°C, evidence is available which indicates that oxygen is present in sizable amounts on silver surface at 900°C. Moore's findings have been vigorously debated by Rhead and Mykura (36), and the controversy is discussed in a review article by Moore (37).

In his review, Moore considers several other cases of faceting where considerable evaporation is known to have taken place and suggests that multi-atomic ledges have also developed on these surfaces when a reactive gas adsorbed into the surface, causing monatomic steps to bunch.

It would appear that at elevated temperatures when non-equilibrium conditions exist, thermal etching is primarily an evaporation phenomena. At lower temperatures, where net evaporation is negligible, surface energy control of the surface morphology is probable.

Further systematic studies are required of surface morphologies when "clean" surfaces are heated in ultra-high vacuum and in various partial pressures of various reactive gases. No attempt has been made to study the detailed ledge structure under the same conditions. This may provide significant information concerning the nature of evaporation kinetics.

2.7 Previous Studies on Zinc

Several authors have reported the observation of thermal etch pits on zinc surfaces. Danko and Griest (38) observed deep, highly crystallographic pits on certain grains of polycrystalline zinc beads of unspecified purity which had been melted in a vacuum of 5 x 10^{-6} torr and then held slightly below the melting point for a short period. They suggested that the pits represented screw dislocations although no evidence was presented to substantiate this claim. Plates of twinned zinc monocrystals developed pits when heated by Rais and Bromberg (39) to 400°C at 10^{-4} torr pressure. The pits which showed the hexagonal symmetry of the lattice formed close to macroscopic defects, e.g. at scratches and cleavage steps. However, no details were given of sample preparation or purity which might assist in establishing the source of the pits.

In what has really been the only attempt to make a quantitative study of evaporation mechanisms, Ruff (40) investigated the effects of vapor undersaturation, impurities and crystal dislocations on the evaporation morphology of zinc single crystals. The samples were grown from high purity zinc, cleaved in liquid nitrogen on (0001) planes and then heated to 300°C in a vacuum of 10^{-8} torr. For undersaturation ratios between 0.29 and 0.006, shallow, conical evaporation pits were formed with slopes which increased with increasing undersaturation. As their density was comparable to dislocation densities given by chemical etching methods, Ruff believed that they were associated with dislocations. The effects of oxygen in the vapor phase at partial pressures ranging from 10^{-8} torr to 10^{-5} torr were studied. For a given undersaturation, the pit slope increased with increasing partial pressures. By means of replica electron microscopy Ruff observed that the pit faces consisted of (0001) terraces, separated by multi-atomic ledges (height 50-5,000Å). He found that his results could not be explained by the theories of Hirth and Pound (41,42) but the observed dependence of the conical etch pit slopes on the applied vapor undersaturation could be satisfactorily interpreted according to the theory of Cabrera and Levine (43). However, the present work will show that Ruff's results are representative of a surface which is initially covered by a thin oxide film. Therefore, they should not lend themselves to quantitative interpretation by theories which have been formulated for clean surfaces.

CHAPTER 3

THEORY

3.1 Surface Energy Anisotropy of Solids

Gibbs (44) first showed how thermodynamic quantities could be defined for solid surfaces. Consequently, the Helmholtz free energy per unit area of an n-component system can be written as

$$f_s = \gamma + \sum_{i=1}^{n} \mu_i \Gamma_i \tag{3.1}$$

in terms of the reversible work, γ, required to create a unit area of new surface, the surface excess Γ_i and the chemical potential μ_i of the i^{th} component. Γ_i and μ_i are defined by

$$\Gamma_i = \frac{dN_i}{dA} \quad \text{and} \quad \mu_i = \left(\frac{\partial F}{\partial N_i} \right)_{T,V,N_j,A} \tag{3.2}$$

where N_i represents the number of atoms of the i^{th} species, A the surface area and the thermodynamic symbols have their usual significance. In a one-component system, $f_s = \gamma$, since Γ_i vanishes in this case. For clean surfaces, γ is normally referred to as the surface free energy. Using equation (3.1), it can be shown (45) that

$$\Gamma_i = - \left(\frac{\partial \gamma}{\partial \mu_i} \right)_{T,\mu_j} \tag{3.3}$$

Therefore, the adsorption of component i onto a clean surface, results in a reduction of the surface free energy, γ.

For a crystalline material, γ may depend on the surface orientation. i.e.

$$\gamma = \gamma(\underline{n}) \qquad (3.4)$$

where $\underline{n}$ is the unit outward normal vector at each surface point. $\gamma(\underline{n})$ can be represented by a three-dimensional polar plot. Fig. 1 shows a $< 11\bar{2}0 >$ zone of the polar plot for zinc, based on experimental values of γ reported by Miller et al. (46) for the (0001), $(10\bar{1}1)$ and $(10\bar{1}0)$ orientations. The orientations A, P and B correspond to the pyramidal, prismatic and basal orientations respectively. For values of $\underline{n}$ representing low-index faces, $\frac{d\gamma}{d\theta}$ and/or $\frac{d\gamma}{d\phi}$ become discontinuous, ϕ and θ being the spherical polar co-ordinates. As a result, low index surfaces correspond to grooved minima or cusps in the polar plot, e.g. at A, P and B. These surfaces have been called "singular" surfaces by Frank (48). Orientations close to singular surfaces are called "vicinal" surfaces. The only difference between a vicinal surface and the corresponding singular surface is that it contains steps which account for the surface energy being greater than a singular surface.

3.2 Effect of Adsorption on the Polar Plot

In the presence of adsorbed impurities, the variation of γ with orientation can be substantially different from that observed for clean surfaces. A specific model for adsorption is required before the influence of adsorption on the γ-plot shape can be predicted (49). For example, if surface steps are the locations of strongest binding between impurity and surface, then the γ-plot cusps will be blunted. It may be possible under these circumstances to remove the cusp completely. On the other hand, if the impurity adsorbs most strongly on the low index surface the cusp will be enhanced.

3.3 Stability of Vicinal Surfaces

The total surface free energy E of a body of area A is given by the integral,

$$E = \int_A \gamma(\underline{n})\, dA \qquad (3.5)$$

Gibbs (44) defined the equilibrium shape of a body as that which minimizes the total surface free energy. At elevated temperatures, the atoms in small particles will re-arrange themselves so as to minimize E (50) subject to the constraint that the volume of the body remains unchanged. Herring (51) has suggested that, in an analogous manner, a vicinal surface might break up into a faceted surface containing planar faces of other orientations with lower γ, causing a minimization of the total surface free energy. This phenomenon is subject to the constraint that the average macroscopic orientation does not change.

The conditions for instability with respect to faceting have been discussed in detail by Herring (51). He proposed that "a continuously curved surface with normals in the neighbourhood of OS (Fig. 1) will be stable with respect to formation of a hill-and-valley structure if, and only if, the γ-plot nowhere passes inside the sphere through the origin and tangent at S". The geometric construction of the tangent sphere for the orientation S is illustrated in Fig. 1. From this construction, it can be concluded that the orientation S would break up into (0001) and (10$\bar{1}$1) facets.

The criterion stated in the above paragraph is equivalent to requiring that the following two conditions be satisfied (52):

(a) that the curvature of the tangent sphere be greater than that of the γ-plot at the point S, which guarantees that the point A is stable with respect to infinitesimally small changes in orientation;

(b) that the penetration of the tangent circle by any other point of the two-dimensional γ-plot, i.e. by an inward pointing cusp, does not occur. Gruber (53) has demonstrated that condition (a) can be reduced to the simple statement,

$$(\gamma_S + \frac{\partial^2 \gamma_S}{\partial \Theta^2}) > 0 \qquad (3.6)$$

Normally, $\frac{\partial^2 \gamma_S}{\partial \Theta^2} < 0$ (49). In order to satisfy equation (3.6), it must follow that,

$$\gamma_S > \left| \frac{\partial^2 \gamma_2}{\partial \Theta^2} \right| \qquad (3.7)$$

These ideas are applicable when the surface is in equilibrium with its own vapor. However, it is possible that during non-equilibrium processes a quasi-equilibrium is maintained on the surface and an interpretation of surface morphology in terms of surface free energy control is approximately correct.

3.4 Evaporation Mechanism

A crystal cleaved on a low-index plane is not normally flat on the atomic scale. In order to apply an atomistic approach to crystal evaporation, it is convenient to adopt a model of the crystal surface which was first proposed independently by Kossel (54) and Stranski (55). Any vicinal surface of a crystal can be thought of as being composed of low-index facets separated by ledges of monatomic height. The ledges lie in low-index directions except at kink sites where they are displaced by a monatomic distance. Fig. 2 represents such a model for a cubic crystal.

Kink sites (K) are favored evaporation sites since the atomic bonding is weaker there than at other step sites (S), or at sites in the perfect surface "terrace". Burton et al. (56) have shown that a ledge in a vicinal surface will contain a high density of monatomic kinks due to thermal fluctuations. For a monatomic ledge in a low-index direction, they estimated the mean distance between kinks at a temperature T°K to be

$$\lambda_o = \frac{1}{2} a \{ \exp w/kT + 2 \} \tag{3.8}$$

where w is the energy required to form a kink and a is the lattice constant in the direction of the ledge. For a typical value of $w/kT \sim 2$, the mean kink spacing, $\lambda_o \sim 5a$.

Kossel (54) and Stranski (55) following Gibbs (44) pointed out the importance of monatomic ledges and kinks in the processes of growth and evaporation. Consequently, it has been shown by Burton, Cabrera and Frank (56) in the case of growth and Hirth and Pound (41) in the case of evaporation, both following the general ideas of Volmer (57) that the kinetics involve the steps: (a) adsorption or desorption to the vapor phase from the surface; (b) surface diffusion; and (c) movement into or out of a kink position in a monatomic ledge on the crystal surface, at which the equilibrium concentration of adsorbed atoms is maintained.

3.5 Ledge Sources

Burton et al. (56) have considered the possibility that, at elevated temperatures, statistical fluctuations may produce surface roughening. Their analysis indicates that a close-packed surface in equilibrium with its vapor will remain flat at temperatures below the melting point. Even under non-equilibrium conditions, singular surfaces should not roughen in the case of evaporation, according to the theory of roughening developed by Cahn (58). Therefore, the availability of surface steps will be an important factor in the evaporation process. The possible sources of steps will now be considered.

3.5.1 General Surface Nucleation

On a perfect, low-index surface, steps may be formed by the two-dimensional nucleation of holes in the surface. An example is shown at H in Fig. 2. The free energy change in forming a cylindrical hole of radius r and height h consists of a volume term and a surface term (16):

$$\Delta G = \frac{\pi r^2 h}{\Omega} \Delta\mu_o + 2\pi r h \gamma \qquad (3.9)$$

where Ω is the atomic volume, γ the surface energy for the side of the nucleus and $\Delta\mu_o$ the change of chemical potential for one atom going from the solid to the vapor phase. For ideal or dilute phases, one can use the expression

$$\Delta\mu_o = kT \ln p/p_e \qquad (3.10)$$

Here p_e is the equilibrium vapor pressure and p the actual vapor pressure. In the usual manner, the radius of the critical nucleus, ρ_c, is obtained by requiring $\frac{\partial \Delta G}{\partial r} = 0$. Nuclei larger than this will grow spontaneously, while those smaller will be unstable. One finds that

$$\rho_c = - \Omega\gamma/\Delta\mu_o \qquad (3.11)$$

and the critical activation energy for two-dimensional nucleation on a perfect singular surface is

$$\Delta G^* = - \pi\gamma^2\Omega h/\Delta\mu_o \qquad (3.12)$$

Hirth and Pound (7) have shown that for nucleation to become appreciable, a critical undersaturation given by

$$(p/p_e)_{crit.} = \exp - \{ \frac{\pi\gamma^2\Omega h}{65\ k^2T^2} \} \qquad (3.13)$$

must exist. For a typical solid under normal experimental conditions $p/p_e << 1$.

3.5.2 Nucleation at a Dislocation

The free energy of formation of a nucleus at a dislocation involves a strain energy term in addition to the volume and surface energy term, so that

$$\Delta G = \frac{\pi r^2 h}{\Omega} \Delta\mu_o + 2\pi r h\gamma - hE(r) \qquad (3.14)$$

where E(r) is the strain energy within a cylinder of radius r, per unit length of dislocation line. It is the sum of the elastic strain energy and the core energy, E_c, (59), so that

$$E(r) = \frac{Gb^2}{4\pi\xi} \left[\ell n \left(\frac{r}{r_o}\right) - 1\right] + E_c \qquad (3.15)$$

where G is the elastic shear modulus, b, the Burgers vector, ξ a factor which is one for a screw dislocation and one minus Poisson's ratio for an edge dislocation. Typically, r_o is approximately equal to b. The core energy is difficult to estimate and has therefore been neglected in most calculations. As $E(r) > 0$, it is clear that the activation energy for nucleation will be lower at a dislocation than on a perfect surface.

Maximization of equation (3.14) yields the free energy of formation of the critical nucleus (7).

$$\Delta G^* = - \pi h \gamma^2 \Omega/\Delta\mu_o - (Gb^2 h/4\pi) \ \ell n \ (-\gamma\Omega h/b\Delta\mu_o) \qquad (3.16)$$

Using 3.16, Hirth and Pound (7) have shown that $J_\perp$, the nucleation rate at dislocations, is related to that on a perfect low-index surface by the expression

$$J_\perp/J = - (x_\perp \gamma\Omega h/b\Delta\mu_o) \ \exp \ (Gb^2 h/4\pi kT) \qquad (3.17)$$

where $x_\perp$ is the fraction of surface sites intersected by dislocations. This expression can then be used to calculate the critical undersaturation for appreciable disc nucleation at dislocations, as

$$(p/p_e)_{crit.} = \exp \{(-\pi\gamma^2 \Omega h/k^2 T^2) \ [50 + \ell n \ x_\perp + (\frac{Gb^2 h}{4\pi kT}) \ell n \ \frac{\rho_c}{b}]\} \qquad (3.18)$$

3.5.3 Dislocations with a Screw Component

A screw dislocation (60) emergent, at a crystal surface, provides a step on the surface equal in height to the projection of the Burger's vector on the surface normal. A nucleation process is not required in this case and the removal of one atomic layer leaves the step intact. However, the step must terminate at the dislocation and, consequently, during evaporation will wind itself into a spiral. The radius of curvature at the centre of the spiral must not be less than that of the cylindrical void in equilibrium with the undersaturated vapor phase. On taking this constraint into account, Cabrera and Levine (43) showed that the spacing, λ, of ledges near the centre of the spiral is

$$\lambda = 19\,\rho_c \tag{3.19}$$

where ρ_c, the critical radius of a two-dimensional nucleus on the crystal surface, is given by equation 3.11. Therefore, the pit slope in this region is $h/19\,\rho_c$ where h is the step height. In order that a detectable pit is formed, the step spacing $\lambda_1 = 19\,\rho_c$ must be small. As $\rho_c = \frac{\gamma\Omega}{kT\ell np/\rho_o}$, it follows that high undersaturations are required to produce observable pit formation at screw dislocations.

3.5.4 Crystal Edges

Ledges arising at "unprotected" crystal edges may play an important role in evaporation kinetics (41). Evidence of such a mechanism has been provided by Hudson and Sears (61) who studied the evaporation of zinc whiskers at undersaturation ratios $p/p_e \geq 0.99999$. If the crystal edge is composed of low-index surfaces, a nucleation problem may be involved. In the present work the crystal edges were protected by an electrolytic plating.

3.6 Evaporation Kinetics

Hirth and Pound (41) have considered the ledge configuration on surfaces of perfect crystals when evaporation takes place by the advance of monatomic steps emanating from crystal edges. They assumed a stepwise evaporation mechanism, i.e. removal of atoms from kink sites, surface diffusion on a low-index terrace and desorption into the vapor phase. Desorption into the vapor phase was assumed to be rate controlling.

As the concentration of kinks in ledges is appreciable at elevated temperatures, ledges act as continuous sources of atoms. Thus, the equilibrium concentration of adsorbed atoms (adatoms) is maintained at the ledge. Under non-equilibrium conditions, desorption of adatoms results in a surface diffusion flux away from the ledges. Invoking a condition of continuity, the divergence of this flux equals the flux of atoms evaporating into the vapor phase. Solving the differential equation corresponding to the continuity condition, Hirth and Pound (41) show that ledges arising at crystal edges, accelerate away from the edge and finally approach a limiting velocity asymptotically. The terminal spacing of the ledges is

$$\lambda = 6\,\bar{X} \qquad (3.20)$$

where $\bar{X}$ is the mean free path for random walk of an adsorbed atom on the close-packed terrace. It is given by

$$\bar{X} = (2D_s\tau)^{1/2} = a \exp\left\{ (W_s - U_s)/_{2kT} \right\} \qquad (3.21)$$

where D_s is the coefficient of surface diffusion, $\tau = \nu^{-1} \exp(W_s/kT)$ the mean lifetime of an adatom before being evaporated, W_s is the evaporation energy from the surface to the vapor, U_s is the activation energy for surface diffusion, a is the interatomic spacing in the surface. and ν is the vibration frequency of adatoms. It is significant that the ledge spacing, λ, is independent of undersaturation. In this limiting case, Hirth and Pound (41) deduced the evaporation coefficient to be

$$\alpha = \frac{1}{3} + \frac{2}{3}\, p/p_e \tag{3.22}$$

For free evaporation, $p = 0$ and so $\alpha = \frac{1}{3}$. In the perturbed region close to the crystal edge where the step spacing, $d < 6\,\bar{X}$, the evaporation coefficient is in the range

$$\frac{1}{3} \leq \alpha \leq 1 \tag{3.23}$$

The ledge spacing attains its terminal value at a distance approximately $60\,\bar{X}$ from the crystal edge.

Hirth and Pound (42) have also shown how the above theory may be used to describe steps arising at other ledge sources in the surface. In general, if $d < 6\,\bar{X}$ for ledges emanating from any source in the surface, they accelerate to the steady state velocity as evaporation proceeds. In this case, an evaporation pit would form with a surface slope which decreases towards the limiting value $h/6\,\bar{X}$ far from the source. On the other hand, if $d > 6\,\bar{X}$, the ledges move outward with a steady velocity, maintaining a constant spacing. Application of these ideas to a screw dislocation step source shows that if $19\rho_c < 6\,\bar{X}$, the evaporation coefficient of the central portion of the spiral will be greater than $\frac{1}{3}$. Pronounced evaporation should, therefore, take place in this region and a pit will form.

For steps produced by two-dimensional nucleation at dislocations, the initial step spacing will be controlled by the diffusion fields associated with the ledges. As the first ledge moves away from the source, its diffusion field will increase the adatom concentration at the source, thus making the next nucleation process more difficult. Cabrera (62) considered this "back-stress" effect and estimated that the previous step must move out a distance of 10^6 atomic spacings before another cylindrical void could form. This would result in an undetectable evaporation feature, since the crystal surface would be nearly flat. These ideas are modified considerably when impurities are present.

3.7 Surface Impurity Effects

Impurities, present in small amounts have a profound effect on evaporation and crystal dissolution (18, 63). They may adsorb from the vapor onto the surface dynamically during evaporation, may be already adsorbed prior to the experiment, may adsorb dynamically by diffusion from within the crystal or may be uncovered in the course of evaporation. Unfortunately, their role in the modified evaporation kinetics is poorly understood and attempts to provide a suitable explanation are at best speculative.

There are two extreme types of impurities that can be considered, either immobile or completely mobile. Immobile impurities are assumed to be adsorbed permanently at points where they strike the surface. A moving step will then be required to squeeze through between the impurity positions on the surface. It is obvious that, if a pair of impurities are closer than 2 ρ_c, the step will be effectively blocked. Cabrera and Vermilyea (64) have given an estimate of the effect on step velocities, finding that

$$v = v_\infty \; (1 - 2 \; \rho_c/d) \tag{3.24}$$

where v_∞ is the step velocity of a straight ledge on a clean surface and d is the mean impurity spacing. This relationship predicts a critical undersaturation for step motion on a contaminated surface. The critical condition is

$$2 \; \rho_c = d \tag{3.25}$$

Substituting $\rho_c = \gamma\Omega/kT \; \ell n \; p/p_e$ from equation (3.11) gives

$$\left(\frac{p}{p_e}\right)_{crit.} = \exp\left(\frac{-2\gamma\Omega}{kTd}\right) \tag{3.26}$$

In a more exact treatment of this problem, using statistical mechanics, a non-zero, though rapidly decreasing, velocity is found for $d < 2 \; \rho_c$.

The formation of macroscopic ledges is attributed in many cases to impurity induced bunching of monatomic ledges. Cabrera and Vermilyea (64) have suggested that macroledge formation will result from the "pile-up" of steps as they proceed into a contaminated region where they are blocked by the mechanism described above. Frank (35) has considered the motion of a train of equally spaced, parallel ledges on an evaporating surface when there is time-dependent adsorption of impurities onto the surface. If the assumption is made that when a step passes it leaves a clean surface, then the density of adsorption met by an oncoming step is an increasing function of the time elapsed since the passage of the previous step. If one step is allowed to lag a little behind its regular position, it meets a dirtier surface and is retarded. The following step suffers diminished impurity retardation and catches up with the retarded step. The united pair lag increasingly behind the preceding steps and more steps are absorbed to form a multiatomic ledge.

In the case of completely mobile adsorbed impurities, the concentration along a ledge is in equilibrium with the impurity concentration. The principal effect on step motion would be caused by impurity adsorption at kink sites where they would interfere with the removal of atoms from those sites. This would result in an appreciable lowering of the step velocity. Sears (65) has pointed out that in order for this to happen, complete step coverage is necessary, otherwise new kinks will form as a result of thermal fluctuations. Presumably, there is a small reduction in step velocity up to complete step coverage, when a sharp decrease in step velocity would be expected. Cabrera (62) has suggested that the diffusion field near a poisoned step will be considerably modified, resulting in a reduction or the elimination of the "back stress" effect on two-dimensional nucleation mentioned earlier.

A number of authors (65,66) have pointed out that as a consequence of the decrease in surface energy, γ, due to impurity adsorption, the step spacing close to the centre of a screw dislocation spiral which is directly proportional to the surface energy should decrease, producing an increase in the pit slope.

It has also been suggested that (65,66) pit nucleation at non-spiral dislocations would be less difficult if the surface energy was lowered. According to Cabrera (62) the impurities must be extremely mobile so that they can be adsorbed during the time that the critical nucleus is being formed. He believed that because of their high mobility, the same impurities could not pin steps effectively and hence the "back-stress" effect would not be eliminated. In the case of a single impurity system, it is not expected that both mechanisms are operative.

3.8 Vapor Pressure of Alloys

Consider a binary alloy in equilibrium with its vapor phase. In equilibrium with each alloy phase there exists a gaseous phase which comprises the partial pressures of the vapors of each component of the alloy . The partial pressure of each component gaseous species changes with temperature and composition of the alloy, maintaining equilibrium between the vapor and solid phases. The vapor pressure of a species A, when there is a dilute solution of an impurity B in A, is lower than the vapor pressure of pure A. The introduction of B lowers the chemical potential by an amount (67)

$$\Delta\mu = RT \ \ell n \ a_A \qquad (3.27)$$

where R is the gas constant, T the temperature in °K and a_A is the activity of the component A in the solid phase of given composition. By definition (68) ,

$$a_A = p_A/p_A^{\circ} \qquad (3.28)$$

where p_A^o and p_A are the equilibrium vapor pressures of pure A and A in the alloy respectively. When A is a dilute solution in B, a_A is directly proportional to the fractional concentration of A. However, a_A is really an empirical parameter which is experimentally determined.

In summary, the partial vapor pressure of a component in equilibrium with an alloy will be lower than that of the pure component by a factor a_A. Equation (3.27) can be applied to the alloy base constituent or the added impurity.

3.9 Vapor Pressure of Curved Surfaces

In 1871, Thompson (69) showed that the vapor pressure of a small droplet exceeded that of a plane surface of the same liquid. Herring (70) has considered the equivalent change in vapor pressure for solids, allowing for the variation of surface free energy with orientation. He showed that the chemical potential, μ, on a convex segment of surface is related to its value, μ_o, on a planar segment by

$$\mu - \mu_o = \Omega \{ K_1 (\gamma + \frac{d^2\gamma}{d\phi_1}) + K_2 (\gamma + \frac{d^2\gamma}{d\phi_2}) \} \qquad (3.29)$$

where Ω is the atomic volume, $K_1 = \frac{1}{R_1}$ and $K_2 = \frac{1}{R_2}$ represent the principal curvatures of the surface and the ϕ's are angles measured in planes defining the principal sections of the surface convexity. Close to low index orientations, the second derivative of γ with respect to these angles does not exist and this expression is no longer valid.

If γ is isotropic, the angular derivatives are zero and equation (3.29) reduces to the classical Gibbs-Thompson formula:

$$\mu - \mu_o = \gamma\Omega \left(\frac{1}{R_1} + \frac{1}{R_2}\right) \qquad (3.30)$$

As $\Delta\mu = kT \ln p/p_o$, where p and p_o are the vapor pressures of the curved and flat surfaces respectively, equation (3.30) becomes, on rearranging

$$p/p_o = \exp \left(\frac{2\gamma\Omega}{RkT}\right) \qquad (3.31)$$

if $R_1 = R_2 = R$, as in the case of a spherical shape.

The Gibbs-Thompson relationship has already been encountered in another context, viz., the expression for the size of a critical nucleus (equation 3.11). In that instance, the concave curvature of the step lowers the chemical potential at the step, and consequently, a vapor undersaturation is required for evaporation.

3.10 Segregation of Impurities to Dislocations

The crystalline volume around a dislocation is in a state of stress. These stresses can be relieved by a suitable arrangement of solute impurity atoms. The interaction energy between the solute atoms and the dislocation was first calculated by Cottrell and Bilby (71). Their original solution has since been modified by Bilby (72).

In the Bilby-Cottrell model, the solute atom behaves as an elastic inclusion in the solid solution and gives rise to a permanent elastic strain field. This strain field, in turn, interacts with the strain field of a dislocation. In effect, the interaction arises because the elastic strain energy of a solid containing solute atoms and dislocations is decreased when a solute atom migrates from a position of misfit in the bulk material to a position of better accommodation in the region of imperfect packing surrounding a dislocation.

The solute atom-dislocation interaction can then be analysed in terms of isotropic elasticity theory. The solute atom is simulated by an elastic sphere of radius r, imbedded in a spherical cavity of radius r_o in an elastic matrix. Since a spherical elastic occlusion causes radial displacements only, the elastic stress field of the solute atom interacts with the hydrostatic components of the dislocation stress field, ie., the solute atom will only interact with the edge component. The elastic work performed by the forces of the dislocation stress field acting through the displacements of the solute atom strain field gives rise to the interaction energy, U . Bilby (72) calculated U to be

$$U = 4\ Gb\ \varepsilon\ r_o^3 \frac{\sin\alpha}{R} \qquad (3.32)$$

where R and α are the magnitude of the radial vector protracting from the dislocation and the angle between the slip plane and the radius vector respectively, G is the elastic shear modulus, b is the Burgers vector of the edge dislocation and $\varepsilon = (r' - r_o)/r_o$ is the size misfit parameter. r' is the effective radius of the segregated atom.

If the solute atom is to interact with the screw component of a dislocation, it must produce a non-spherical distortion in the bulk matrix. There is evidence to suggest that solute atoms do, in fact, migrate to screw dislocations (73). In these cases, the atoms in question must produce asymmetric distortions in the lattice.

For a large solute atom, close to an edge dislocation, U is positive for $\pi > \alpha > 0$, i.e. on the side of the extra half-plane, and negative on the other side. Thus a large atom is repelled from the compressed region of the dislocation and attracted into the expanded region. $|U|$ is a maximum when α is $\pi/2$ or $3\pi/2$.

When time is allowed for the necessary diffusion, these interactions cause the solute atoms to segregate around stationary dislocations in equilibrium distributions. Cottrell (74) has shown that, at a point where the interaction energy is U, the equilibrium concentration is

$$C = C_o \exp (U/kT) \qquad (3.33)$$

where C_o is the average solute concentration. This formula is valid provided the concentration at any point is not enough to alter appreciably the value of U at that point. If $U_{Max} >> kT$ at the aging temperature, the atmosphere becomes saturated. When this happens the Maxwellian distribution of equation (3.33) is no longer valid.

It is interesting to estimate the value of U_{Max} for a typical impurity in zinc, i.e. lead. When the approximation is made that $r' \simeq r_{Pb} = 1.75\mathring{A}$, $r_o \simeq r_{Zn} = 1.33\mathring{A}$, (47), ε is 0.315 for the Pb-Zn system. Then, using the value $G = 3.8 \times 10^{11}$ dynes. cm^{-2}, one finds that $U = 0.7$ eV at the point $\alpha = \frac{3}{2}\pi$, $R = b$. This value is probably too high because equation (3.32) was obtained by using linear elasticity theory. However, it is correct in order of magnitude and agrees well with the equivalent calculations for systems where segregation at dislocations has been observed (30). Therefore, there should have been appreciable impurity segregation at "grown-in" dislocations in the zinc crystals which were used.

3.11 Crystallography of Zinc

Zinc crystallizes in the "hexagonal close-packed" structure with a c/a ratio of 1.85. By comparison, a close packed arrangement of hard spheres in contact has a c/a ratio of 1.63. Nevertheless, the close-packed lattice itself can be used to illustrate some of the structural properties of zinc.

An examination of the atomic positions in (0001) planes (Fig. 52) reveals that surface steps might lie in $\langle 11\bar{2}0 \rangle$ directions, with kinks in such steps lying in some other $\langle 11\bar{2}0 \rangle$ direction. The atom in the kink position would have six nearest neighbors, whilst the step positions would have seven nearest neighbors. By comparison, a perfect surface position would have nine nearest neighbours. It is possible to construct other straight steps such as $\langle 1\bar{1}00 \rangle$. The atoms in this step, having six nearest neighbors, would be expected to evaporate as readily as those in the kink sites of $\langle 11\bar{2}0 \rangle$ steps. After sufficient evaporation, this step would move into a $\langle 11\bar{2}0 \rangle$ direction, which would be stable.

CHAPTER 4

EXPERIMENTAL APPARATUS

4.1 The Ultra-High-Vacuum System

An all-metal ultra-high vacuum (U.H.V.) system was designed and constructed using, in large part, commercially available components. Schematic diagrams and a photographic view of the system are shown in Figs. 3 to 8.

Since it was desirable that all possible sources of contamination should be kept to a minimum, a 140 liters/sec "sputter" ion pump* "P" (Fig. 3) was employed in conjunction with cryogenic roughing pumps[+] "C" (Fig. 8), thus eliminating the use of working fluids and moving parts which may introduce contaminant vapors into the vacuum chamber. One roughing pump was used to reduce the pressure to 1 torr. It was then valved off and the second sorption pump introduced. The pressure would quickly fall to 3×10^{-3} torr and at this point the ion pump could be started.

Liquid nitrogen sorption pumps rapidly remove all gases with liquification temperatures above or near 78°K. However, those gases not in this category, particularly neon and helium, are not adsorbed to any significant extent, and consequently they constitute the major residual species in the vacuum chamber. Therefore, if a two-stage roughing technique is employed, the non-condensible gases are swept into the

---

* Varian Model No. 912-7000

[+] Varian Model No. 941-6001

sorption pump during the initial air inflow and are trapped by closing a block value* "B" (Fig. 8) before the pressure is reduced to a level which would permit the uncondensed gases to diffuse back into the vacuum chamber.

T (Fig. 4) is a 50 liters/sec. water-cooled titanium sublimation pump[+], which has a high pumping speed for active gases, such as nitrogen and oxygen. The operating filament current was 49 amps. Although the sublimation pump can be efficiently employed at all pressures below 10^{-2} torr., in the study of "clean" surfaces it is normally only used at low pressures to getter chemically active gases before an experimental run.

During the roughing stage of pump-down, pressures in the range 1 to 10^{-3} torr. were measured by a thermocouple gauge** "T.C." (Fig. 8), positioned on the low vacuum side of the U.H.V. stainless steel valve[++] "V" which isolated the roughing system from the ultra-high vacuum unit. Gas pressures between 10^{-3} torr. and 2×10^{-12} torr. were measured with a Bayard-Alpert type ionization gauge[†] "G" (Fig. 3) which was bakeable to 550°C. The gauge was furnished with a calibrated response to several different gases. However, it is convenient to refer to "equivalent nitrogen pressures" in the absence of a specific knowledge concerning the gases present. This policy will be followed here, except in those cases in which a specific gas was wholly responsible for the background pressure

---

* General Electric 22HV125

[+] Varian Model No. 916-0011

** Varian Model No. 952-5007

[++] Varian Model No. 971-7004

[†] Varian Model No. 951-5027

A mass spectrometer-type residual gas analyser* M (Fig. 3), bakeable to 300°C, was incorporated into the vacuum system. The total mass range 2 to 300 A.M.U. was covered in two increments, viz. 2 to 12 A.M.U. and 12 to 300 A.M.U., with unit resolution+ at 75 A.M.U. Each mass constituent could be scanned by varying the ion acceleration voltage, since the magnetic field remained fixed. Three different operational modes were available, viz.:

(i) the mass range could be scanned manually and the mass peaks read on an electrometer;

(ii) the mass-spectrum could be printed-out on a Leeds and Northrup 3-decade recorder as the mass range was scanned automatically; and

(iii) the mass spectrum could be observed on an oscilloscope while the time base of the oscilloscope was used to control the ion accelerating voltage and hence sweep through the mass range.

For accurate determination of residual gas pressures, mode (ii) was used. The recorder covered three logarithmic scales: 0-1 mV, 1-10mV and 10-100 mV, and as each scale was divided into equally spaced linear divisions, smaller output signals were more readily studied, thus increasing the sensitivity of the instrument. The addition of an electron multiplier to the ion current collector stage, permits the measurement of residual gas pressures in the low 10^{-13} range.

---

* Vacuum Electronics, Type GA4

\+ Two peaks are said to be just resolved if the distance from the base line to the valley between them is equal to 1% of the sum of their heights.

As the chart read-out times in mode (ii) were of the order of minutes, when instantaneous changes in partial pressures were required mode (iii) was used. The instrument could be set so as to follow the changes in a single mass peak, a range of peaks or the entire mass spectrum. Obtaining permanent records of transient effects was the major difficulty in this operational mode.

The response of the instrument to each gas must be known in order to convert ion currents at the collector electrode to partial pressure readings. In the absence of this knowledge, it is conventional to use the calibrated response to nitrogen and once more refer to "equivalent nitrogen pressures". Recent investigations by Bailey (75) indicate that this approach is quite acceptable when only the approximate partial pressures are needed.

4.2 The Evaporation Chamber

One of the principal objectives of the present study was to prepare a clean low-index surface in ultra-high vacuum. As zinc single crystals cleave without difficulty on the (0001) plane, a vacuum chamber was designed to permit cleavage *in situ* of large zinc single crystals. The main features of the chamber are shown in Fig. 4.

The chamber itself was constructed from a cylindrical (6" diameter, 13" long) stainless steel nipple* which was modified by the addition of eight 1 1/2" outside diameter tubular feedthroughs, fitted with "conflat" flanges+. All working components in the vacuum system were flange-mounted.

---

* Varian Model No. 952-5055

+ Varian Model No. 954-5071

As a result, they could be removed for maintenance or re-design with a minimum of inconvenience, with the vacuum only broken for a short period of time.

A 6" diameter, flange-mounted, type 7056 glass viewing port* "W" (Fig. 4) was used to "close-off" the vacuum chamber. This permitted the observation of all events which occurred inside the vacuum system. In particular, one could determine if a successful crystal cleavage had been achieved or visually observe evaporation from the sample. However, its principal purpose was to facilitate measurement of the specimen temperature by an external pyrometer.

In order to cleave the crystals in vacuum, it was necessary to produce a sudden linear impulse within the vacuum chamber. Because a suitable device was not commercially available, a unit capable of external manipulation was designed and constructed in the laboratory (Fig. 5). All components were constructed with type 304L stainless steel and all permanent seals, "W", were argon arc-welded. High quality stainless steel bellows+, "B" were mounted on a conflat flange "C" as shown in Fig. 5. Linear motion was effected by a "drive-rod", R, which was welded to the top end of the bellows. Since the bellows would collapse under vacuum, they were supported in an extended position by the cylinders "S_1", "S_2" and pins "P". The bellows were released and motion introduced to the vacuum system when the support pins "P" were aligned with guidance slots in the upper cylinder, "S_1".

---

* Varian Model No. 954-5129

\+ Flexible Metal Hose Part No. 460-150-030

The crystal holder (Fig. 6) was machined from a type 304L stainless steel rod and was screw-mounted on a three-quarter inch thick, conflat flange "C", suitable gas release holes having been machined to prevent the formation of pockets which could give rise to virtual leaks. The crystal mount "M" (Fig. 6) was also made of stainless steel and attached to the support by a threaded connection. The crystal itself was held in a pyrophyllite casing, "P". The use of pyrophyllite which is a poor thermal conductor, permitted good thermal insulation of the sample. A clamping screw "S" held the sample firmly in place.

A notch was cut in the sample so that, when the sample was in position, the notch coincided with the front face of the sample holder. Therefore, when the cleavage tool was released and allowed to push on the sample (as shown by the arrow in Fig. 4), the crystal broke at the plane section defined by the notch. Cleavage of zinc single crystals on (0001) is relatively easy at liquid nitrogen temperature. However, preliminary experiments with another vacuum system indicated that vacuum cleavage at room temperature could be effected without appreciable deformation. This room temperature cleaving was adopted in the present work, permitting a simplified crystal holder design.

After early attempts to heat the sample by a focused infra-red heating lamp external to the chamber had proven unsatisfactory, it was decided that the most efficient heating method was by electron bombardment of the single side opposite the prepared face. For this purpose, a simple electron gun, "G" (Fig. 4) was constructed in the laboratory.

Two stainless steel current pins were mounted on a pyrophyllite insulation disc and a 0.02 inch diameter tungsten filament* spot-welded to the pins. The filament holder was then placed in a stainless steel shield. The shield was held at the same potential as the filament, thus producing some focusing of the electron beam. The gun was supported by current leads of heavy gauge copper, which were bent so as to position the gun exactly behind the sample (Fig. 3). The electron gun operating power, which was provided by a two kilovolt D.C. power supply, was transmitted into the vacuum chamber via a flange-mounted, dual medium-current U.H.V. feedthrough+.

The entire vacuum system rested on a specially designed aluminum table as shown in Fig. 7.

An essential procedure in ultra-high vacuum technique is a high temperature bakeout of the vacuum system, to drive off adsorbed gases from the chamber walls and internal parts. A simple oven construction, suggested by Prescott (76) was built so that the equipment enclosed by the dashed lines in Fig. 3 could be baked-out.

The oven was constructed from pieces of 0.08 inch thick "Fiberfrax" paper†, cut according to the oven design (each wall being constructed separately) and covered on both sides with aluminum foil. To complete the oven, the individual walls were stapled together. The aluminum table was also covered with similar sheets.

---

[*] Varian Model No. 980-1014

[+] Varian Model No. 954-5008.

[†] Obtained from Carborundum Company, Niagara Falls, N. Y., U. S. A.

The heating elements were infra-red quartz lamps*, 3/8 inch diameter and 19 3/4 inch long. With two of the lamps connected in parallel and placed close to the bottom of the oven, a fairly uniform oven temperature of 300°C could be attained within a short period of time. The bake-out temperature was measured with an iron-constantin thermocouple and its output voltage was used as the input signal for a Honeywell Pyr-O-vane+ temperature control unit, which maintained the required oven temperature by turning the lamps on and off in appropriate time cycles.

4.3 The Gas-Leak System

Part of the study was to investigate how the evaporation mechanism is modified in the presence of vapor phase impurity, e.g. oxygen. For this purpose, the gas-leak system shown schematically in Fig. 8 was assembled. By incorporating the roughing stage of the ultra-high vacuum system into the gas-leak system, the sorption pumps "C" could be used either to "rough" the ultra-high vacuum unit with the valves L and N_2 closed but V open or to evacuate the gas-leak system during a gas-leak experiment. The roughing system was constructed from commercially available stainless steel parts and the gas lines were constructed with 1/4 inch outside diameter copper tubing.

---

[*] Canadian General Electric Company, Model No. 1600T3/VB.

[+] Model No. 105C4-VS-24.

In Fig. 8, N_1 and N_2 represent brass needle valves* and L represents an U.H.V. variable leak valve+ which could be operated either full-closed or to give gas leak rates down to 10^{-10} torr. liters/sec. The other components have been described above.

During a typical gas-leak experiment, the entire unit, on the low vacuum side of L and V, would be evacuated using one of the cryogenic pumps, flushed with oxygen and re-evacuated. Then with N_2 closed, oxygen at atmospheric pressure was allowed into the reduced volume and finally admitted, via L, into the ultra-high vacuum chamber. The leak-rate was manually adjusted to give the required oxygen partial pressure in the vacuum chamber, whilst pumping with the ion pump.

4.4 The D.C. Power Supply

A simple double wave rectification unit was designed to provide the D.C. power supply for the electron gun. The electrical circuitry is shown in Fig. 9.

The design permitted the filament to be maintained at a negative potential with respect to the sample, which was earthed. The filament current could be varied from zero to 25 amps. by the Variac VT8 and the high voltage output from zero to 2KV by the Variac VT20. The voltage ripple on the latter was negligible.

The complete unit was mounted in a mobile cabinet, seen in the foreground of Fig. 7.

---

* Nupro, Model No. B-4H

\+ Varian Model No. 951-5100

4.5 Surface Temperature Measurement

When an atomically clean surface is prepared by cleavage in vacuum, measurement of the surface temperature at a later time is extremely difficult.

The obvious solution is to perform a calibration experiment in which a thermocouple is attached to a pre-cleaved sample and the surface temperature measured as a function of time when the geometrical position and the electrical characteristics of the electron gun are equivalent to those which exist during an actual evaporation run. However, the relatively low melting point of zinc makes it very difficult to attach thermocouples to a zinc surface by conventional techniques, e.g. spot welding or silver soldering. Therefore, a chromel-alumel thermocouple was silver soldered to the surface of an iron sample. This allowed an approximate measurement of the heating capacity of the gun, but as an accurate technique of determining surface temperatures, it was less than satisfactory.

In order to achieve a more accurate knowledge of the temperature, an IRCON infra-red pyrometer* was used. This instrument is capable of measuring surface temperatures with an accuracy of ± 10°C above 120°C, providing the emissivity of the surface is known. An emissivity value of 0.07, for an oxide-free zinc surface, was supplied by the manufacturer and this value was used in the present work.

When the emissivity scale in the control unit was set at the correct value for the surface under study, the surface temperature may

---

* IRCON Model No. 300C

be read directly from a meter in the control unit. However, as the lowest value on the scale was 0.2, an extrapolation, using Wien's law, had to be made in order to calculate the true surface temperature from the reading on the meter.

The 300C IRCON pyrometer utilises the infra-red radiation emitted in the wavelength range 2.0 to 2.6 μm. The transmission coefficient of the glass window was 93 per cent. Therefore, a correction which takes this into account must be made when computing the surface temperature.

A further problem arose in that radiation from the electron gun filament was "picked up" by the infra-red detector, giving a continuous background reading on the meter. The effect was minimised by attaching a radiation shield to the sample holder, so that most of the radiation was reflected away from the detector. The remainder was corrected for by a calculation. However, as the shield interfered with the cleavage event, it could only be employed when a pre-cleaved sample was used. Hence, calibration experiments were performed with several pre-cleaved samples and a mean value, 390°C, taken as the normal experimental temperature, assuming that the same temperature characteristics hold with a vacuum cleaved sample under similar experimental conditions.

With the detector placed twelve inches from the surface, the pyrometer read the average temperature of an area approximately 0.17 inches diameter. A small circle, visible in the eyepiece of the detector, was used to locate this area and great care was taken that it did not include any cleavage steps or other macroscopic defects which might cause a further inaccuracy in the surface temperature measurements.

In view of the various corrections, the above temperature could at best be taken as accurate to ± 15°C. If the purpose of the present study had been to measure the evaporation coefficient of zinc, this uncertainty could not be tolerated. However, as the experimental strategy was to make a qualitative study of evaporation morphologies under various environmental conditons, an accuracy of ± 15°C in the temperature measurement was considered acceptable, providing the electron gun was operated in an identical fashion during each evaporation run. The consistency and reproducibility of the observations which are described in Chapter 6 would indicate that this assumption was justified.

As the sample temperature approached 390°C, the flux of evaporating zinc became appreciable and the glass viewing port was quickly coated with a thin film of condensed zinc. Therefore, the infra-red pyrometer could no longer be employed.

This problem was overcome by using the thermocouple temperature calibration method to determine the values of filament current and accelerating voltage which were necessary to maintain a constant surface temperature throughout the evaporation period (Section 5.3).

The thermocouple calibration technique played an invaluable role in permitting frequent checks on the operating characteristics of the electron gun, e.g. if the position of the gun with respect to the sample had changed, a re-calibration with the infra-red pyrometer was necessary.

The calibration method was also used to measure the cooling rate of the samples after the electron gun was switched off. The rate of cooling was slower than was desirable, although no surface features, which might have developed during cooling, were observed. An attempt was made to increase the cooling rate by introducing nitrogen to atmospheric pressure on completion of the evaporation run. However, this procedure distinctly affected the observed surface morphology.

CHAPTER 5

EXPERIMENTAL PROCEDURES

5.1 Sample Preparation

Using the apparatus shown in Fig. 10, cylindrical 3/8 inch diameter zinc mono-crystals were grown from the melt by the Bridgman method. The crystal growing unit consisted of a water-cooled brass base "B" which supported a vertical length of 5/8 inch diameter vycor tubing "B", a vacuum seal being effected by the rubber O-rings "O". A valved outlet at the top of the vycor tubing,"V" allowed either the maintenance of a low vacuum in the system or the passage of a suitable gas during growth.

The crystals were grown in moulds, machined from 1/2 inch diameter Union Carbide ECV graphite rods. "F" was an external resistance furnace which was driven vertically at a constant speed of 7 1/2 inches/hr by a small electric motor. It was assumed that the crystal growth rate also had this value.

Since it was important that the (0001) crystal axis was parallel to the cylindrical sample axis, all crystals were grown from a seed with this orientation. The starting material was obtained in the form of 3/8 inch diameter polycrystalline rods, with a stated purity of 99.999% zinc, from Cominco Limited, Montreal, Quebec. Therefore, a crystal could be grown from the as-received rods, thus eliminating the possible introduction of further impurities by extra preparatory processes.

For crystal growth, a suitable seed "S" was placed in the bottom of the mould "M", with a 2 inch length of polycrystalline zinc "P" on top.

The system was evacuated to 10^{-3} torr, flushed with normal grade nitrogen and re-evacuated. A slow flow of nitrogen, which was released through dibutyl thaline trap, was maintained during growth. The furnace was started from a pre-determined position which allowed melting to commence at approximately 1/4 inch below the single crystal-polycrystal interface. In this way, an orientated zinc single crystal was obtained. When the oven had traversed the mould, all power supplies were switched off and the crystal allowed to cool to room temperature in an increased flow of nitrogen. When the combined crystal and seed was removed from the mould, it was given a deep etch in dilute $HC\ell$, to remove any surface contamination. Then, by cleavage in liquid nitrogen, the seed was separated and made available for re-use.

In order that gas evolution from the sample during an evaporation run was minimized, it was necessary to previously outgas the sample at a temperature slightly greater than the experimental temperature. However, this is impossible without appreciable evaporation of zinc. Therefore, the crystals were electroplated with a very thin nickel plate. Before plating, the crystals (length ≃ 1 1/2 inches) were mechanically polished on all surfaces and a shallow cleavage notch cut 1/2 inch from each end.

A qualitative spectrographic analysis of several samples was obtained. The principal impurities detected are listed in Table 1 along with their solubilities in zinc (77,78).

5.2 Preparation of the U.H.V. System for an Evaporation Run

Before each evaporation run, the vacuum chamber was thoroughly cleaned of all zinc deposits resulting from the previous experiment.

The geometry of the vacuum chamber insured that only those parts between the sample and the glass viewport were affected, viz. the cleavage tool, the crystal holder, the chamber walls and the viewport.

A dilute HCℓ solution was used to clean these parts. As HCℓ is strongly adsorbed on stainless steel surfaces (see Section 6.1), this was followed by thoroughly rinsing with warm water. The vacuum chamber was finally washed with acetone and dried in a stream of warm air.

The sample, having previously been degreased in acetone, was mounted in the crystal holder. To prevent the introduction of unnecessary contamination from moist hands, nylon gloves were worn whilst performing all operations inside the vacuum chamber, i.e. when mounting the crystal or assembling the electron gun. The system was finally closed by replacing the glass viewing port.

After the cryogenic pumps had reduced the pressure to approx. 3×10^{-3} torr., the "Fiberfrax" bakeout oven was placed over the vacuum chamber. A one-hour bakeout, conducted at 150°C whilst pumping only with the sorption pumps, removed a major portion of the water vapor which remained adsorbed on the chamber walls following the cleaning procedures. Without a preliminary bake-out the extra flux of gas desorbing from the walls during pump-down made it extremely difficult to start the ion pump, which has a low pumping speed at high pressures. After the system had been allowed to cool for thirty minutes, the U.H.V. valve to the sorption pumps was closed, and the ion pump started without difficulty.

In a typical pump-down cycle, the pressure would fall to $\sim 10^{-8}$ torr. overnight and the bakeout oven was again switched on. The oven temperature was gradually raised to 250°C, the heating rate being manually controlled in order to maintain the pressure in the vacuum system in the range 10^{-6} to 10^{-5} torr. When the pressure had fallen below 10^{-6} torr. at 250°C, the ion pump was baked-out to 200°C, while pumping, using a suitable heating mantle.

If it is desired to maintain very low pressures in a vacuum system while high temperature current filaments are operative, such filaments must be run during bakeout at currents which effectively outgas the filament, yet sublime negligible material. Accordingly, the titanium sublimation pump filament was held at 25 amps. throughout the bakeout and the electron gun filament held at 12 amps. during the last hour of the bakeout. The current through the gun-filament was increased to 16 amps. during the final 10 minutes -- a procedure which was found necessary if outgassing from the gun, during use, was to remain negligible.

The bakeout, which normally lasted about 8 hours, was complete when the pressure, with all filaments operating, had fallen to 1×10^{-6} torr. The system was allowed to cool down overnight and next morning, if the unit was free of leaks, the pressure, as determined from the ion pump current, had fallen to $<< 10^{-9}$ torr. The bakeout ovens and mantles were then removed.

The ion gauge could then be reconnected, switched on and outgassed by electron bombardment of the grid and collector. The length of this operation depended on the vacuum, but the ion gauge reading normally approached a steady state within fifteen minutes. On completion of the

---

* Glas-Col Apparatus Company, Serial No. 441554

ion gauge bakeout, the titanium sublimation pump was switched on for two minutes in order to further reduce the partial pressures of getterable gases which may have desorbed whilst outgassing the ion gauge.

Outgassing the sample was extremely important, as it had a critical effect on the pressure which could be maintained during the evaporation run. The temperature calibration experiments had shown that when the electron gun filament current, I_F, was 15.5 amps. (giving an emission current of ∿1 mA) and the gun-to-sample potential difference, V_F, was 1.1 kV, the sample temperature rose to 390°C in 3 1/2 minutes and could be held at this level if the gun was operated at a current, I_F, of 13.8 amps. and potential, V_F, of 1.2 kV. In light of these facts, the sample and gun were outgassed by bombarding the sample for 2 1/2 minutes with I_F = 16 amps and V_F = 1.1 kV and then holding I_F = 16.0 amps and V_F = 1.2 kV for a further 2 1/2 minutes. Because it was observed that the outgassing characteristics were affected very little by repeated operations of the above procedure, it was only carried out once before each evaporation run.

After completion of the various outgassing procedures, the system was normally left for twenty-four hours to pump-down to its ultimate base pressure, which was in the range 1 to 5 x 10^{-10} torr.

5.3 Evaporation in Vacuum

Before cleaving the crystal, the titanium sublimation pump was switched on for two minutes, in order to reduce the partial pressures of oxygen and other active gases. Then, with a background pressure of $\sim 5 \times 10^{-10}$ torr, cleavage parallel to the (0001) crystal plane of zinc was effected. If successful, the electron gun filament current and voltage were switched on and, as discussed previously, were held at 15.5 amps. and 1.1 kV respectively for 3 1/2 minutes. At the end of this period, with the surface temperature approximately 390°C, evaporation was confirmed by the visible condensation of zinc vapor on the viewing port. The power input to the gun was then held at 13.75 amps. and 1.2 kV for the duration ($\sim$ 3 minutes) of the evaporation run. Throughout the experiment, the pressure as measured by both the ion gauge and the ion pump calibration, was recorded. The pressure during the "heating-up" period was 1 to 2 x 10^{-7} torr. but quickly fell to 4 to 6 x 10^{-8} torr. when the filament current (or more realistically, the emission current) was reduced. After the power was completely switched off, the pressure fell within a few minutes to the low 10^{-9} torr. range.

During many experiments, the mass spectrum of the residual gases was monitored on the oscilloscope at each stage of the procedure, thus giving a detailed knowledge of the "vacuum" environment.

It might seem reasonable to have operated the sublimation pump during the evaporation run. However, because of its relatively low pumping speed, it has a negligible effect on the background pressure.

On the completion of an evaporation run, the ion gauge and ion pump were switched off and the vacuum system brought to atmospheric pressure by introducing normal "cylinder"-grade nitrogen via the needle values N_1 and N_2 in the gas-leak system and the U.H.V. valve "V". The viewing port flange was opened and the sample carefully removed.

5.4 Evaporation at High Oxygen Partial Pressures

For those experiments which involved the introduction of oxygen to the evaporation chamber during the evaporation run, the following modifications to the experimental technique were required.

The procedures described in Section 5.3 were repeated but, instead of switching off the electron gun after 6 minutes, "ultra-pure" (99.95%) oxygen* was introduced to the system via the variable leak valve. The conductance of the valve was set so as to give approximately the desired oxygen partial pressure in the system.

During the experiment the total pressure was read on the ion gauge. This value was corrected to obtain the oxygen partial pressure, as follows:

(i) of the total pressure, the percentage which was due to oxygen (> 90 per cent) was determined using the mass-spectrometer in the oscilloscope mode.

(ii) the ion gauge reading was adjusted by a factor which is a measure of the gauge sensitivity for oxygen. This factor, as supplied by the manufacturer, is 1.1.

Controlling the partial pressure of oxygen via the total pressure in this manner, permits the use of the mass analyser during the experiment to obtain the maximum possible information concerning the residual gas spectrum. However, it should be stated that this method is only satisfactory when the background pressure is both reasonably constant and relatively small, i.e. less than 10% of the total pressure.

---

* Matheson of Canada Limited

After the oxygen was admitted to the system, the sample was held at 390°C for another three minutes. Then the electron gun was switched off and the sample allowed to cool down in the oxygen environment, the variable leak valve being closed normally after a further period of six minutes. The surface temperature at this time was less than 130°C and further evaporation would have been negligible.

The ion pump continued to pump throughout the evaporation runs. At the end of an experiment, the vacuum system was brought to atmospheric pressure and the samples removed in the manner described previously for vacuum evaporated crystals.

5.5 Optical Microscopy

A Zeiss two-beam interference microscope which could be operated with either white light or green thallium light, was used to study the surface morphologies of the evaporated samples. In its operation, the primary beam is split along two paths -- one to the sample and the other to an optically flat silvered surface. The reflected beams are combined and when viewed through a suitable eyepiece, give a regular interference pattern. If the specimen was perfectly flat, an appropriate adjustment of the instrument would produce an image of equally spaced, sharp interference finges. Sufficiently large deviations from flatness would produce fringe shifts, corresponding to the increased path length. When green light was employed, the depth interval corresponding to a shift of one fringe spacing was 0.27 μm. Under optimum conditions, a vertical sensitivity of 300Å can be realized. This limitation is a result of the simple "sine-wave" nature of fringes, which makes more accurate measurement of fringe spacings impossible, unless special photographic imaging techniques are used. The interference microscope also permits visual examinations with magnifications up to 480x. By employing a beam interupting device it is possible to obtain both interference micrographs and normal optical micrographs of the same area.

A 35 mm. camera was attached to the microscope for photographic recording. Calibration of the photographic magnification was performed by taking micrographs of a standard stage micrometer containing 200 lines spaced 0.01 mm.

Except for evaporation into a relatively high partial pressure of oxygen, the evaporation features were sharply faceted. Therefore, the interference microscope could not be used in its normal mode of operation viz., to give "contour maps" of elevations or depressions which had developed on the surface. However, the microscope did prove useful in the following applications.

5.5.1 General Survey of Evaporation Morphology

After its removal from the vacuum system, the evaporated sample could be quickly examined under the microscope. A general picture of the surface topography could be ascertained and a decision made on the structures which might be investigated further by electron microscopy.

5.5.2 Indirect Measurement of Evaporation Pit Depths

An indirect method was devised by which the interference microscope could be employed to measure pit depths. This method is illustrated in Fig. 11 where CC' is the optically flat reference surface, SS' the surface of the sample and the dashed lines FF' represent the sample positions which give destructive interference when SS' and CC' are parallel. If, however, the sample is tilted through a small angle, θ, with respect to CC' (Fig. 11(a)), interference fringes are produced where the dashed lines intersect SS'. This is illustrated in Fig. 11(b) which is a projection of the corresponding lines of intersection on a surface parallel to CC'. The fringe system in Fig. 11(b) is the interference pattern which is actually observed in the microscope.

When the microscope is operated with the white light source, a narrow interference band containing only a few fringes, each having a different colour, is produced. If the instrument is adjusted so that one of these fringes can be observed at the pit-bottom the same fringe should also be observable on the surface at A. It follows, that the number of fringes contained in the distance AE times $\lambda/2$ is equal to BE. BE is related to the pit depth BD by BD = BE cos θ. As θ was normally $\leq 0.5°$ during this operational mode, cos θ can be taken as unity. It is evident that the instrument must be operated with the green light source if the fringes along AE are to be observable. Consequently, to measure pit depths, the white light source was employed to locate the point A and then the green light source was used to determine the number of fringe spacings, N. Once the pit depth (= N x 0.27 μm) was known, it was possible to calculate two other important properties of the pit.

(i) ledge height: when a pit face was composed of low index terraces separated by macroscopic ledges, the mean ledge height is given by the ratio, pit depth/number of ledges on the pit face. This technique was very difficult for deep and/or steep-sided pits and was best suited to pits composed of twenty or less ledges. Otherwise, counting the ledges was tedious and inaccurate.

(ii) pit slope: from a photograph, it was possible to obtain the pit radius, providing the photographic magnification is known. The pit slope can then be computed as pit-depth/pit-radius.

5.5.2 Evaporation Pit Density

Whilst operating the interference microscope at its lowest magnifying power, a direct optical micrograph was taken of a general surface area. The number of pits in this area could be used to estimate the number of pits per cm^2. By repeating this procedure for other regions on the surface, an average value of the pit density could be obtained.

5.6 Scanning Electron Microscopy

When used to study ledge structure in etch pits, the optical microscope has two major shortcomings, viz. limitation of the linear magnification and of the depth of focus. In many cases, these problems have been solved by using replica electron microscopy. In the present work, this method was not found to be applicable because,

(i) of the difficulty in replicating sharp corners and edges satisfactorily,

(ii) of the difficulty in separating a replica from zinc surfaces without destroying the fine structure in the replica. Various methods were tried but none gave complete satisfaction.

(iii) replication would destroy the surface for meaningful subsequent examination.

These problems were obviated by the use of a Cambridge Stereoscan scanning electron microscope (S.E.M.) which allowed direct observation of the evaporated zinc surface, without further preparation. The depth of focus is 300 times that of an optical microscope.

In the operation of the S.E.M., a fine beam of high energy electrons is scanned across the specimen surface in a rectangular raster, synchronized with the spot of a cathode-ray tube (CRT). The secondary electrons resulting from the interaction of the beam with the specimen modulate the CRT brightness, and therefore a picture of the specimen is built up on the CRT face. Since the secondary-electron yield depends on the angle between the specimen surface and the electron beam, the picture obtained represents the surface topography.

The stereoscan employed primary electrons with energies in the range 20-30 KeV. The magnification was variable between 20 and 100,000, although focusing was extremely difficult at higher magnifications due to the level of the electronic background noise. The spot size ($\sim$ 100Å diameter) and the scatter of secondary electrons limited the resolution to approximately 200Å. To achieve better contrast, the sample could be tilted towards the collector at angles, β, to a maximum of 45° from the horizontal.

In the present study, interesting surface features which had been observed initially by optical microscopy were studied in greater detail in the S.E.M. at various magnifications. The resolution of fine structure on macroscopic ledges offered a ten-fold improvement over optical methods.

5.7 Chemical Etching Techniques

An examination of the etching behavior of several chemical solutions on zinc surfaces has been conducted by Rosenbaum and Saffren (79). They systematically examined the halogens chlorine, bromine and iodine in different organic solvents. Several solutions were obtained which produced etch pits related to line imperfections, possibly dislocations, emerging on the (0001) surfaces of high purity zinc crystals. One of these solutions, 1 Mol. HCℓ in ethanol, was employed in this study to obtain information, complementary to that given by the evaporation results, regarding the nature of possible defects which intersect (0001) zinc cleavage surfaces.

Fresh (0001) surfaces for etching were produced by cleaving a thin section from a large zinc single crystal. Before cleavage, the crystals were cooled to 77°K in a liquid nitrogen dewar. They were then removed from the dewar, placed on a clean table and cleaved by a sharp tap with a hammer on a knife-edge cleaving instrument which was held against the rod and parallel to the basal plane of the crystal.

Immediately after cleaving, the samples were placed in ethanol and warmed to room temperature, thus preventing excessive condensation of water vapor on the freshly cleaved surface. After rinsing in anhydrous di-ethyl ether, the samples were dried in a flow of warm air.

The samples were etched in freshly prepared solutions contained in 250 ml. beakers. Following the etching, the samples were washed in absolute alcohol for 20 secs. and in anhydrous di-ethyl ether for 15 secs. After drying, the etched surfaces were examined with the Zeiss interference microscope.

On several occasions, the unevaporated matching vacuum cleavage surfaces were chemically etched. After removal from the vacuum system, the crystals were etched in a similar manner to that described above for air-cleaved surfaces.

CHAPTER 6

EXPERIMENTAL RESULTS

6.1 Residual Gas Analysis

Residual gas partial pressures under various experimental conditions are listed in Tables 2-7. In each case, the total pressure measured by the ion gauge, is given at the bottom of the table.

In column two, effective partial pressures corresponding to the ion currents which were observed for the mass/charge ratios shown in column one, are tabulated. Cracking patterns* of common molecules in the G.A.4 residual gas analyser source were used to assign probable ions (column three) to the mass numbers. Based on this interpretation of the mass spectrum, possible parent molecules were evolved for each ion and these are listed in column four. Finally, in column five, partial pressures of the residual gases are tabulated opposite the appropriate mass number. When computing the residual gas partial pressures from the related ion current measurements, the following rules were adopted:

(a) the currents corresponding to singly and doubly ionized molecules were assumed to be additive, i.e. each ion represents a single un-ionized gas molecule;

(b) the ion currents at mass numbers 12,13,14,15 and 16 were added to give the partial pressure of CH_4. This assumes that the ions

---

* supplied by Vacuum Electronics Corporation

C^+, CH^+, CH_2^+ and CH_3^+, each represent a methane molecule via dissociation reactions of the type

$$CH_4 \rightarrow CH_3^+ + H^+$$

The ion currents at these mass numbers result not only from the dissociation of CH_4 but also from the dissociation of higher hydrocarbons. Consequently, the procedure outlined above would give an incorrect value for the partial pressure of CH_4. However, since these partial pressures were negligible, their contributions to the mass peaks were assumed to be small and, therefore, the procedure used is a good approximation. Similar rules were followed when calculating the partial pressures of $HC\ell$ and H_2O.

The dissociation of CH_4, H_2O and $HC\ell$ into their constituent ions contributes to the magnitude of the H_2^+ peak. Therefore, allowance for this fact has been made when calculating the H_2 partial pressure from the ion current at mass number 2.

It is generally found that, in an otherwise clean vacuum system, the residual atmosphere consists mainly of hydrogen, water vapor and carbon monoxide. The hydrogen is believed to diffuse from the vacuum chamber walls and the water vapor originates to some extent from the gas atmosphere which filled the system before pumping, but mostly from water which adsorbs on the vacuum components when they are exposed to the atmosphere or subject to cleaning procedures.

In order to account for the relatively high carbon monoxide partial pressures, the following chemical reaction has been proposed (80)

$$C + H_2O \rightarrow CO + H_2$$

where carbon which is present in all stainless steel parts, reacts with adsorbed water vapor. This reaction also provides a secondary source of hydrogen.

In the presence of hot tungsten filaments, e.g. in an ion gauge, the partial pressure of carbon monoxide is observed to increase relative to that of water vapor. Consequently, Blears (81) has suggested that the above reaction also takes place at hot filaments, carbon either being an impurity in the tungsten or arising from adsorbed hydrocarbons.

Its extent and relative importance as a source of carbon monoxide depends on the number and the temperature of the filaments and the partial pressure of water vapor in the system.

These assumptions are very useful in interpreting the residual gas analyses listed in the above tables. For example, in an unbaked system (Table 2), whilst the partial pressures of water vapor and hydrogen were large, that of carbon monoxide was also appreciable as a result of the conversion of water vapor into carbon monoxide and hydrogen as discussed above. A high temperature bakeout drives most of the water vapor from the walls and because much of the remainder reacts with carbon at the ion gauge filament, the partial pressure of carbon monoxide was always found to be much larger than that of water vapor in the ultra-high-vacuum region (Table 3). It is interesting to note that when the sublimation pump was operating in ultra-high-vacuum, the carbon monoxide and hydrogen partial pressures were significantly reduced but the water vapor component was little affected.

The large carbon dioxide partial pressures in Tables 2-5 probably occurred as a result of the secondary reaction

$$C + 2H_2O \rightarrow CO_2 + 2H_2$$

the reactants having the same sources as those in the primary reaction.

Acetone, which was used during the cleaning procedures to "degrease" the vacuum components, usually dissociated on hot filaments. The mass spectrometric results show that methane was the major dissociation product. Its cracking pattern produced minor peaks corresponding to C^+, CH^+, CH_2^+ and CH_3^+ ions. The methane cracking pattern, when it existed, was taken as evidence that the signal at mass number 16 was due to methane and not atomic oxygen.

The use of a dilute hydrochloric acid solution to remove zinc deposits from the vacuum chamber walls almost certainly caused the high partial pressures of $HC\ell$, particularly in the ultra-high vacuum region. $HC\ell$ is known to be adsorbed strongly on metal surfaces and as a result it is difficult to remove, even by a high temperature bakeout.

The residual gas analysis recorded in Table 3 is representative of the background atmosphere during cleavage of the zinc single crystals. Observation of the instantaneous mass spectrum on the oscilloscope screen revealed that the cleavage event was accompanied by a sharp rise in the ion current at mass number 28. The evolved gas was rapidly pumped away and the pressure in the system decreased to its original value within several seconds after cleavage. The gas was probably nitrogen which had dissolved in the crystal during growth. Only a small concentration would be required to produce an observable pressure rise in such a high vacuum.

During electron bombardment of the sample, the main gas which evolved appears to have been water vapor. However, the mass spectrometric results (Table 4) indicate that the water vapor was quickly converted into carbon monoxide, carbon dioxide and hydrogen, presumably by reacting with carbon at the electron gun filament and at the stainless steel filament shield which became quite hot when the gun was operated close to full power. Proof of this assumption was forthcoming when it was observed that, after the filament current was reduced on attaining a sample temperature of 390°C, the water vapor partial pressure increased at the expense of the partial pressures of the aforementioned species (Table 5) and continued to do so until the electron gun acquired a new equilibrium temperature.

At 1600°C (the temperature of the tungsten filaments), the probability of the reaction

$$C + H_2O \rightarrow CO + H_2$$

is significantly greater than the probability of the reaction (68)

$$C + 2H_2O \rightarrow CO_2 + 2H_2$$

Therefore in Tables 2 and 3 the partial pressures of CO are much larger than those of CO_2. As has been mentioned previously, these reactions are also thought to take place at the electron gun shield which, during operation, had a temperature of about 600°C (red heat). At this temperature the difference in the reaction rates is not as pronounced as at 1600°C (68). Consequently, the partial pressures of CO_2 were observed to increase relative to those of CO (Tables 4 and 5) during an evaporation run.

Whilst heating the sample, a fairly constant pressure (∿ 1 x 10^{-7} torr) was maintained. As the sample temperature approached 300°C, a sharp rise in pressure, lasting approximately 30 secs. was observed. The mass spectrum, as displayed on the oscilloscope, showed a concurrent rise in the H_2^+, Ne^+ and CO^+ peaks indicative perhaps of water vapor and other adsorbed gases desorbing from the zinc surface. They could have been adsorbed with a surface coverage of approximately one monolayer during the initial stages of the heating cycle.

In all of the above tables, a relatively high ion current was detected at mass number 20. As the only species which should produce a significant current at this value is neon, it is thought that, although possible sources of neon were few, the slow pumping speed of sputter-ion pumps for neon caused an observable partial pressure of neon in the vacuum chamber. In the presence of an air leak, a peak at mass number 20 was prominent. When the leak was closed, the signal only disappeared after an extended period of time which would indicate that Ne^+ ions were most likely responsible for the peak at mass number 20.

During evaporation in an oxygen environment the dominant peak in the mass spectrum naturally corresponded to the presence of O_2^+ ions (Table 6). Other minor peaks were observed for CO^+, O_2^{++}, and H_2O^+ ions. In this case, the formation of carbon monoxide could also proceed via the reaction

$$2C + O_2 \rightarrow 2CO$$

thus providing an additional source. Carbon monoxide and water vapor were, of course, present as part of the background atmosphere.

Several evaporation runs were carried out in the presence of a carbon dioxide leak. The mass spectrum (Table 7) showed that, besides a major signal at carbon dioxide, dissociation of the molecule at hot filaments produced substantial partial pressures of carbon monoxide, atomic oxygen and carbon. As normal grade carbon dioxide was used, neon was probably present as an impurity in the gas.

Finally in this section it should be stated that, during evaporation, zinc atoms were not detected by the mass spectrometer when used in the oscilloscope operational mode. This is not surprising as at such low pressures, zinc atoms should travel to the chamber walls where they condense without being scattered by the residual gases. Therefore, very few zinc atoms would reach the mass-spectrometer, the ion gun of which was not in line-of-sight of the sample.

6.2 Topography of (0001) Zinc Cleavage Surfaces

It was not possible to produce a cleavage surface completely free of optically observable structure. Cleavage steps, similar to those shown in Figure 12(a) were the most commonly observed departures from a flat surface. Figure 12(b), an interference micrograph of the same region, shows that the step heights are about 600Å. These "river-like" step patterns are typical of freshly cleaved surfaces (82). $(10\bar{1}2)$ mechanical twins, emergent along $<11\bar{2}0>$ directions in the cleavage surface, were also frequently observed. A pair of twins is shown in Figure 12(c). It can be seen that, as the interference fringes are displaced in opposite directions at each twin, the surfaces of the two twinned regions must be of opposite slope.

6.3 Evaporation in Vacuum

6.3.1 General Surface Observations

Evaporation of (0001) zinc cleavage surfaces under the experimental conditions described in Section 5.3, resulted in the development of new surface structures distributed non-uniformly over the surface. The major evaporation features were point-bottomed pits which had an average surface density $\sim 4 \times 10^4$ cm^{-2} (Table 8). In Figure 13, which is an optical micrograph of a thermally evaporated surface, it can be observed that the pits had the hexagonal symmetry of the zinc lattice. They had depths $\sim$ 2.5μm and their faces made angles of about 3° with the basal plane. A small fraction ($\sim$ 10%) of the pits were larger than the majority, with depths $\sim$ 5μm. They can be picked out easily in Figure 13.

The disappearance of all small cleavage steps indicated that, in addition to enhanced evaporation at local centres, there was also considerable general evaporation of the surface.

6.3.2 Ledge Structure on Pit Faces

By employing the scanning electron microscope, the pit faces were observed to consist of (0001) terraces separated by macroscopic ledges. The ledge heights were determined to be about 1400Å. Figure 14 shows ledge structure typical of a thermovacuum pit, the ledge spacings being about 2μm

The ledges were observed to be parallel to the intersection of

$(10\bar{1}2)$ mechanical twins, with the basal plane as shown in Fig. 36. Therefore, the ledges were in $<11\bar{2}0>$ directions, which are the close-packed directions. It is readily seen in Fig. 14 that there is very little observable structure along the macroledges. This point is further illustrated in Fig. 15 which is a high magnification (12,000x) scanning electron micrograph of the ledge structure in a flat-bottomed pit. It also shows that the (0001) facets are flat, within the resolution of the instrument.

6.4 Evaporation in Oxygen

6.4.1 Effect of Oxygen on Ledge Structure

A summary is given in Table 8 of the main observations on (0001) zinc cleavage surfaces which had been evaporated in oxygen with partial pressures in the range 10^{-7} to 10^{-6} torr.

When the partial pressure of oxygen was 1.5×10^{-7} torr, surface pitting was again observed, as shown in Fig. 16(a). As had been observed on vacuum evaporated surfaces, a small fraction ($\sim$ 10%) of the pits are larger and deeper than the majority. However, on closer examination of the surface, two distinct differences were observed between the ledge structure on surfaces which had been evaporated in oxygen and that on surfaces which had been evaporated in vacuum. Firstly, the ledge heights had decreased to about 800Å and secondly a distinct roughening of the ledges had occurred. The latter effect was characterised by the formation of macrokinks*. This is illustrated in Fig. 16(b), which is

---

* A macrokink is defined here as a lateral displacement of the surface ledge by a distance many times greater than the fundamental lattice spacing.

a scanning electron micrograph of the ledge structure in one of the pits shown in Fig. 16 (a).

When the partial pressure of oxygen was increased to 4.5 x 10^{-7} torr, an apparent rounding of the thermal pits was observed. This is shown in Fig. 17(a). However, on examination of the ledge structure with the scanning electron microscope, it was observed that the macroscopic rounding was due to a "pile-up" of macrokinks at the intersection of $<11\bar{2}0>$ ledges, as shown in Fig. 17(b). The geometry of this "pile-up" is better illustrated in Fig. 18 which is an electron micrograph of a flat-bottomed pit on this surface. It can be observed that at macrokinks, the ledges are displaced in other $<11\bar{2}0>$ directions.

It is noteworthy that the degree of "rounding" increases with distance from the pit centre. In Fig. 19 it is shown that, at the pit bottom, single macrokinks are the most common structural features on otherwise straight ledges. However, it is possible to observe the commencement of kink "pile-up" within a few steps of the centre.

Raising the partial pressure of oxygen to 6.5 x 10^{-7} torr resulted in a further increase in pit rounding, as shown in Fig. 20(a) which is a low magnification scanning electron micrograph of typical pits on this surface. Fig. 20(b), which is a micrograph of pit A in Fig. 20(a) at a higher magnification, once again shows that the pile-up of kinks at pit corners increases with distance from the pit centre. Furthermore, on a given pit face, it is possible to mark the boundary between $<11\bar{2}0>$ ledges and the rounded corners by approximately straight lines, xx' and yy', as shown in Fig. 20(b). This observation holds for all pits in which a "pile-up" of macrokinks occurred at the intersection of adjacent faces.

In Fig. 20(c), it is shown that, although the ledge structure within the pit was extremely rough, crystallgraphic contraints on the ledges remain operative. It is also observable that small "peninsulas" have developed along the ledges.

When the oxygen partial pressure was increased to 8 x 10^{-7} torr, approximately round pits developed during evaporation. This is illustrated in Fig. 21(a) which is an interference micrograph of a typical region on the surface. It also shows that the pit-bottoms were quite shallow, if not flat. In Fig. 21(b), the variation in fringe spacing indicates that the pit slope decreases with increasing distance from the centre.

A scanning electron microscopic examination of this surface revealed that, although crystallographic features were absent (Fig. 21(c)), a mottled ledge structure was observable on the pit faces. An example is shown in Fig. 21(d).

Evaporation in an oxygen partial pressure of 1.1 x 10^{-6} torr, produced a very rough surface morphology. This may be deduced from the very irregular interference fringes shown in Fig. 22(a). Fig. 22(b) is a scanning electron micrograph of an extremely rough pit on this surface, whilst Fig. 22(c) shows a pit of a smoother profile. An ordered ledge structure was either absent or was beyond the resolution of the instrument. When compared to the smooth basal terraces (for example, in Fig. 14(b)), at lower oxygen partial pressures, the surface shown in Figures 22(b) and 22(c) is quite rough. When studied under the scanning electron microscope, the small irregular features shown in Fig. 22(a) were found to be hillocks. An example is shown in Fig. 22(d).

In the absence of a sharp ledge structure on the pit faces, "point" bottomed pits were difficult to observe with the scanning electron microscope. This is illustrated in Fig. 23. For this reason, the micrographs which are employed in the preceding figures show only flat-bottomed pits .

6.4.2 Additional Effects of Oxygen

(a) The introduction of oxygen at an earlier stage, for example as the sample temperature reached 390°C, produced effects similar to those described in the previous section. However, the size of the pits was somewhat reduced.

(b) As the oxygen partial pressure was increased, the fraction of pits which had flat-bottoms also increased. Whereas, five per cent of the pits which had developed during vacuum evaporation were flat bottomed, Fig. 24 shows that after evaporation in an oxygen partial pressure of 6.5×10^{-7} torr, as many as twenty per cent of the pits were flat-bottomed.

(c) At low partial pressures of oxygen, the pit edges were extremely sharp. This is clearly shown in Fig. 16(a). As the partial pressure was increased, the edges became quite rounded and extended, with a shallow lip, much farther into the basal surface. This point is illustrated in Fig. 25 which is an optical micrograph of evaporation pits when the oxygen partial pressure was 4.5×10^{-7} torr.

6.5 Evaporation of Pre-cleaved Samples

Several evaporation runs were performed on zinc (0001) surfaces which had been prepared by cleavage in air, as described in section 5.7. The evaporation features which were observed on these surfaces are also summarized in Table 8.

The general surface was quite rough relative to evaporated vacuum cleavage surfaces. Unevaporated islands, similar to that shown in Fig. 26 were frequently observed on these surfaces. The interference micrograph in Fig. 27(a) shows several pits, typical of those which developed on pre-cleaved samples. The ledge structure within the pits was quite irregular, as is shown in Fig. 27(b).

When precleaved samples were evaporated at lower temperatures ($\leq$ 300°C), general evaporation of the surface did not occur. Rather evaporation only occurred at local centres, such as cleavage steps.

6.6 Effect of Sample Purity

All evaporation runs which have been described in the previous sections, were performed with samples grown from zinc with a stated 99.999% purity. In order to investigate the effect of sample purity on the evaporation features, a number of runs were carried out with crystals of different bulk purity. A summary of the observations is given in Table 9.

Employing the method described in section 5.1, an orientated single crystal was grown from a 99.9999% zinc rod, using a 99.999% zinc seed. To ensure the highest possible purity of the final specimen, this crystal was then used to seed the growth of several high purity crystals.

Evaporation of vacuum cleavage surfaces, prepared from these crystals, resulted in the development of shallow (depth $\sim$2μm), faceted pits, examples of which are shown in Fig. 28. The ledges [illegible] had heights of about 2000Å and very few macrokinks along their lengths.

The density of pits was ∿ 8×10^4 cm^{-2}, which is similar to those on other samples, but the density of deep pits (< 5% of the total) was smaller than on less-pure samples. This is illustrated in Fig. 29.

Several evaporation runs involved samples whose bulk purity was significantly lower than the others. During evaporation, the vacuum cleavage surface of zinc single crystals, grown from raw material with a stated 99.99% purity, developed a low density of deep (depth 3-5 μm) thermal pits. About fifty per cent of the pits were flat-bottomed. The ledge structure inside the pits was very irregular and reminiscent of that observed on samples which had been evaporated in an oxygen environment. This is shown Fig. 30, where the pile-up of macrokinks at pit corners is again observable.

In an attempt to obtain a sample of very low purity, a crystal was grown from 99.99% zinc rods but with little effort made during the growth process to prevent the introduction of further impurities into the crystal. The evaporated cleavage surface was covered with round thermovacuum pits, similar to those shown in Fig. 31(a). The pit density was ∿ 10^4 cm^{-2}. The "ledge structure" in a typical pit is shown in Fig. 31(b). It is seen to be similar to that observed in 99.999% zinc crystals which had been evaporated in oxygen partial pressures of approximately 1×10^{-6} torr. Due to the presence of many small hillocks, the general surface was very rough, as is shown in Fig. 32.

A semi-quantitative spectrographic analysis of both high purity and low purity samples revealed the presence of the same impurities as are listed in Table 1 for 99.999% zinc samples. However, this method of analysis proved insensitive to changes in sample purity and therefore, it was considered unreliable as a quantitative measure of the impurity concentrations. Consequently, these quantities have been omitted from Table 1. It should also be pointed out that the above method of analysis would not have detected several important impurities which may have been present in the samples. Of these, the most important is oxygen.

6.7 Miscellaneous Evaporation Features

6.7.1 Polycrystalline Samples

In Section 5.1, it was described how a small groove was machined into each sample to facilitate cleavage. As a result, a region of the crystal adjacent to the groove was certainly plastically deformed. During outgassing of the sample prior to an evaporation run, recrystallization in the damaged region produced a shallow polycrystalline surface layer. This could increase the difficulty of cleavage, which was therefore accompanied by further deformation of the sample.

After the evaporation run, it was observed that the outer regions of the cleavage surface were invariably of non-basal orientation. Further recrystallization and subsequent grain growth had produced new crystal orientations. The degree to which the surface was covered with grains of non-basal orientation was observed to increase as the cleavage difficulty increased.

The large grain size indicated that the amount of deformation during cleavage was only a few per cent, because under these conditions, very few nuclei for recrystallization are produced and these are able to grow into grains of large size. This factor has often been used to produce large alloy crystals by the "strain-anneal" technique(83).

This phenomenon made a very important contribution to the present study, since it allowed the observation of evaporation features on "clean" non-basal surfaces.

All non-basal orientations were observed to develop (0001) facets during evaporation. An example is shown in Fig. 33. The macroledges which separated the (0001) facets were always in a $<11\bar{2}0>$ direction or combinations of $<11\bar{2}0>$ directions. Hexagonal pits were frequently observed on orientations, vicinal to the basal plane. This is illustrated in Fig. 34(a). (The mean pit density was about 4×10^3 cm^{-2}.) The relatively straight ledges on the general surface suggest that the surface orientation was of the type $(1\ 0\ \bar{1}\ \ell)$. The scanning electron micrograph in Fig. 34(b) shows the detailed ledge structure in the immediate vicinity of a typical pit on this surface.

6.7.2 Observation of Nucleation Centers

The scanning electron microscope allowed the observation of small steep-sided "holes" at the bottoms of all point-bottomed thermal pits. An example is shown in Fig. 35(a). They are probably associated with active ledge sources in each pit. Their absence in all flat-bottomed pits further substantiates this conclusion. A distinct difference was observed between the "holes" in shallow pits and those described above for deep pits. As can be seen in Fig. 35(b), the pit bottom has a much more gradual slope in these pits.

6.7.3 Evaporation Structures at Mechanical Twins

Some interesting evaporation features developed at deformation twins emerging on zinc (0001) surfaces. Fig. 36(a) shows the intersection of a pair of parallel $(10\bar{1}2)$ twins with a single $(10\bar{1}2)$ twin. A high density of relatively shallow etch pits were often observed at the lower edge of a twin. This is illustrated in Fig. 36(b).

A complicated ledge structure developed on each twin during thermal evaporation. Fig. 37(a) which is a scanning electron micrograph of two adjacent, thermally etched twins, shows that the ledges were parallel to $\langle 11\bar{2}0 \rangle$ directions. Fig. 37(b) shows these ledges at a higher magnification.

6.7.4 Thermal Pit Formation at Sub-grain Boundaries

In chemical etching studies, there are many examples of etch pit formation along sub-grain boundaries (84). On evaporated zinc (0001) surfaces, pit arrays, indicative of sub-grain boundaries were often observed. An example is shown in Fig. 38. Thermal pitting along more complex misorientation boundaries was also observed. This is shown in Fig. 39, which depicts three sub-grain boundaries meeting along a nodal line.

6.7.5 Thermal Pits Along Glide Bands

On several occasions, pits lying along nearly straight lines were observed. This is illustrated in Fig. 40. By a chemical etching technique, the pits were shown to lie along $(10\bar{1}0)$ directions. Groups of pits lying along different $\langle 10\bar{1}0 \rangle$ directions are shown in the above micrograph. It will be shown later that these pits represent screw dislocations in the $\{11\bar{2}2\}$ $\langle \bar{1}\bar{1}23 \rangle$ slip system.

6.7.6 Thermal Pits Along Cleavage Steps

If, due to certain experimental problems, e.g. malfunction of the electron gun, the time needed to heat the sample to the evaporation temperature was increased and the surface temperature was lower than that normally employed, evaporation occurred only at isolated centres, which, as is shown in Fig. 41, were mainly situated along cleavage steps. These pits were often observed to become flat-bottomed after prolonged evaporation.

For the sample shown in the above micrograph, the "heating period" was eight minutes. The surface temperature was unknown.

Extremely deep, multi-centred pits, similar to that shown in Fig. 42, frequently developed on these surfaces. They had depths of about 50 μm and their faces made angles of up to 30° with the basal surface, in contrast to the shallow pits which normally developed.

6.7.7. Pit Asymmetry

Many pits, particularly the deeper ones, were asymmetric along $<11\bar{2}0>$ directions. A typical example is shown in Fig. 43. This asymmetry can also be seen in Fig. 17(a), i.e. on a sample which was evaporated in a relatively high partial pressure of oxygen.

Symmetrical pits are probably formed at defects which intersect the surface normally whilst asymmetrical pits occur at defects which lie in planes inclined to the surface. The direction of asymmetry corresponds to the direction of inclination of the defect plane with the surface and the amount of asymmetry depends on the depth of the pit and the angle of inclination. Examination of a number of pits, revealed that the angle of inclination was about 30° and was approximately constant for all asymmetric pits. This angle and the direction of asymmetry would suggest defects lying in $(10\bar{1}3)$ planes which make angles of 32.15° with the basal surface.

However, this result may be fortuitous because evaporation kinetics may exaggerate the asymmetry produced by a defect on a less-shallow plane.

6.7.8 Evaporation in Carbon Dioxide Environments

As carbon dioxide was the major oxidative background species during the oxygen-leak experiments, several evaporation runs were performed with a carbon dioxide leak. Similar changes in the ledge morphology to those reported for oxygen, were observed at comparable partial pressures. However, as was reported in Table 7, dissociation of carbon dioxide at hot filaments produced relatively large partial pressures of oxygen (O^+) and carbon, both of which would affect the ledge morphology if adsorbed on the surface. This makes an understanding of the observations difficult, although it must be concluded that carbon dioxide adsorption played a role in the development of evaporation morphology.

6.8 Chemical Etching Results

(0001) zinc cleavage surfaces were chemically etched in the manner described in Section 5.5. Their etching behaviour was observed to depend on sample purity. Previous studies by Ives and McAusland (85) had shown that the hydrochloric acid etchant produced a low density of relatively deep chemical etch pits superimposed on a high density of shallow pits. This is illustrated in Fig. 44 which is an interference micrograph of a chemically etched zinc cleavage surface. However, Ives and McAusland were not interested in ascertaining the type of defect which was associated with these deep pits.

The interference micrograph in Fig. 45(a) shows the etched cleavage surface of a zinc single crystal of 99.99% purity. The density of deep pits was about 1.6 x 10^4 cm^{-2}. On the other hand, for samples of higher purity, the density of deep pits was reduced by a factor of about ten. This can be seen by comparing Fig. 45(a) and (b), the latter of which shows the etched cleavage surface of a 99.9999% purity zinc crystal. In Fig. 45(b) a sub-grain boundary has also been preferentially etched. The pit morphologies on samples of different purity are quite similar. This point is illustrated in Fig. 46(a) and (b) which show interference micrographs of typical pits on low and high purity samples.

Little difference can be observed in the etching behaviour of 99.999% purity zinc and 99.9999% purity zinc. Each have some regions with a negligible density of deep chemical etch pits and other regions where the density of these pits was approximately 10^3 cm^{-2}. This lack of surface homogeneity in pit density distinguished the 99.9999% zinc samples from those of lower purity.

The hydrochloric acid/ethanol etchant was observed to produce etch pits at cleavage steps. This is clearly seen in Fig. 47 which shows a cleavage surface before and after a 5 second etch in the above etchant.

Very interesting etch features developed close to deformation twins. Fig. 48 is an interference micrograph of the same surface as that of Fig.12(c). Particularly noticable is the sharp change in direction of the interference fringes close to both edges of each twin. Using "white" interference fringes, this was shown to be a "groove" effect which could have been produced by an increased chemical attack in these regions.

Several samples were deformed by compression parallel to the

(0001) plane. The chemically etched surfaces were then found to be covered with bands of shallow pits as shown in Fig. 49. By referring to the directions of mechanical twins on the same surface, these bands were observed to lie along $<10\bar{1}0>$ directions. This indicates that the pits had probably formed at fresh, screw dislocations which had been introduced by deformation on the $\{11\bar{2}2\}$ $<\bar{1}\bar{1}23>$ slip system (79). The sides of deep pits in Fig. 49 are seen to lie along $<10\bar{1}0>$ directions and not the close-packed $<11\bar{2}0>$ directions, in agreement with the observations of Rosenbaum and Saffren (79).

CHAPTER 7

DISCUSSION

7.1 Introduction

The theories of evaporation employ models of actual systems which postulate the presence of surface steps. Evaporation is then described as a result of step motion (41,42). The observations reported here will be considered in the light of these theories. Refinements will be proposed where they prove inadequate to account for the observed evaporation morphology.

Evaporation pits have been produced on low index surfaces by the preferential nucleation of steps at the intersection of line defects with the surface. Evidence will be produced to show that these defects were probably emergent dislocations. A mechanism will be proposed whereby enhanced step nucleation can take place at dislocations which have been decorated by bulk impurities.

Assuming that local nucleation centres emit a train of monatomic steps, it will be shown that macroscopic ledges quickly form when a flux of impurity atoms or molecules is incident at the surface. The impurities may originate either in the vapor phase or within the substrate. The stability and motion of macroledges will be discussed in detail. In order to explain the formation of macrokinks in ledges at high surface impurity concentrations, it will be found necessary to consider step motion not only on the (0001) surface but also on the macroledge "riser".

7.2 Nucleation of Evaporation Pits

7.2.1 Evidence for Dislocations Acting as Step Sources

The observation of steep-sided "holes" at the bottom of point-bottomed etch pits and their absence in flat-bottomed pits is indicative of continuous line defects acting as step sources during evaporation. Furthermore, asymmetric pit development indicates that a number of these defects lie on low-index planes which make angles <90° with the basal plane. This would suggest that the thermal pits are associated with dislocations. In this section, several other observations which tend to point to a correspondence between dislocations and evaporation pits will be discussed.

Dislocation densities of between 10^6 and 10^8 cm^{-2} are normally reported for metals in an annealed condition, whereas the pit densities listed in Table 8 for evaporated (0001) zinc surfaces lie within the range 10^4 and 10^5 cm^{-2}, irrespective of the experimental conditions. These values therefore are somewhat lower than would be expected if a one-to-one correspondence between thermal pits and dislocations were to exist. However, the basal plane is the primary slip plane in mostly hexagonal-close-packed metals. Therefore, since only non-basal orientations would have been effective step sources in this study, a much lower density would be expected.

The observed density is in agreement with related pit densities reported by previous workers. For example, Ruff (40) observed thermal etch pit densities in the range 3.3 to 7.5 x 10^4 cm^{-2} on air-cleaved (0001) zinc surfaces. Chemical etch pit densities of 3.4 x 10^4 cm^{-2} were found on annealed cleavage surfaces of the same crystal. Rosenbaum and Saffren (79) report the observation of dislocation etch pits along glide bands in zinc single crystals which had been lightly deformed by bending along an axis parallel to the (0001) direction. An analysis of their micrograph gives a dislocation density of 4 x 10^4 cm^{-2} on (0001) planes. Again, there is good agreement with the densities reported here. An alternate method for the determination of dislocation densities was employed by Schultz and Armstrong (86) who observed dislocations in zinc single crystals by the Berg-Barrett X-Ray topograph technique. They estimated the dislocation line density in random planes perpendicular to the cleavage surface to be 10^5 to 10^6 cm^{-2}. The deviation between the densities as given by etch pit and x-ray techniques is possible because

(a) of a natural variation in dislocation densities according to sample preparation, and

(b) more than one dislocation may be associated with a single etch pit (87). An example is shown in Fig. 27(b) where three step sources can be observed at the pit bottom.

The observation of a number of thermal etch pit configurations was reported in the previous chapter. These observations can be understood if the pits formed at certain types of dislocation groups. For example, pit arrays indicative of sub-grain boundaries were frequently observed (Fig. 38). The simplest type of subgrain boundary, a small-angle symmetrical "tilt" boundary separating two regions of the crystal that differ in orientation by an angle Θ, can be formed by arrays of edge dislocations of Burgers vector $\underline{b}$ and spaced a distance, h, apart.

It can be shown (59) that

$$\Theta = \tan^{-1} \frac{|\underline{b}|}{h} \qquad (7.1)$$

Although this formula is only applicable to simple tilt boundaries, it may be used to get an estimate of the degree of misorientation at the boundary in Fig. 38. In this case h is about 10 μm and $|\underline{b}|$ is typically 2.66Å. Therefore $\Theta << 1°$. A simple tilt boundary composed of edge dislocations lying in $(10\bar{1}0)$ planes and with Burgers vector $\frac{1}{3}$ $(11\bar{2}0)$ would intersect the basal plane perpendicularly and produce an array of etch pits, such as those in Fig. 38.

In Fig. 39, the intersection of three sub-boundaries is shown. The depth of an evaporation "groove" depends upon the angle which the dislocations in the boundary make with the surface. Therefore, if the boundaries shown in Fig. 39 are each of a different type, e.g. pure tilt, pure twist or a mixture of tilt and twist components, the observed depth difference between the "grooves" can be expected (84).

Both chemical and thermal etch pits were observed at cleavage steps. Cleavage steps are formed when the cleavage crack is deflected from one atomic plane to another due to imperfect crack propagation or to lattice imperfections. Gilman (82) has suggested that the monatomic steps which remain when a cleavage step intersects an array of screw dislocations can combine to form a visible step. The screw dislocations may be "grown-in" or they may be nucleated ahead of the advancing crack. Gilman (88) has shown how dislocation loops may form just in front of the crack tip. The $\{11\bar{2}2\}$ $<\bar{1}\bar{1}23>$ slip system in zinc is operative at room temperature (89). Therefore, dislocation loops, with screw components lying in $\{11\bar{2}2\}$ planes and with $\langle\bar{1}\bar{1}23\rangle$ Burgers vectors, can nucleate just ahead of the crack tip. These dislocation loops are severed when the advancing crack cuts through them and the screw component of the loop produces a primary cleavage step of maximum height 5.66Å. Pits which form at the dislocations would be expected to become flat-bottomed after an extended period of evaporation. This was, in fact, observed (Fig. 41). The sample shown in Fig. 47(b) was chemically etched for only 5 secs. and hence insufficient material had been removed for the chemical etch pits to become flat-bottomed.

Groups of evaporation pits lying along $\langle 10\bar{1}0\rangle$ directions were shown in Fig. 40. Similar pit arrays have been observed along glide bands in chemical etching investigations. This has been taken as evidence that glide dislocations were being etched (18). Chemical etch pits lying along $\langle 10\bar{1}1\rangle$ glide bands in a heavily deformed zinc cleavage were reported in Section 6.8. (Fig. 49). If both the observed thermal and chemical etch pits correspond to dislocations, they probably result from deformation on the $\{11\bar{2}2\}$ $\langle\bar{1}\bar{1}23\rangle$ slip system during the cleavage process. If this is true, then the etch pits represent screw dislocations.

When a deformation twin is formed in a crystal, the matrix stresses which develop as a result, tend to untwin the re-orientated region. However, if they reach a sufficiently high level, some form of accommodation slip or kinking may occur. Accommodation by primary kink bands is common in hexagonal-close-packed metals. A twin with its accommodation kink is shown schematically in Fig. 57. It is seen that the lattice accommodates to the twin by bending about an axis parallel to the twin (90). The bending occurs by the formation of a low-angled tilt boundary perpendicular to the basal plane, consisting of an assembly of basal plane dislocations. Secondary accommodation kinks with traces in the basal plane normal to that of the twinning plane have also been observed (91). Rosenbaum (92) has shown that they are formed from non-basal dislocations. These facts suggest that evaporation pits which developed close to mechanical twins were nucleated at dislocations resulting from accommodation deformation during twinning. Enhanced chemical attack at these dislocations would also account for increased dissolution at the same regions during chemical etching (Fig. 48).

In summary, evidence has been presented to show that evaporation etch pits were formed at line defects which were probably dislocations. Further proof was provided by showing that the observation of various pit configurations could be understood if the pits were associated with dislocations.

7.2.2 Evidence for Impurity Precipitation at Pit Sources

There are many examples in the literature of enhanced chemical etch pit formation in metals at impurity-decorated dislocations. For example, Gilman (32) has described how the precipitation of cadmium at dislocations in zinc leads to the formation of dislocation etch pits at sub-grain boundaries and other isolated sites in an etchant composed of aqueous solutions of CrO_3 and Na_2SO_4. No pits were observed when undoped zinc crystals were employed.

In Gilman's work, zinc single crystals were grown from a melt containing 0.1% Cd as added impurity. Forty and Frank (93) have observed that precipitation at dislocations will also occur at relatively low impurity concentrations. They showed that normal bulk impurity levels in 99.999% Al were sufficient to permit insoluble impurities to precipitate at dislocations. When the samples were aged, dislocations could be revealed by chemical etching as a result of the impurity enhanced chemical reactivity of these regions.

A number of direct observations of impurity precipitation at dislocations have been made. In the best known example, Dash (94) diffused copper into silicon single crystals at 900°C. On cooling, copper precipitation at dislocations could be observed by use of infrared transmission microscopy. As chemical etch pits were formed at the points where decorated dislocation lines intersected the surface, he was able to establish a one-to-one correspondence between etch pits and dislocations.

In the investigations described here, chemical etching investigations showed that extremely shallow, shapeless pits formed at fresh dislocations (Fig. 49). In light of the observations described above, it seems likely that the deep chemical etch pits were nucleated at dislocations which had been decorated by the precipitation of insoluble impurities present in the matrix.

In Table 10 the densities of thermal macropits* and chemical macropits are compared for samples of equivalent purity. A distinct

---

* Henceforth all deep pits will be referred to as macropits.

correspondence between the variations of their densities with sample purity is seen. This correspondence strongly indicates that the presence of impurities at evaporation step sources plays an important role in their nucleation, i.e. a role in which they increase the rate of step nucleation at these sites.

An attempt was made to show that thermal macropits and chemical macropits were both associated with the same type of crystal defect. This was accomplished by marking a macropit on an evaporated sample and then chemically etching the surface in the normal manner. The pit continued to deepen during etching and, as the surface morphology evolved to that of a typical chemically etched sample, the evaporation pit became a chemical macropit. If, however, chemical macropits formed at a different type of defect, the evaporation pit would have quickly developed a shallow bottom upon etching. In addition, chemical macropits were observed to form only at the sites of evaporation macropits. These observations strongly suggest a one-to-one correspondence between chemical and evaporation macropits.

Young (95) has observed that the presence of 0.01% Te and 0.05% Sn in 99.999% copper single crystals promotes the formation of oxide nuclei at dislocations which intersect $\{\bar{1}\bar{1}2\}$ planes. No effect was observed when 0.1% Si was added to the crystals. In the present work zinc oxide nuclei appeared to have formed on the surface during evaporation runs in oxygen partial pressures $> 8 \times 10^{-7}$ torr. It is possible that the presence of large concentrations of impurities close to dislocations may have "catalysed" oxide formation in these regions at lower oxygen partial pressures. As oxide nuclei on the surface were observed to poison local evaporation, their formation at decorated dislocations would inhibit step nucleation, leading to flat-bottomed pits. In fact, an increase in the density of flat-bottomed pits was observed at oxygen partial pressures in the range 5 - 8 x 10^{-7} torr. As this "catalytic" effect would depend on the type and the density of the impurity at dislocations the observed dependence of oxide nucleation on oxygen partial pressure would be expected.

In this section, the established phenomenon of enhanced chemical etching at decorated dislocations combined with the correspondence between chemical and thermal etching observations has been used to show that evaporation macropits were nucleated at impurity decorated dislocations. The presence of impurities at step sources was also shown to explain the increase in density of flat-bottomed pits as the partial pressure of oxygen was raised.

7.2.3 Effect of Impurity Segregation at Dislocations on Step Nucleation

Equation (3.14) shows that the free energy change in forming a two dimensional embryo at a dislocation is composed of three terms, i.e.

$$\Delta G = \Delta G_{vol.} + \Delta G_{edge} - \Delta G_{strain} \qquad (7.2)$$

where ΔG_{strain} represents the decrease in free energy required for nucleus formation at a dislocation, relative to that for formation on the free surface. However, it was shown in Section 3.10 that the strain energy around a dislocation may be reduced by the segregation of suitable bulk impurities at the dislocation. Using the expression (equation 3.32) derived by Bilby (72) for the binding energy of impurities to edge dislocations, it was shown that a typical impurity, lead, in zinc, would be strongly attracted to the expanded side of the dislocations. Calculations for the other impurities which are listed in Table I give smaller but appreciable binding energies at edge dislocations in zinc. Therefore, it is quite probable that as the crystals cooled to room temperature after solidification, the segregation of solute impurities at dislocations reduced the strain energy associated with these "grown-in" dislocations. In this case, equation (7.2) is incorrect because the strain energy term, ΔG_{strain}, has been reduced by an amount ΔG_p. The corrected equation is

$$\Delta G = \Delta G_{vol.} + \Delta G_{edge} - (\Delta G_{strain} - \Delta G_p) \qquad (7.3)$$

Therefore, there is an increase in the free energy required for nucleation and hence a considerable decrease in the rate of step nucleation at dislocations. An inhibition of chemical etch-pit formation at dislocations by segregated impurities has been observed by Gilman et al. (18). They showed that grown-in dislocations produced shallow etch pits when a LiF crystal was aged and slowly cooled. Fresh dislocations, on the other hand, produced deep, well-formed pits. In metals, however, electrochemical effects may enhance the rate of chemical attack at decorated dislocations (31).

In the case of evaporation, the rate of nucleation depends only on the free energy required for ciritcal nucleus formation. As equation (7.3) shows, impurity segregation at dislocations will retard the local rate of evaporation with respect to that at a "clean" dislocation. From this point of view, segregation of impurities cannot be responsible for the nucleation of deep pits at dislocations. However, in the following sections it will be shown that due to another mechanism, the formation of impurity precipitates at dislocations may lead to an increase in the local rate of evaporation.

7.2.4 Impurity Precipitation At Dislocations

Unless high purity metals are carefully zone refined, insoluble impurities are "grown-in" to the solid phase. Then, as solid solubility normally decreases with temperature, a solid solution of increasing supersaturation will be produced as a melt-grown single crystal is cooled to room temperature. If diffusion in the parent lattice permits, precipitation of a second phase may occur.

For high supersaturations, precipitation takes place mainly by homogeneous nucleation at random lattice sites. However, for low undersaturations and high misfit energies at the boundary between the precipitate and the parent crystal, heterogeneous nucleation at dislocations will be favored because the local strain energy introduced by precipitation can be relieved by the strain fields of the dislocation. The growth of a critical nucleus will be promoted by either a compressive or tensile strain, dependent upon the particular precipitating system. Since dislocations are associated with regions of both, they should assist the formation of a nucleus (96). The precipitate will grow in a manner that is dependent upon the supersaturation and the aging treatment. Ample experimental evidence is available to show that dislocation networks do act as sites for preferential nucleation in metal as well as ionic crystals(93,94,96

Precipitation commences with the segregation of impurities to dislocations under the attractive interaction of their stress fields. A fluctuation in composition along the dislocations then leads to the nucleation of a precipitate (97). Further growth takes place by the addition of impurity atoms from the supersaturated solid solution. In this manner crystallographic rod-shaped precipitates form at dislocations (98), although for extremely low undersaturations there may be uneven precipitation along the dislocation length (94).

The quantity of data on the solid solubilities of impurities in zinc at low concentrations and low temperatures is restricted. However, the solubility data in Table 1 suggests that below 100°C, lead, iron, nickel and silicon are sufficiently insoluble to precipitate a second phase in the zinc crystals which were employed in this work. Although a semi-quantitative spectrographic analysis is not an accurate measure of the impurity concentrations, it revealed impurity levels for the above species high enough to promote precipitation. The low temperature solubilities of tin, cadmium, manganese and magnesium might also promote precipitation, but to a lesser degree. An examination of the binary phase diagrams for Zn - X (X denotes Fe, Ni, etc.) (77, 78) indicates the phases which would precipitate in supersaturated solid solutions of the above impurities. These are listed in Table 11 along with their chemical and crystallographic structures. Their stability on heating to 390° and the vapor pressures (99) of the pure elemental impurities at 390°C are listed in the fourth and fifth columns respectively. It should be pointed out that the precipitation of ternary or higher order phases is also possible.

It is informative to make an estimate of the precipitate size. This may be achieved by calculating the diffusion distance of a typical solute in zinc during the most effective stage of aging. Then, assuming that all impurities in a cylinder around the dislocation with this radius precipitate at the dislocation, one can estimate the radius of a continuous rod of these atoms.

The diffusion distance, x_i, of an atom in a time t is given by

$$x_i = (2D_i t)^{1/2} \qquad (7.4)$$

where D_i is the bulk diffusion coefficient of the component i. Using typical values (100) for D_i perpendicular to the c-axis in zinc, when aging takes place for two months at 25°C, 30 minutes at 127°C, and 15 minutes at 227°C the values of x_i are 340Å, 1047Å and 17,150Å, respectively. These conditions approximately describe the cooling stage of the crystal growth process employed. Higher temperatures are excluded as the solid solubilities at these temperatures prohibit significant precipitation.

For 99.999% zinc, there is one impurity atom per 10^5 zinc atoms. Assuming that most precipitation takes place at 200°C and using the naive model described above, it can be shown that the impurity atoms in a cylinder of unit length and radius 1.715×10^4 Å, i.e. $\pi(1.715 \times 10^{-4})^2/10^5\Omega$ impurity atoms, where Ω is the atomic volume of zinc, can condense into a circular rod of 100% impurity and radius 55Å. This calculation has used only approximate aging conditions, ignored growth kinetics and assumed a zinc-free precipitate. Allowing for nucleation and growth kinetics would decrease the radius whilst considering a zinc-rich phase would increase the radius. However, the above values are an indication of the order of magnitude.

7.2.5 Enhanced Evaporation at an Impurity Precipitate

When a crystal with impurity precipitation along dislocations is heated, a number of things can happen at the precipitates. In this section their effects on the local rate of evaporation will be considered.

7.2.5.1 Decomposition of Unstable Compounds

True chemical compounds may precipitate at dislocations (98). If they decompose below the evaporation temperature, hollow cylinders would result at these sites, producing a ready source of evaporation steps. However, an inspection of possible precipitates (Table 11) which may have been present in the zinc samples, shows that no true chemical compounds could have precipitated. Those precipitates which are unstable below 390°C are unstable only with respect to dissolution in the zinc matrix. They will, therefore, have very little effect on local evaporation rates

There is a possible zinc compound precipitate which has not been discussed, i.e. Zn_3N_2. Although nitrogen is sparingly soluble in zinc (78), a sufficient amount may have dissolved in molten zinc during growth, segregated to dislocations after solidification and formed a Zn_3N_2 precipitate. The precipitate would decompose at 350°C in vacuum (78) and almost certainly affect the vaporization kinetics. However, although small quantities of nitrogen were evolved when the crystals were cleaved in vacuum it is unlikely that Zn_3N_2 precipitation had taken place because

(a) Zn_3N_2 can only be produced with great difficulty (78) and (b) some results of Wain and Cotrell (73) on yield points in zinc show that very little nitrogen would have dissolved in the crystals during growth. They observed yield points which they believed to be a consequence of dislocation pinning by nitrogen atmospheres around the dislocations. However, they were only present in crystals grown from molten zinc through which nitrogen had previously been bubbled. They were totally absent when the samples were grown from 99.999% Zn in a nitrogen atmosphere identical to the growth conditions of the present work.

7.2.5.2 Precipitates with High Vapor Pressures

Table 11 shows that precipitation from supersaturated solid solutions of Si, Ni, Pb, Sn and Cd in Zn produces precipitates of the pure elements. This is a consequence of zinc having an extremely low solubility in these metals. As the vapor pressure of zinc at 390°C is 7×10^{-2} torr, all the above elements, except Cd, have lower vapor pressures than zinc at the evaporation temperature (Table 11). Therefore, a lower rather than an increased evaporation rate would be expected at these precipitates. Only Cd precipitates would have a higher rate of evaporation than a pure zinc surface. However, as cadmium is increasingly soluble in zinc above 100°C, cadmium precipitates will dissolve into the zinc-rich terminal phase as the temperature is raised during an evaporation run.

The other impurities Fe, Ni, Pb, Mn and Mg each precipitate in a zinc-rich phase. The vapor pressure, p_i, of an element i in an alloy system is

$$p_i = a_i \, p_{oi} \qquad (7.5)$$

where a_i is the activity of i for a given alloy composition and p_{oi} is the vapor pressure of the pure i component. In Table 11 it is seen that at 390°C these impurities have vapor pressures very much less than that of zinc. Therefore, as $a_i < 1$, enhanced evaporation at these precipitates is not possible. A decrease in the local evaporation rate would again be expected as a_{Zn} is less than unity in these alloys. In the absence of any other process which might produce enhanced evaporation at emergent precipitates, a small evaporation hillock would form at these points. It will be shown in the following section that enhanced evaporation by another mechanism was possible. Nevertheless, hillocks would still be expected where a pure precipitate intersects the basal surface. No hillocks were observed on any of the vacuum-evaporated 99.999% zinc samples but they were observable on the 99.99% Zn sample (Fig. 32). It is possible that in pure samples, the elemental preciptates, if present, were not large enough to effectively poison step motion on the surface, so as to produce a hillock.

7.2.5.3 Evaporation at Small Precipitates due to Gibbs-Thomson Effects

Herring (70) has shown that, at elevated temperatures, a groove will develop at the intersection of a non-coherent boundary with a flat surface. The groove results from a minimization of the total interfacial free energy at the boundary. It has been shown (68) that this will be achieved when the three interfacial energies, σ_{Zn}, σ_{ξ} and $\sigma_{Zn\xi}$ (Fig. 50(c)) satisfy the equilibrium relationship

$$\sigma_{Zn\xi} = \sigma_{Zn} \cos\phi + \sigma_{\xi} \cos\Theta - \frac{\partial \sigma_{Zn}}{\partial \phi} \sin\phi - \frac{\partial \sigma_{\xi}}{\partial \theta} \sin\Theta \qquad (7.6)$$

The only zinc-rich precipitates included in Table 11 which will be stable at 390°C are $FeZn_{13}$ (ξ) and Ni_4Zn_{31} (δ). As both have non-coherent phase boundaries with the zinc matrix, it is highly probable that thermal grooves formed at these boundaries during an evaporation run. This is shown schematically in Fig. 50(a) and (b). If the precipitate had a small cross-sectional area, a tip, having an extremely small radius of curvature, will be formed by interphase-boundary grooving at each precipitate. This curvature of the tip will result in a local increase in the chemical potential, given by (70)

$$\mu - \mu_o = \Omega \{ K_1 (\gamma + \frac{d^2\gamma}{d\phi_1}) + K_2 (\gamma + \frac{d^2\gamma}{d\phi_2}) \} \qquad (7.7)$$

where the various symbols have already been discussed in Section 3.9. It was also shown in Section 3.9 that when γ is isotropic and the tip is spherical with radius R, the above equation reduces to

$$\mu - \mu_o = \frac{2\gamma\Omega}{R} \text{ , the Gibbs-Thomson equation} \qquad (7.8)$$

The assumption that the surface energy, γ, is isotropic is justified if the surface of the tip is on the average a high-index orientation, when $\frac{d^2\gamma}{d\phi_1}$ and $\frac{d^2\gamma}{d\phi_2}$ are small. This condition probably holds for the present application.

As $\Delta\mu = kT \ln p/p_o$, the vapor pressure p of a curved surface relative to that of a flat surface, p_o, can be expressed as

$$p/p_o = \exp \frac{2\gamma\Omega}{RkT} \qquad (7.9)$$

Before this equation can be used to calculate the zinc vapor pressure at the tip, it must be modified to allow for the fact that the zinc concentration is less than 100%. Combining equations (7.5) and (7.9) gives

$$p = a_{Zn}\, p_o{}' \exp\left(\frac{2\gamma\Omega}{RkT}\right) \qquad (7.10)$$

where a_{Zn} is the activity of zinc in the precipitated phase and $p_o{}'$ is the vapor pressure of a flat, pure zinc surface. In $FeZn_{13}$ and Ni_4Zn_{31} intermetallic compounds $a_{Zn} \simeq 0.9$. Taking $\gamma \simeq \gamma_{(10\bar{1}1)} = 1000$ ergs cm^{-2} (46) and $\Omega = 1.5 \times 10^{-23}$ cm^{-3} (101), $p/p_o \simeq 1.75$ for R = 50Å and T = 663°K. When R is 100Å, p/p_o becomes 1.25. Therefore, as this is the range of values that is expected for R, it is readily seen that if a curved tip develops in the manner described above, a substantial increase in the local rate of evaporation will result. However, this will only be true for precipitates which have compositions that are zinc-rich.

7.2.6 Model for Step Nucleation at a Decorated Dislocation

Based on the discussion of the previous section, the following model is proposed to describe step nucleation at decorated dislocations.

When the sample temperature is raised, thermal grooves develop at the precipitate-zinc boundary. As the precipitate diameter is about 50Å, a tip with a high surface curvature forms at the end of the rod-shaped precipitate. Consequently, the chemical potential of the tip relative to that of the basal surface is large. Driven by this chemical potential difference, the tip tries to reduce its chemical potential by reducing its curvature. At low temperatures, the required material transport occurs by surface diffusion but at 390°C, evaporation of atoms from the tip is the primary process. At 390°C, the system is not at equilibrium. However, a quasi-equilibrium may be maintained at the phase boundary. As a result, the groove deepens further in an attempt to counteract the decrease in surface curvature which would upset the equilibrium condition represented by equation (7.6) and depicted in Fig. 50(c).

Eventually, equilibrium is established between the two processes and the tip recedes at a constant rate and with a permanent shape. The enhanced rate of evaporation from the tip produces a steep-sided "hole" in the surface. This is illustrated in Fig. 50(d). The face of the "hole" has a slope which is determined initially by the angle ϕ (Fig. 50(c)) but which is modified by evaporation from the sides. A possible circular "hole" might be 1 μm deep and have a side slope of 60°. Such a "hole" would intersect the basal surface on a circle of diameter 2 μm, which is approximately equal to the "hole diameters" which were observed in the scanning electron micrographs (e.g. Fig. 35(a)).

A modification would be expected if the precipitate intersects the surface at an angle less than 90°. The "hole" would have a steep slope on one side and a relatively shallow slope on the other, as shown in Fig. 50(d). Asymmetric holes, similar to that shown in Fig. 35(a), would be expected.

During evaporation, there may be dissolution of the precipitate in the matrix due to increased solubility at elevated temperatures. However, the effect of dissolution would be to increase the curvature of the tip and hence increase the rate of evaporation from the tip. It will be shown later that this would only have had a minor effect on pit morphology.

As the intersection of the "hole" with the basal surface is equivalent to an unprotected crystal edge, a powerful source of monatomic steps has been produced. The motion of these steps on the surface will be discussed at length in later sections.

7.2.7 Enhanced Dissolution by Chemical Action at Decorated Dislocations

A number of models have been proposed to account for enhanced chemical attack at impurity decorated dislocations. Vermilyea (31) has suggested that it is primarily an electrochemical effect. In this case, impurity segregation or precipitation at dislocations produces local changes in electrical potential differences at the crystal-solution interface. Then, as metals dissolve as positive ions, a change in the local rate of dissolution will take place. For example, if the impure matrix close to a dislocation is anodic with respect to the pure matrix, enhanced dissolution at the dislocation will be observed.

Alternatively, as dissolution of metals either begins by the breakdown of a surface oxide film or proceeds by diffusion through one, an impurity precipitate may facilitate an increased rate for these processes (93).

7.2.8 Step Nucleation at Shallow Pits

Shallow pits which were observed on evaporated surfaces could have been formed at undecorated dislocations. Such dislocations may be introduced by deformation during cleavage, e.g. along glide bands (Fig. 40) and in the proximity of deformation twins (Fig. 36(b)). On the other hand, they may have been dislocations which were decorated at room temperature by impurities that are soluble at higher temperatures.

As was stated previously, the $\{11\bar{2}2\}$ $\langle\bar{1}\bar{1}23\rangle$ system is the major non-basal slip system operative in zinc at room temperature. Therefore, any dislocations produced by deformation in this slip system must, by simple geometry, contain a screw component if they intersect the basal (cleavage) plane. Cabrera and Levine (43) have shown that steps emanating from a screw dislocation have a ledge separation,

$$\lambda = 19\ \rho_c \qquad (7.11)$$

close to the centre, where ρ_c is the critical radius of a two-dimensional disc-shaped nucleus on the perfect surface. In Section 3.5.1, it was seen that

$$\rho_c = - \frac{\gamma\Omega}{kT\ell n\ p/p_e} \qquad (7.12)$$

where the symbols have their usual meanings. It is difficult to make an accurate estimate of p/p_e. However, taking $\gamma = 600$ ergs cm^{-2} (46), $\Omega = 1.5 \times 10^{-23}\ \mathrm{cm}^3$ (101), $k = 1.38 \times 10^{-16}$ ergs/°K , $T = 663$°K and $p/p_e \sim 10^{-4}$, then $\rho_c \sim 1$Å. Although macroscopic nucleation theory is no longer credible at these dimensions, it is evident, in any case, that a pit which forms at a screw dislocations will, from equation (7.11), have a relatively large slope (∿ 2.9°) close to its centre. Impurity effects will further increase the slope (Section 3.7). This possibly explains why steep-sided "pits" were observed (Fig. 35(b)) at the bottom of shallow pits, in contrast to the deep "holes" which were observed in deep pits.

Steps could have been produced at undecorated edge dislocations by strain-energy enhanced nucleation of two-dimensional holes in the surface (Section 3.5.2), leading to pit formation at these sites. In fact, Johnston (16) has pointed out that etch pits which form at screw dislocations may also be due to two-dimensional nucleation because in chemical etching studies, pits are produced as readily at edge dislocations as at screw dislocations.

The critical undersaturation required for the formation of disc-shaped hole on the perfect surface is

$$p/p_e = \exp - (\pi\gamma^2\Omega h/65\ k^2T^2) \qquad (7.13)$$

where each quantity has already been defined in Section 3.5.1. Using $h = 2.66\text{Å}$, $\gamma = 600$ ergs cm^{-2}, $\Omega = 1.5 \times 10^{-23}\ \text{cm}^3$, $k = 1.38 \times 10^{-16}$ ergs /°K and $T = 663°\text{K}$, one finds that $(p/p_e)_{crit} \simeq 0.4$. As $(p/p_e) << 0.4$ for free evaporation, substantial step nucleation by this mechanism was possible in the present work. The classical value for the concentration, n*, of nuclei of critical size is (7)

$$n^* = n_o \exp(-\Delta G^*/kT) \qquad (7.14)$$

where n_o ($\simeq$ surface atom density) is the number of nucleation sites on the surface and ΔG^*, the free energy of formation of the critical nucleus. As ΔG^* is small for the high temperatures and undersaturations used in this investigation, n* would have been large. Therefore, two-dimensional nucleation on the perfect surface would have led to general surface evaporation rather than pit formation.

7.3 Motion of Monatomic Steps on a Low-Index Surface

In the preceding sections it was shown that "curvature-enhanced" evaporation at zinc-rich precipitates produces steep-sided "holes" on the surface. As the intersection of these "holes" with the basal surface is analogous to an unprotected crystal edge, they would provide a ready source of monatomic steps during evaporation (41). A theoretical description of the advance of monatomic steps arising at crystal edges has been given by Hirth and Pound (41) and should be directly applicable to the present system.

Therefore, steps emanating from "holes" accelerate across the surface and asymptotically approach a limiting velocity. This is illustrated in Fig. 51(a). For clean surfaces, the terminal velocity is reached at a distance $X_o \simeq 10\ \lambda_o$ from the source, where $\lambda_o = 6\ \bar{X}$ is the terminal step spacing, $\bar{X}$ being the mean adatom diffusion distance on the close-packed terrace.

Similarly, at other step sources, such as screw dislocations, if the initial step spacing, λ, is less than $6\bar{X}$, the steps accelerate until the terminal spacing, λ_o, is attained. If, however, $\lambda > 6\bar{X}$, the steps maintain this spacing as they move across the surface.

In order to make an estimate of the step spacing, it is necessary to evaluate $\bar{X} = \{D_s/(\nu\exp - W_s/kT)\}^{1/2}$, where D_s is the surface diffusion coefficient, ν the atomic vibration frequency and W_s the activation energy for transfer of an adatom to the vapor. A calculation for (0001) zinc surfaces at 390°C results in $\bar{X} = 150\text{Å}$. Consequently, the steps should reach a terminal spacing of 900Å at a distance of about 0.9μm from the source. Therefore, a pit should form, the slope decreasing with distance from the centre to a value $h/6\bar{X} = 0.0028$.

However, pit slopes much greater than 0.0028 and macroledges instead of monatomic steps were observed. Obviously, other factors must be taken into consideration if the observed pit morphologies are to be understood.

7.4 Formation and Stability of Macroledges

In this section, various mechanismswhereby macroscopic ledges can be formed from a train of monatomic steps will be considered. It will be shown that the most satisfactory explanation of the present observations is given by a mechanistic model which allows a qualitative understanding of ledge height upon the level of surface impurity.

As similar effects on the evaporation morphology were produced by both the bulk and gaseous impurities, the term "impurity" will be used in the discussion to mean impurities from either source, unless the source is specifically mentioned.

7.4.1 Surface Free Energy Control of Surface Morphology

A surface in equilibrium with its vapor will take up a minimum surface free energy configuration at elevated temperatures (51). For small displacements from equilibrium, surface free energy arguments may be justified but when a system is far from equilibrium, e.g. during free evaporation, their validity is questionable. However, if a quasi-equilibrium is maintained on the surface, the evaporation morphology may be that which gives the minimum surface free energy.

It is assumed that steps emanating from all sources initially obey the predictions of Hirth and Pound (41,42). Therefore, a surface orientation close to that of the basal plane is produced. This orientation may correspond to the point S in the γ-plot (Fig. I). It was shown in Section 3.3 that the orientation S is unstable with respect to surface energy faceting, i.e. it will break up into (0001) terraces and a complex plane whilst maintaining the same macroscopic orientation. If impurities are adsorbed at ledges, the free energy of vicinal orientations is reduced as a consequence of equation 3.3. Increasing the surface impurity concentration can result in a corresponding decrease in the surface-free energy anisotropy. At some point, it could disappear altogether and facets would no longer be observed on the surface.

The present observations are in agreement with these predictions. For small surface impurity levels, well-defined facets develop on pit faces. As the surface excess of impurity was increased, faceting disappeared altogether as expected. However, there are two major reasons why this explanation of macroledge formation is unsatisfactory. First, the theory is unable to make any predictions about ledge heights and ledge separations, and secondly, the pit slope should be identical to that of the unfaceted surface. This should be the value predicted by the Hirth-Pound theory. However, pit slopes of between 3° and 6° were observed, in contrast to slopes of 0.15° which would be expected (Section 7.3).

In an analogous manner, a two-dimensional [0001] zone polar-plot of ledge free energy can be used to predict the equilibrium ledge structure. In the case of zinc, the ledge free energy plot will have cusps at <11$\bar{2}$0> poles, i.e. corresponding to the most closely packed ledges. On this basis, the observed hexagonal ledge structure would be expected on a clean surface. The adsorption of impurities at ledge kinks will reduce the ledge-free energy anisotropy. Therefore, at high surface impurity levels, there will be a tendency towards round evaporation pits. Although there was a departure from a hexagonal pit shape with increasing impurity concentrations, it was not a true "rounding" effect, as the apparent "rounding" was observed to be due to a build up of macrokinks at pit corners (e.g. Fig. 18(b)). True pit "rounding" which was observed at high impurity levels can be attributed to miscellaneous kinetic processes which occurred on the surface, e.g. the formation of ZnO nuclei (Section 7.6).

It is apparent that the evaporation morphology is not a configuration of minimum surface free energy. In later sections, it will be suggested that kinetic effects control the evaporation morphology. However, it is possible that evaporation features which are representative of an equilibrium surface are produced but these features will be transitory because of their kinetic instability at high undersaturations (102).

7.4.2 Non-Uniform Impurity Distribution along a Dislocation

Gilman (103) observed terraced sides in chemical etch pits at aged dislocations on (001) LiF cleavage surfaces, whereas smooth sides developed in pits at fresh dislocations. At the centre of each terraced pit, a string of small particles could be seen and each time a new terrace was observed, a new particle appeared at the centre of the pit. As the ledge heights (2000 - 4000Å) and the particle diameters were of the same order of magnitude, he concluded that an uneven impurity precipitation along the dislocation produced an uneven rate of step nucleation at the dislocation. Hence, macroledges were formed.

The application of this model to the present case is unsatisfactory. In contrast with Gilman's observations, macroledges developed in all etch pits, including those at fresh dislocations. Also, the model which has been proposed for step formation at aged dislocations during evaporation predicts that a "hole" will develop in the surface at the impurity precipitate. As the depth of the "hole" is probably much greater than the impurity "spacing" along the dislocation, only small effects on the pit morphology would be expected because the impurity precipitate would have "recovered" before the "hole" could have disappeared. As long as the "hole" exists, a ready source of monatomic steps is maintained. The rate of step formation should be only slightly affected by the depth of the "hole".

7.4.3 Mechanistic Model for Macroledge Formation

It is obvious that the motion of monatomic steps during evaporation will be considerably modified in the presence of surface impurities. A mechanistic model for evaporation from an impure surface will now be proposed. The model assumes that an equilibrium impurity concentration (< one monolayer) is maintained on the surface during evaporation. When the impurity source strength is changed, e.g. by changing the sample purity, the surface impurity concentration is assumed to undergo a corresponding change.

The impurity atoms form part of the two-dimensional surface matrix. As the evaporation steps sweep across the surface, these impurities eventually assume positions in the steps. If the rate of removal of an impurity atom from a site in the step to an adatom position is much less than that for zinc atoms, step motion at these positions is effectively blocked. When the concentration of impurities along steps is large, the step velocity is reduced to a value given by (64)

$$v = v_o \, (1 - 2 \, \rho_c/_d)^{1/2} \qquad (7.15)$$

where v_o is the step velocity in the absence of impurities, d the distance between impurity sites in the step and ρ_c the radius of the critical two-dimensional nucleus on a clean surface. It is seen that impurity retardation of steps will be excessive when $d \sim 2\rho_c$. In Section 7.2.8, it was shown that $\rho_c \sim$ interatomic dimensions. Therefore, for small impurity levels (<< one monolayer) only small effects should be observed. However, as impurity atoms have a relatively long "lifetime" at step positions, the impurity concentration at the step builds up as the latter traverses the surface. Eventually, the concentration will be sufficient to effectively retard step motion.

On a clean surface, steps emanating from a given ledge source accelerate across the surface and attain a terminal velocity in the manner described previously (Fig. 51(a). In the presence of surface impurities, the steps are retarded as described above. Consequently, they lag behind their equivalent position on a clean surface. From the preceding discussion, it is obvious that the magnitude of the retardation increases with the distance the step has travelled from the source, as shown in Fig. 51(b). At some point, an impurity-induced fluctuation causes one or more steps to bunch (Fig. 51(c). If the bunch does not dissociate before a major "pile-up" of steps can take place a multiatomic ledge forms (Fig. 51(d) and (e)).

The question then arises as to why the initial step bunch is stable for a time that is sufficiently long to allow a multiatomic ledge to form. This can be understood by considering the movement of atoms away from steps in a bunch similar to that shown in Fig. 51(g). The kinetics of crystal growth from the vapor involves the steps (a) adsorption on the surface, (b) surface diffusion, and (c) movement into kink positions, i.e. the opposite of the steps involved in evaporation. If the step separation, λ, is less than the diffusion distance of adatoms on the terrace, the rate of incorporation of atoms into ledges depends on λ. By the principle of microscopic reversibility (122), the motion of atoms from the steps $k + 1$ and $k - 1$ (Fig. 51(g)) to sites on the terraces separating them from the step k is retarded because the small step spacings reduce the number of sites to which the atoms can diffuse. Therefore, atoms escaping from these steps travel mostly in the indicated directions. If the escape probability for atoms moving to the terrace in front of the step is greater than that for atoms moving to the terrace above the step, the velocity of the step $k - 1$ would be greater than that of the step $k + 1$. Therefore, steps at the rear of the bunch are moving more rapidly than steps at the front. Consequently, the bunch is stable with respect to dissociation into monatomic steps. The macroledge then grows by the accretion of steps into the bunch until a second ledge is formed by the same process, Fig. 51(f). Succeeding macroledges are produced in a similar manner.

By considering a simple ball model of a surface step, the assumption of a direction dependent escape probability can be justified qualitatively. It is shown in Fig. 51(h) that an atom at a step position "c" can move either to a terrace site "b" or alternatively to a site "a" on the upper terrace. Schwoebel (104) has considered this problem for an arbitrary surface and showed that, for an adatom diffusing on the surface, the potential maximum at A could be increased relative to that at B due to coordination differences between the positions A and B. An analysis of a ball model of a step in a <11$\bar{2}$0> direction on a (0001) zinc surface shows that, for both the above diffusion processes, the atom is removed from a surface site with coordination number 5 to one with coordination number 3, having gone through intermediate sites at A and B respectively with coordination number 2. At first sight, it would appear that the energies required to move an atom from "c" to either "a" or "b" are equal. However, there is a subtle difference in the paths which must not be overlooked. An atom moving from a site "c" at the step to a site "a" in the upper terrace goes through a potential maxima somewhere between the positions A' and A (Fig. 51(h)). The distances which the atom must travel to go from "c" to A' or from "c" to A are $\sim \frac{c}{2}$ (= 2.47Å) and $\{\frac{c}{2} +^{)} \sqrt{3}\, a/4$ (=1.15Å)} respectively. The energies required to move the atom to A and A' represent the maximum and minimum values of the potential in this path respectively. On the other hand, the distance an atom must move from "c" to the potential maximum at B is $\sqrt{3}\, a/4$. Assuming that the atomic forces which attempt to hold the atom at "c" are equivalent for both paths, the energy required to move an atom from "c" to either A or A' is obviously greater than that required to move the atom from "c" to B. As a result, there is an increase in the potential barrier at A (or A') associated with a diffusing atom, as shown in Fig. 51(i). The increased energy required for atoms to move to sites on the upper terrace results in the probability of this process being lower than that for atoms moving to positions "b", which is the condition required for the stability of a step bunch. Ehrlich and Hudda (121) using a field ion microscope to investigate surface self-diffusion on tungsten have observed a diffusion barrier at steps. When adatoms approached the edge of a plane on the tungsten tip, they were reflected, as a consequence of the additional activation energy needed to cross the step onto the next plane.

As a macroledge can only form at a certain distance from the source, i.e. where the impurity concentrations at the steps is sufficient to stabilize a macroledge, the number of steps contained in this distance determines the height, H, of the macroledge. The distance which the first ledge travels before the second bunch forms determines the ledge separation, λ_m. It follows that when the surface impurity concentration is increased, the ledge height and ledge spacing should both decrease. In fact, such an effect was observed when the sample purity was decreased and also when the partial pressure of oxygen in the vapor phase was increased. The relative roles of bulk and gaseous impurities will be discussed later.

It is evident from Fig. 51(b) that the mean surface slope of a monatomic step train is greater in the presence of impurities than that predicted by the Hirth-Pound theory for a clean surface. A macroledge, once formed, will traverse the surface at a velocity which is much less than that of a monatomic ledge. Therefore, the development of stable macroledges results in a sharp increase in the pit slope. This is illustrated by the full and dashed lines in Fig. 51(e) which show the slopes of the actual pit face and that of a Hirth-Pound pit respectively. This provides an explanation for the observed pit slopes being between 3 and 6° rather than the 0.15° predicted by Hirth and Pound (41,42).

7.4.4 Structure of the Macroledge

Andrade and Randall (25) observed faceted thermovacuum pits on (0001) surfaces of cadmium single crystals. Using an optical goniometer they determined the pit faces to be (0001) terraces separated by regions composed of $(10\bar{1}1)$ planes. $(10\bar{1}1)$ macroscopic ledges have also been observed by Straumanis (105) for the platelet growth of zinc crystals from the vapor. A Unitron microgoniometer was used to determine if the "risers" of the macroledges observed in the present study were low index planes. No reflections could be observed at $(10\bar{1}1)$ poles.

However, on using the microgoniometer for other applications, it was observed to be only sensitive to the macroscopic surface orientation and not that of microscopic features of this magnitude. (The ledges reported here are smaller by a factor of 10 than those observed by Andrade and Randall (25)). Therefore, it cannot be concluded that the macroledges have not low-index orientations. In fact, several observations suggest that they probably have, for example:

(a) Scanning electron micrographs of macroledges reveal no observable structure in what appear to be flat surfaces. This point is illustrated in Fig. 15. It should be pointed out, however, that the resolution of the instrument is limited to about 200Å.

(b) An assumption that the macroledge is a low-index plane leads to a model for evaporation of a faceted surface which agrees with the observed ledge morphologies at high surface impurity concentrations (Section 7.5).

If the macroledge is a low-index surface, it is probably the $(10\bar{1}1)$ plane, as reported by Andrade and Randall (25) for cadmium. This follows from the work of Stranski et al. (26), who showed by a bond model calculation that after $\{0001\}$, $\{10\bar{1}1\}$ surfaces were the next most stable. Low-index macroledge surfaces are stable during evaporation because any deviations from these orientations produce surface atoms which evaporate more rapidly than those in the low-index plane. Consequently, after sufficient evaporation, the complex plane moves to the nearest low-index orientation which is stable. It should be remembered that the macroledge is only formed in the presence of surface impurities and is not part of the configuration of minimum surface-free energy.

The coordination numbers of atoms in alternate $(10\bar{1}1)$planes are different. Successive planes have 8 and 6 nearest neighbours respectively, as is illustrated in Fig. 52(a) and (b).

7.4.5 Impurity Sources

The observations reported in the previous chapter indicate that both gaseous and bulk impurities have similar effects on the evaporation morphology. It is probable that, during evaporation, impurities from both sources are present on the surface. In this section, the relative importance of gaseous and bulk impurities will be discussed.

The principal species which were present during both stages of a vacuum evaporation run are listed in Tables 4 and 5. Trapnell (106) has reported that of the gases N_2, H_2, CO, C_2H_4, C_2H_2 and O_2, only

O_2 chemisorbs on zinc. The other species are only physically adsorbed. The mean lifetime, τ, of an adsorbed atom on the surface is given by $1/\tau = \nu \exp -(U/kT)$ where ν is the vibrational frequency of adsorbed atoms and U is their activation energy for desorption. For U = 6 kcal/mole (107) and $\nu = 10^{13}$ $\sec^{-1}$, the mean lifetime of a physically adsorbed species on zinc at 390°C is about 10^{-11} secs. In comparison, for a chemisorbed species, U = 65 kcal/mol (107) and $\tau \simeq 10^{+8}$ secs. Consequently, the population of physicaly adsorbed gases on zinc would have been negligible at the small partial pressures given in Tables 4 and 5 in agreement with the observation of Rhodin (108) who reported that nitrogen monolayer coverage on zinc at 90°K was only possible for nitrogen pressures greater than 10^{-2} torr. Therefore, those gases which physically adsorb on zinc would have had little effect on the evaporation morphology in the present work.

Of the gases listed in Tables 4 and 5, only CO_2 and H_2O chemisorb on zinc. The reactions

$$Zn + CO_2 \rightarrow ZnO + CO \qquad (7.16)$$

and

$$Zn + H_2O \rightarrow ZnO + H_2 \qquad (7.17)$$

are possible at 390°C if $p_{CO}/p_{CO_2} \leq 5 \times 10^5$ and $p_{H_2}/p_{H_2O} \leq 2 \times 10^7$ respectively (68). It can be seen in the above tables, that these conditions were satisfied in the present work.

For a gas present at a pressure, p, the flux, J, of molecules incident on the surface is given by the equation,(109)

$$J = \frac{p}{(2\pi mkT)^{1/2}}$$

where m is the molecular weight of the gas molecules and T the gas temperature. Using this equation, one finds that during the electron bombardment and evaporation stages the combined fluxes of CO_2 and H_2O molecules onto the zinc surface were 0.005 and 0.0025 monolayers/sec. respectively. Therefore, assuming accommodation coefficients of unity, the total possible surface coverage during an evaporation run is approximately equal to 1.5 monolayers. Although accommodation coefficients less than one are normally observed for metal surfaces (110,111), there was some evidence to indicate that adsorption did take place, at least during the electron bombardment stage. When large exposures* (10^{-4} torr. sec) occurred during electron bombardment, a surface film formed. This film only permitted evaporation from isolated centres such as cleavage steps (Fig. 41). The evaporation temperature of these surfaces was unknown but it was probably much less than 390°C. The mass-spectrometric observations (Section 6.1) showed that during each evaporation run, considerable gas desorption from the sample occurred just before the evaporation temperature was reached. The main species evolved was H_2O. It is probable that CO_2 and H_2O molecules are initially weakly adsorbed (but more strongly than in physical adsorption) onto the surface. The above reactions (7.16 and 7.17) then take place at a rate determined by the respective reaction rate constants. It is known (68) that these reactions are slow when compared with the reaction

$$Zn + \frac{1}{2} O_2 \rightarrow ZnO \qquad (7.18)$$

---

* Exposure is defined as the product of the pressure and time of exposure. It is normally given in units of torr-sec.

Therefore, it is possible that at temperatures > 300°C, if most of the CO_2 and H_2O has not reacted with the zinc surface, these species are either thermally or dynamically desorbed. Dynamical desorption would occur when the evaporation flux from the surface is large.

With the development of sophisticated techniques in surface research, e.g. L.E.E.D.*, Auger Spectroscopy, etc., observations of bulk impurity diffusion to the surface have been frequently reported (112). For example, Boggio and Farnsworth (113), during ion bombardment in a L.E.E.D. system, observed faceting parallel to a {130} plane on a {110} tantalum face which had previously been heat - treated at 1450°C. However, Farnsworth et al. (114) have more recently reported that faceting on {110} Ta faces does not occur when the samples have been heat-treated at 2150°C. They conclude that the faceting formerly observed was caused by bulk contaminant which had not been removed by heat treatment and had diffused to the surface during the experiment. This suggestion was supported by the observation that the (310) face of molybdenum developed facets concurrent with observable bulk impurity diffusion to the surface when heated at or above 1500°C.

Therefore, it seems probable that at elevated temperatures, bulk impurities out-diffuse to the surface in substantial quantities (112) and consequently provide a plentiful supply of impurities during evaporation. In a time period, t, a simple relationship gives the average diffusion distance, $\bar{x}$, of an impurity atom in the solid state as

$$\bar{x} = (2\ Dt)^{1/2}$$

---

* Low energy electron diffraction

where D is the diffusion coefficient of the impurity. Using typical data for impurity diffusion parallel to the c-axis in zinc (100), gives $\bar{x}$ = 390μm at 390°C when t = 1 sec. Assuming all impurities within 3μm of the surface out-diffuse during one second, the surface flux of impurity atoms in 99.999% zinc crystals is 0.01 monolayers per sec. This value is probably a lower limit, since the as-grown samples probably have higher impurity levels than truly 99.999% zinc crystals. Therefore, the crystal substrate is potentially a more powerful source of impurities during evaporation than the vapor phase. This conclusion is supported by the large adjustments in the ledge height and ledge spacing (Table 8) when the bulk impurity contents were changed. However, the gaseous impurities should also contribute, but to a lesser degree, to the total surface impurity population.

Diffusion of impurities to the surface reduces the total free energy of the system by an amount ΔF. ΔF includes the reduction in the surface-free energy (equation 3.3) and the reduction in the free energy of the substrate phase if the impurities were present in supersaturated solution. The analogy between impurity segregation to the surface and that to a dislocation (Section 3.10) is readily seen. In a similar manner to the latter case, an equilibrium surface impurity concentration, S, will be maintained where S is given by, (115)

$$S = B \exp -\Delta F/kT \qquad (7.19)$$

and B is the bulk impurity concentration. Therefore, relatively insoluble impurities diffuse to the surface as the temperature is raised.

At any temperature, and 390°C in particular, an equilibrium surface impurity concentration is attained. These impurities then affect the motion of evaporation steps on the surface in the manner discussed in previous sections. It is assumed that the desorption rate of impurities from the surface is small. This is true for most of the impurities listed in Table 1.

During evaporation runs in high oxygen partial pressures, oxygen adsorbs on the surface and adds to the surface impurity concentration. Following Uhlig's (107) description of oxygen adsorption on clean surfaces, molecular oxygen initially adsorbs on the zinc surface. It then dissociates into atomic oxygen which chemisorbs on the surface. The oxygen atoms may penetrate the surface layer to give a two-dimensional zinc-oxygen matrix. (116). As the solubility of oxygen in zinc at 390°C is negligible (117) the solution of oxygen in the zinc can be neglected.

At an oxygen partial pressure of 10^{-7} torr, the flux of oxygen molecules striking the surface is about 0.03 monolayers per sec. Even allowing for accommodation coefficients << 1, there is obviously a considerable increase in the surface impurity concentration. The mechanism proposed in Section 7.4.3 for macroledge formation would predict that, at high oxygen partial pressures, the ledge heights and ledge spacings are reduced from their values during vacuum evaporation. The results in Table 8 are in agreement with this conclusion.

Similarly, when samples of lower bulk purity are used, the flux of impurity atoms to the surface is increased and consequently the equilibrium concentration of impurities on the surface is increased. The ledge spacings and ledge heights show the expected decrease (Table 9).

Once again, the point is illustrated that any surface impurity, irrespective of its source, affects the ledge morphology provided the impurity to zinc bond is stronger than the zinc to zinc bond.

A number of observations at high oxygen partial pressures cannot be understood without making certain assumptions regarding the adsorption of oxygen on the evaporating surface.

(a) L.E.E.D. studies of oxygen adsorption on clean metal surfaces (107) have shown that the concentration of oxygen on the adsorbent normally increases with exposure time. Uhlig (107) suggests that the formation of ZnO nuclei should commence at a surface coverage of less than one monolayer. During an evaporation run in an oxygen partial pressure of 5×10^{-7} torr, the maximum quantity of oxygen which could adsorb on the surface is about 30 monolayers. Hence, oxide nucleation would be expected at oxygen partial pressures much lower than this value. However, it was not possible to resolve oxide nuclei on evaporating zinc surfaces with the techniques employed in the present study unless $p_{O_2} > 8 \times 10^{-7}$ torr.

(b) If the quantity of adsorbed oxygen is a function of surface exposure, it follows that the concentration of oxygen on pit terraces should increase with distance from the pit centre. This would lead to a corresponding variation in pit morphology. For example, large oxygen concentrations towards the edge of each pit will inhibit the local evaporation rate, producing a pit with a slope which increases towards the edge. However, no substantial variations in pit morphology were observed and, in fact, when a slope variation did occur, the opposite trend was observed (Fig. 25).

In understanding adsorption phenomena during evaporation, the dynamical state of the surface must be taken into account. Assuming an evaporation coefficient, $\alpha_v = \frac{1}{3}$, the theoretical evaporation rate of zinc at 390°C is equivalent to the removal of 2.5×10^3 monolayers/sec. Therefore at 5×10^{-7} torr oxygen partial pressure, for every oxygen atom which can adsorb on the surface about 1.5×10^4 zinc atoms are leaving. If a dynamical adsorption equilibrium which maintains an equilibrium oxygen surface coverage for a given oxygen partial pressure in the gas phase is set up, a uniform evaporation pit morphology would be expected.

Simmons et al. (118), using L.E.E.D., observed a dynamical equilibrium concentration of adsorbed oxygen on copper of less than one monolayer, even after exposures equivalent to hundreds of monolayers. As oxygen is highly soluble in copper, they assumed that the excess oxygen had dissolved in the copper matrix. When the oxygen partial pressure in the system was increased, the equilibrium surface concentration increased. During evaporation, zinc atoms may "drag" some of the chemisorbed oxygen off the surface as they evaporate. If the fraction of oxygen atoms removed is proportional to the surface concentration of oxygen, an equilibrium surface population is established for a given flux of oxygen molecules to the surface, i.e. for a given partial pressure of oxygen in the vacuum system. The surface concentration of oxygen would then increase with increasing oxygen partial pressures. This is in agreement with the changes observed in the evaporation morphology as the partial pressure of oxygen was increased. De Maria et al. (119) have reported the existence of a critical temperature for the oxidation of a zinc surface during ion bombardment of the surface with inert gas ions.

This temperature seemed to represent an equilibrium condition between oxide growth and sputtering action. Similarly, the equilibrium suggested here is also one between induced desorption of oxygen from and adsorption of oxygen on the surface.

7.4.6 Summary of Evaporation Processes on Zinc Surfaces

A model for the vacuum evaporation of (0001) zinc surfaces is shown schematically in Fig. 53(a). The dashed line AA' represents a cleavage surface which is intersected by a "fresh" dislocation, D, and an impurity-decorated dislocation, D'. Monatomic evaporation steps are formed at D and D' by the mechanisms already discussed. The difference in pit depths is a consequence of the enhanced rate of step nucleation at decorated dislocations. The advance of these steps on the low index surface is retarded by impurities which diffuse to the surface from the bulk. Eventually, the impurity induced instability of monatomic steps caused them to bunch, producing a train of macroscopic ledges. The formation of stable macroledges further reduces the lateral ledge velocity and consequently an optically observable etch pit is produced. The pit slopes in Fig. 53(a) are exaggerated for clarity.

As the ledge kinetics at each type of pit should not differ, the diameters of the intersections of each pit with the cleavage surface, AA', should be equal (85). However, it was shown in Section 7.2.8 that, at the high undersaturation used in this investigation, two dimensional nulceation, T, on the perfect basal surface should proceed at a rapid rate. As a result, the surface AA' recedes, during evaporation to a position BB' and the pit diameters then reflect the difference in pit slope at D and D' as shown in Fig. 53(a). This may explain why shallow pits were observed to be smaller than deep pits when the partial pressures of oxygen were low (Fig. 16(a)). At higher oxygen partial pressures, all pits were observed to have larger diameters and both types of pits were more uniform in size (Fig. 24), indicating that adsorbed oxygen had retarded the rate of two dimensional nucleation on the perfect surface. Fig. 53(a) also shows how surface evaporation accentuates the different evaporation rates at different defects. When surface evaporation is retarded (Fig. 24) the depth difference is less evident. Similar effects have been reported by Ives and Plewes (63) who observed that the rate of general surface dissolution of (001) LiF cleavage surfaces in dilute aqueous solutions of ferric chloride is greatly reduced when the ferric ion concentration is increased to only 1 - 2 ppm.

When surfaces vicinal to the basal orientation are considered, the evaporation model (Fig. 53(b)) is only slightly modified. In this case, evaporation of the general surface will be more rapid, as vicinal surfaces provide a ready source of steps (41), eliminating the necessity for step nucleation. As before, bulk impurities can diffuse to the surface and promote the formation of macroscopic ledges.

In Fig. 53(b) it is seen that the inclined surface causes the observed height difference between the opposite faces of pits on vicinal surfaces. As the point P at the front of each pit cannot be maintained; a flat terrace is produced (Fig. 34(a) and (b)). The increased evaporation rate of the general surface probably eliminates the possibility of observing shallow pits, S, on these surfaces, in agreement with observed pit densities which were approximately equal to the density of deep pits on flat regions of the same sample.

7.5 Evaporation Model for Faceted Surfaces

When the "risers" of macroscopic ledges which form during evaporation are singular surfaces and have heights equal to many atomic spacings, the nucleation and motion of steps on the riser must also be taken into consideration. It will be shown below that when this is done for the ledges which were observed in the evaporation pits, a mechanism for macrokink formation in these ledges at high surface impurity levels is forthcoming.

The cross-section of a zinc surface comprised (0001) and $(10\bar{1}1)$ facets is shown in Fig. 54(a). Evaporation then proceeds by the nucleation of disc-shaped holes on both the terrace and riser. This is illustrated in Fig. 54(b). The free energy change for formation of a two-dimensional nucleus is again given by

$$\Delta G = \frac{\pi R^2 h}{\Omega} \Delta\mu_o + 2\pi Rh\gamma \qquad (7.20)$$

where R and h are the radius and depth of the nucleus respectively and $\Delta\mu_o$ is the change in chemical potential as an atom of the crystal is removed from the surface into the vapor phase. The free energy change for the nuclei shown in Fig. 54(b) is approximately half this value. It was shown in Section 3.5.1 that maximizing the above expression for ΔG with respect to R gives the free energy change for the formation of a critical nucleus as

$$\Delta G_p = \pi \gamma^2 \Omega h/\Delta\mu_o$$

$\Delta\mu_o = kT \ln p/p_e$ and is normally assumed to be independent of orientation.

However, as the radius of the critical nucleus is of the order of the lattice constant when $p/p_e \sim 10^{-4}$, a condition which holds in the present application, the use of macroscopic thermodynamics in treating nucleation phenomena is no longer accurate. For example, employing the bulk value for the surface energy in computing the free energies of small clusters is questionable because the definition of this quantity is ambiguous for small groups of atoms (120). Also, when small nuclei are involved, the free energy change on forming a critical nucleus should be a sensitive function of the coordination number of the atoms, i.e. on the surface orientation. It is a reasonable assumption that nucleation is most difficult on the plane where the atoms are most tightly bound. For zinc, this is the (0001) surface in which each atom has 9 nearest neighbours. The next most stable plane is the $(10\bar{1}1)$ plane which is the probable orientation of the macroscopic ledges (Section 7.4.4). Atoms in alternate $(10\bar{1}1)$ planes have 8 and 6 nearest neighbours. The plane with 8 nearest neighbours will obviously have the slowest nucleation rate. Therefore, nucleation on this plane will be compared with that on (0001) planes.

If nuclei are formed by atoms leaving positions in the close packed terrace and diffusing to adatom sites, the number of nearest neighbour bonds broken on (0001) and $(10\bar{1}1)$ planes for this step are 6 and 5 respectively. Although surface diffusion of adatoms may also have some effect on nucleation, a bond model analysis of the formation of small nuclei suggests that nucleation on non-basal surfaces is more rapid than on basal surfaces.

Based on this assumption, it is proposed that evaporation of the faceted surface shown in Fig. 54(a) takes place primarily by the nucleation and advance of steps on the $(10\bar{1}1)$ ledge risers. The nucleation and motion of steps on the (0001) terrace also takes place but at a slower rate.

When the height of the macroledge is much smaller than its length, as is the case here, step motion on the riser is primarily along its length, i.e. in $<11\bar{2}0>$ directions for $(10\bar{1}1)$ risers. Steps nucleated on the riser move away from their point of nucleation (Fig. 55(a)) towards the intersection of neighbouring ledges where they are annihilated by similar steps on the risers of these ledges. Steps nucleated on different parts of the same riser (Fig. 55(b)) may also interact and annihilate (Fig. 55(c)). Consequently, most steps travel insufficient distances on the $(10\bar{1}1)$ riser to be affected by impurities when the concentration of the latter is small. Only those steps which nucleate close to the centre of a reasonably long riser and are able to travel to the corner without annihilation can possibly accumulate enough impurity atoms at the step to be effectively retarded. However, on the riser of a long ledge it is unlikely that a step could travel the necessary distance without annihilation. Therefore, at low surface impurity concentrations, the straight macroledges which were observed would be expected.

When the surface impurity concentration is larger, steps nucleated at the centre collect impurities more rapidly and are effectively retarded after much shorter distances. Steps nucleated between the centre of the riser and the poisoned step (this is possible because the "back-stress" effect (Section 3.7) is reduced close to the poisoned step (62)) pile-up into the latter and a macrokink forms.

For a given impurity level, a ledge close to the pit centre is too short for this mechanism to be effective (Fig. 56(a)). As the ledge moves away from the pit centre, a point is reached when its length is just sufficient for a macrokink to form (Fig. 56(b)). As the ledge moves further from the pit centre, a second kink forms in a similar manner. As the length of the ledge increases further, more macrokinks form and a macrokink pile-up at the pit corners results (Fig. 56(c) and (d)). The resemblence between Fig. 56(d) and the ledge structure in Fig. 18(b) indicates that this mechanism is responsible for the ledge structures observed at high surface impurity concentrations.

It follows from the above discussion that for a given surface impurity population, a critical riser length, L_c, (Fig. 56(b)) is required before macrokink formation is possible. Therefore, on a given pit face, there should be a region approximately equal to L_c which is relatively free of macrokinks. This explains the observed parallel boundaries between the macrokink pile-ups and straight $<11\bar{2}0>$ ledges shown in Fig. 20(b).

As the surface impurity concentration is increased, the unkinked length, L_c, should decrease since the distance a step must move before it is retarded to produce a macrokink decreases with increasing impurity concentration. The trend shown in Figs. 16(b), 17(b) and 20(b) as the oxygen partial pressure is increased is in full agreement with this prediction. The agreement between the model shown in Fig. 54 for evaporation of a faceted surface and experimental observations, is strong support for its validity.

Steps which are nucleated on a (0001) terrace advance across the terrace and are incorporated into the preceding macroledge, giving a steady-state surface morphology. Their motion is, of course, inhibited by impurities present on the terrace. If there is a fluctuation in the surface impurity concentration or in the macroledge spacing, further bunching may occur between the ledges. This would cause the uneven separation of ledges shown in Fig. 14(b).

7.6 Evaporation at Very High Oxygen Pressures

The evaporation morphologies which were observed at high oxygen partial pressures were extremely complex. An explanation of their development is attempted below. However, it should be stated that it is at best speculative.

Since the d-electron levels in zinc are filled, the zinc-oxygen bond in the two-dimensional surface matrix is weak relative to the bond between a transition metal and oxygen. Consequently, the zinc-oxygen adsorption state is unstable with respect to zinc oxide nucleation at oxygen levels of approximately one monolayer (107). Therefore, as the oxygen partial pressure is increased, a critical value is attained at which oxide nucleation occurs on the surface.

Large evaporation features (e.g. hillocks), indicative of the presence of zinc oxide nuclei on the surface were observed at an oxygen partial pressure of 1.1×10^{-6} torr. However, nucleation almost certainly commenced at a lower partial pressure. If a large number of small oxide nuclei are formed on the surface, macroledges interact with these nuclei as they advance on the surface. If the nuclei are randomly distributed, the directional probability of ledge motion is now isotropic and the ledge becomes round. At points where it is retarded by the nuclei, it develops a mottled structure. The evaporation features shown in Fig. 21(c) and (d) can be rationalized by this mechanism. Local inhibition of general surface evaporation produces the observed "dimpled" structure (Fig. 21(c))).

At higher oxygen partial pressures, the oxide nuclei grow and a thin oxide film (a few angstroms thick) covers the surface. Evaporation then takes place by the local breakdown of this film. Step motion on the surface is completely stopped and consequently the pit sides become very rough (Fig. 22(b)). The nucleation and motion of steps at pit-bottoms is also poisoned and the pits become shallow-bottomed (Fig. 22(c)). (It should be remembered that these pits had already been initiated and well developed before the oxygen was introduced to the vacuum system.) Large oxide nuclei on the general surface can completely stop evaporation from that region and a hillock develops (Fig. 22(d)).

A more exact explanation of these morphologies requires a knowledge of the detailed surface structure. The limited resolution of the scanning electron microscope prevented the observation of these details in the present study.

7.7 Evaporation of Pre-Cleaved Surfaces

A thin (∿ 20Å) oxide film is quickly formed when a freshly cleaved zinc surface is exposed to the atmosphere. During a subsequent evaporation run, the oxide film must break down if evaporation of the metal is to occur. Breakdown of the film initially takes place at defects both in the film and the metal, e.g. cleavage steps, emergent dislocations. At higher temperatures, breakdown of the film is general, except at isolated sites, where unevaporated islands develop. (Fig. 26).

An appreciable fraction of the oxygen atoms which were present in the oxide film obviously remain adsorbed on the surface where they influence the evaporation morphology. In particular, the rough ledge morphology (Fig. 27(b)) on a pre-cleaved sample is a consequence of the large amount of oxygen remaining on the surface, i.e. oxygen is the impurity which causes the macro-kinking discussed earlier. It was also observed that the ledge heights were lower on pre-cleaved surfaces than on vacuum cleaved surfaces which had been evaporated under the same experimental conditions (Table 8). Assuming that the macroscopic ledges had developed by the mechanism described in Section 7.4.3, the magnitude of the ledge height indicates that the surface oxygen concentration was equivalent to that when an oxygen partial pressure of $> 10^{-7}$ was present during evaporation of vacuum-cleaved surfaces.

7.9 Evaporation Ledge Structure at Twins

Fig. 57(a) shows the cross-section of a $(10\bar{1}2)$ deformation twin BCD and its associated accommodation kink ABC (90). Dashed lines are drawn to show the relative orientations of (0001) planes in the twinned, kinked and perfect regions of the crystal.

It can be seen in Fig. 57(a) that the the surface plane, CD, of the twin equivalent to a high index orientation. Therefore, it provides a ready source of monatomic steps during evaporation. In the normal manner, step bunching produces macroscopic ledges (Fig. 57(b)).

As the $(10\bar{1}2)$ twinning plane intersects the basal plane along a $<11\bar{2}0>$ direction, macroscopic ledges parallel to this direction would be expected to develop during evaporation. This is in agreement with the observed ledge structure (Fig. 37(a)).

From Fig. 57(a) it can be seen that the risers were probably (0001) surfaces. The scanning electron micrographs (e.g. Fig. 37(b)) indicate that the terraces separating these ledges were also planar. Initially, it was thought that these ledges were $(10\bar{1}1)$ surfaces as this is the most stable plane after the 0001 plane, in the h.c.p. system (Section 7.4.4). It can be shown by simple geometry that, in order that the evaporated twin surface C'D' (Fig. 57(b)) be composed of (0001) and $(10\bar{1}1)$ surfaces, it would have to make an angle of at least 21° with the perfect basal surface. However, the unevaporated twin surface, CD, causes a change of slope of only 3° 58' on the basal surface (123). Therefore, a large variation in evaporation rate across the twin surface is necessary to produce a surface slope which can facilitate the development of (0001) ledges separated by $(10\bar{1}1)$ terraces. As such a variation is improbable, the terraces must be some other low index surface, e.g. $(10\bar{1}0)$ surfaces. As $(10\bar{1}0)$ planes are perpendicular to (0001) planes, $(10\bar{1}0)$ terraces on the evaporated twin would be approximately parallel (within 4°) to the orientation of the basal surface on untwinned regions of the surface, (Fig. 57(b)). Scanning electron microscopic observations of the ledge structure were indicative that this was, in fact, true.

7.10 Relation to Other Experiments

The previous studies of thermal evaporation of zinc by Ruff (40) and Rais and Bromberg (39) resulted in observations of evaporation pits. However, these experiments were performed with surfaces which had previously been exposed to air. Consequently a thin oxide film, which must be punctured before evaporation can commence, was present on these surfaces. The observations in the present study show that the evaporation morphology on a vacuum-cleaved surface is different from that on an air-cleaved surface. The rough ledge structure observed by Ruff (40) could only be reproduced when an oxide film was initially present on the surface or when evaporation was carried out in high oxygen partial pressures.

It was shown in this thesis that the breakdown of an oxide film during evaporation leaves behind a surface with an appreciable concentration of adsorbed oxygen. Therefore, Ruff's (40) use of evaporation theories which describe monatomic step motion on clean surfaces to interpret the observed evaporation morphology is unrealistic. Also, these surfaces are not conducive to the study of impurity effects on the evaporation morphology. Many important effects may be masked by the initial presence of oxygen on the surface. For example, Ruff (40) did not observe any change in evaporation morphology when samples of different purity were employed, whereas the present results show that the morphology is definitely affected by changes in sample purity. It must be concluded therefore, that if a quantitative investigation of the evaporation phenomenon is to be successful, a prime condition is that the surface be prepared in vacuum.

Several workers have reported that thermal pits could only be observed at low or intermediate undersaturations. For example, Ejima et al. (21) observed evaporation pits to form only at edge dislocations when a slight (unspecified) undersaturation was imposed. For very small or very large undersaturations, no preferential evaporation was observed. The presence of impurities (due to surface polishing) was also required. Young and Gwathmey (28) also reported that small undersaturations were necessary to produce observable pits. They observed pronounced evaporation pitting close to the low index poles of electropolished spheres of impure copper. The observations on zinc disagree with these results to the extent that, although the samples were evaporated at large undersaturations, evaporation pits were produced on the zinc surfaces. It is, however, in agreement with the observations of Ejima et al., that the presence of surface impurities is necessary to produce detectable etch pits.

Bolgov et al. (29) observed that evaporation pitting in nickel was promoted by the addition of boron (< 1%) to the crystals. They suggested that the precipitation of boron at dislocations had increased the local chemical potential in these regions, leading to a local enhancement of the evaporation rate. It has been shown in this thesis, however, that when this takes place, the vapor pressure is normally expected to decrease. Therefore, unless the precipitate is rich in boron and the vapor pressure of boron is much greater than that of nickel, a decrease in the local evaporation rate would be expected. In fact, the vapor pressure of nickel is greater than that of boron. On the other hand, if a nickel-rich phase had precipitated at dislocations, it is possible that the mechanism proposed here to account for impurity enhanced evaporation at dislocations is applicable to Bulgov et al.'s system, i.e. thermal grooving at the phase boundaries produces a high surface curvature at the precipitation leading to an enhanced evaporation rate.

In Chapter 2, the disagreement regarding the mechanism by which macroscopic ledges are formed during thermal etching was pointed out. The observations reported here were interpreted in terms of the dynamic bunching of monatomic steps due to impurity poisoning. This agrees with Moore's (37) point of view that the development of macroledges on an evaporating surface is a kinetic effect and not the result of minimization of the surface free energy.

The present work is the first investigation of evaporation from an initially clean metal surface. Consequently, the systematic investigation of the effect of gaseous and bulk impurities on the evaporation morphology is more meaningful than any other attempts which have hitherto been attempted. The only comparable investigations of impurity effects on the "etching" phenmenon have been carried out in the related field of chemical dissolution. Gilman et al. (18) found that the dissolution of (001) LiF cleavage surfaces in distilled water only produces observable etch pits in the presence of small amounts of an ionic species which adsorb at advancing dissolution steps and "poison" the dissolution process. Ferric ions in the etching solution serve this function for the dissolution of LiF. Similarly in the present work it has been proposed that bulk impurities which diffuse to the surface poison evaporation steps, leading to the formation of optically observable evaporation pits.

The effect on the ledge structure of various partial pressures of oxygen in the vacuum system can be compared to the work of Ramachandran and Ives (27), who studied the dissolution of LiF in dilute aqueous solutions of ferric chloride when the ferric ion concentration was varied. They found a decrease in the ledge height and ledge spacing as the ferric ion concentration was increased from < 1 ppm to 150 ppm, although the ledges were unresolvable above a few ppm. They believed that at low ferric ion concentrations, only isolated steps were impeded because of an uneven surface impurity coverage. Then, as the intermediate steps pile up against the poisoned steps, a small number of large ledges were produced. At higher inhibitor contents, a more uniform surface impurity coverage was achieved, producing smaller ledge heights and ledge spacings. On zinc surfaces, the ledge heights and ledge spacings were also observed to decrease as the oxygen partial pressure was increased. Here, however, the surface impurity concentrations are believed to have been too high for the mechanism proposed by Ramachandran and Ives to be applicable. Therefore, a mechanism, which assumed an equilibrium surface impurity population and considered the time required to produce a uniform coverage of the steps by impurities as controlling the ledge height and ledge spacing .has been proposed to explain these observations. If one assumes that during dissolution of LiF in dilute aqueous ferric chloride solutions, an equilibrium ferric ion concentration is maintained on the surface, this mechanism could also be used to interpret the observations of Ramachandran and Ives.

These authors also observed that the etch pits became round at high ferric ion concentrations. "Rounding" effects due to a pile-up of macrokinks at pit corners were also observed on the zinc surfaces of this work at high (> 10^{-7} torr) oxygen partial pressures. The formation and pile-up of macrokinks has been shown to result from impurity-induced bunching of steps advancing on the plane of the macroledge. However, the electron micrographs of Ramachandran and Ives show that the macroledges on LiF surfaces were not low index planes (they had an extremely rough structure) and this explanation cannot apply to their observations.

CHAPTER 8

CONCLUSIONS

1. Clean (0001) zinc surfaces were prepared by cleaving in ultra-high vacuum (5 x 10^{-10} torr). These surfaces, when heated to 390°C in vacuum (5 x 10^{-8} torr), developed optically observable evaporation pits at emergent dislocations. The average pit density was 4 x 10^{4} cm^{-2}.

2. A fraction of the pits (< 10% total density) were observed to have depths significantly larger than the average. The density of deep pits increased when the impurity content of the crystals was increased. It was shown indirectly that, in alcoholic hydrochloric acid solutions, enhanced chemical attack at the same defect sites produced "steep-sided" (slope ∿ 5°) pits. These observations were indicative that the defects associated with the chemical and evaporation pits were impurity-decorated dislocations. It is believed that, at elevated temperature, changes in the surface curvature at decorated dislocations produce an enhancement of the local evaporation rate, as a consequence of the Gibbs-Thompson effect.

3. The evaporation pit faces were composed of (0001) terraces separated by ledges of multiatomic height. An increase in the surface impurity population produced a decrease in the height and spacing of the ledges. A model which describes the bunching of monatomic steps to form a macroscopic ledge was proposed.

4. Impurity sources which were operative during evaporation have been considered in detail. At pressures $< 10^{-7}$ torr, impurities which out-diffuse from the bulk are believed to be most important. At higher pressures, impurities which are adsorbed from the gas phase become increasingly important. Bulk impurities and gaseous impurities which are strongly adsorbed on the surface have similar effects on the evaporation morphology.

5. At high oxygen partial pressures ($> 10^{-7}$ torr), macrokinks formed on macroscopic ledges. They were observed to "pile-up" at pit corners. As the partial pressure of oxygen was increased, this macrokink "pile-up" intensified producing "rounding" of the pits. When the oxygen partial pressure was raised beyond 8×10^{-7} torr, the formation of ZnO nuclei on the surface produced an extremely irregular ledge morphology.

6. A model for the evaporation of faceted surfaces was proposed. It was then employed to interpret the experimental observations at high oxygen partial pressures.

7. The evaporation morphology on pre-cleaved (0001) zinc surfaces was compared with that on vacuum cleaved surfaces. The rough ledge structure on precleaved surfaces was indicative of an appreciable concentration of oxygen on the surface.

CHAPTER 9

SUGGESTIONS FOR FURTHER WORK

The observations reported in this thesis suggest a number of directions which future studies of evaporation might pursue. In general, they involve quantitative investigations of impurity effects which were demonstrated qualitatively in the present work.

(a) The introduction of various amountsof known impurities, e.g. Fe, would help determine the exact role they play in the nucleation and motion of steps on an evaporating surface. In order that a study of this nature be successful, background impurity effects must be minimized. The present observations indicate that the level of impurities in very high purity zinc is sufficient to effectively influence the development of the evaporation morphology. Therefore, zinc which is employed to grow impurity-doped crystals must be extremely pure. This could only be obtained by carefully zone refining high-purity zinc. In order that the adsorption of reactive gases on the evaporating surface does not interfere with bulk impurity effects, a refinement of the experimental technique is required so that pressures $\leq 10^{-9}$ torr can be maintained during evaporation.

(b) An improvement in the experimental technique would also permit more exact studies of gaseous impurity effects. Gases, other than oxygen, may be employed in these studies. However, the complexities caused by the gases reacting with hot filaments must be eliminated. For example, other heating methods, such as the use of a laser, might be employed.

(c) Information with respect to the concentration of surface impurities during evaporation would, perhaps, allow a more quantitative understanding of impurity effects on ledge motion. It would also provide information regarding a possible oxygen adsorption equilibrium on an evaporating zinc surface.

(d) A knowledge of the instantaneous evaporation coefficient, α_v, for evaporation from a contaminated surface would provide valuable information which, when combined with the observed surface morphology, could lead to a further clarification of the evaporation mechanism. However, this would demand an exact knowledge and strict control of the surface temperature. Earlier discussion in this thesis indicated that this may be very difficult to achieve.

REFERENCES

1. S. Dushman, "Scientific Foundations of Vacuum Technique" (J. Wiley and Sons, New York, 1962) 2nd ed. p. 673.
2. H. Hertz, Ann. Phys. (Leipzig) 17, 177 (1882).
3. M. Knudsen, Ann. Phys. (Leipzig) 47, 697 (1915).
4. I. Langmuir, J. Am. Chem. Soc. 35, 931 (1913).
5. O. Knacke and I. N. Stranski, Progr. in Metal Phys. 6, 181 (1956).
6. B. Paul, A.R.S. Journal 32, 1321 (1962).
7. J. P. Hirth and G. M. Pound, "Progress in Materials Science 11, 1 (1963).
8. W. Rosenhain and D. Ewan, J. Inst. Met. 8, 149 (1912).
9. C. F. Elam, Trans. Faraday Soc. 32, 1406 (1936).
10. B. Chalmers, R. King and R. Shuttleworth, Proc. Roy. Soc. A193, 465 (1948).
11. A. J. W. Moore, Acta Met. 6, 293 (1958).
12. R. M. Lowe,Acta Met. 12, 1111 (1964).
13. F. C. Frank, Disc. Faraday Soc. 5, 48, 67 (1949).
14. W. Shockley and W. T. Read, Phys. Rev. 75, 692 (1949).
15. P. Lacombe and L. Beaujard, J. Inst. Metals. 74, 1 (1948).
16. W. G. Johnston, Prog. Ceramic Sci. 2, 1 (1962); W. H. Robinson, in "Techniques in Metals Research", ed. R. F. Bunshah (J. Wiley and Sons, New York, 1968) p. 291.
17. N. Cabrera, J. Chim.Phys. 53, 675 (1956).
18. J. J. Gilman, W. G. Johnston and G. W. Sears, J. Appl. Phys. 29, 747 (1958).

19. W. L. Winterbottom and J. P. Hirth, "Condensation and Evaporation of Solids", (Gordon and Breach, New York (1961)) p. 347.

20. G. J. Russell and D. Haneman, J. Electrochem. Soc. 114, 398 (1967).

21. T. Ejima, W. H. Robinson and J. P. Hirth , J. Cryst. Growth (to be published).

22. G. A. Bassett, Phil. Mag. 3, 1042 (1958).

23. K. W. Keller, "Crystal Growth" (ed. H. S. Peiser (Pergamon Press, Oxford 1967)) p. 629.

24. E. Votava and A. Berghezan, Acta Met. 7, 392 (1959).

25. E. N. da C. Andrade and R. F. Y. Randall, Proc. Phys. Soc. B63, 198 (1950).

26. I. N. Stranski, R. Laischew and L. Krastanov, Zeit. Krist. 88, 326 (1934).

27. T. R. Ramachandran and M. B. Ives, J. Appl. Phys. 38, 3675 (1967).

28. F. W. Young, Jr. and A. T. Gwathmey, J. Appl. Phys. 31, 225 (1960).

29. I. S. Bulgov, V. M. Azhazha, V. M. Amonenko and M. P. Zeydlits. Phys. Metals Metallography. 18, No. 4, 74 (1964).

30. A. H. Cottrell, "Dislocations and Plastic Flow in Crystals", (Oxford Univ. Press. 1953) p.134.

31. D. A. Vermilyea, Acta Met. 6, 381 (1958).

32. J. J. Gilman, Trans. Met. Soc. AIME 206, 998 (1956).

33. R. Shuttleworth, Metallurgia 38, 125 (1948).

34. E. D. Hondros and A. J. W. Moore, Acta Met. 8, 647 (1960).

35. F. C. Frank, "Growth and Perfection of Crystals", ed. R. H. Doremus, B. W. Roberts and D. Turnbull (J. Wiley and Sons, New York 1958) p. 411.

36. G. E. Rhead and H. Mykura, Acta Met. 10, 578 (1962).

37. A. J. W. Moore, "Metal Surface" (ASM 1963) p. 155.

38. J. C. Danko and A. J. Griest, Trans Met. Soc. AIME 206, 515 (1956).

39. G. B. Rais and M. I. Bromberg, Soviet-Phys. Cryst 4, 555 (1960).

40. A. W. Ruff, Jr., J. Chem. Phys. 41, 1204 (1964).

41. J. P. Hirth and G. M. Pound, J. Chem. Phys. 26, 1216 (1957).

42. J. P. Hirth and G. M. Pound, Acta Met. 5, 649 (1957).

43. N. Cabrera and M. M. Levine, Phil. Mag. 1, 450 (1956).

44. J. W. Gibbs, "The Scientific Papers of J. W. Gibbs" (Dover Publications, 1961).

45. W. W. Mullins, "Metals Surfaces" (ASM, 1963) p. 17.

46. W. A. Miller, G. J. C. Carpenter and G. A. Chadwick. Phil Mag. 19, 305 (1969).

47. C. J. Smithells, "Metals Reference Book" 3rd ed., vol. 1 (Butterworths, London 1962) p. 202.

48. F. C. Frank, "Growth and Perfection of Crystals" ed. R. H. Doremus, B. W. Roberts and D. Turnbull (J.Wiley and Sons, New York 1958) p. 3.

49. N. A. Gjostein, Acta Met. 11, 957 (1963).

50. R. Sundquist, Acta Met. 12, 67 (1964).

51. C. Herring, Phys. Rev. 82, 87 (1951).

52. N. A. Gjostein, Acta Met. 11, 969 (1963).

53. E. Gruber (unpublished research).

54. W. Kossel, Nachr. Geo. Wiss. Gottingen 135 (1927).

55. I. N. Stranski, Z. Phys. Chem. 136, 259 (1928).

56. W. K. Burton, N. Cabrera and F. C. Frank, Trans Roy. Soc. A243, 299 (1950).

57. M. Volmer, Kinetic der Phasenbildung. Steinkopff Dresden und Leipzig (1939).

58. J. W. Cahn, Acta Met. 8, 554 (1960).

59. W. T. Read, "Dislocations in Crystals" (McGraw-Hill, N. Y. 1953).

60. J. M. Burgers, Proc. Kon. Ned. Akad. Wetenschap 42, 293 (1939).

61. J. B. Hudson and G. W. Sears, J. Chem. Phys. 35, 1509 (1961).

62. N. Cabrera, "The Surface Chemistry of Metals and Semi-conductors", edited by J. J. Gilman. (John Wiley and Sons, N. Y. 1960) p. 171.

63. M. B. Ives and J. T. Plewes, J. Chem. Phys. 42, 293 (1965).

64. N. Cabrera and D. A. Vermilyea, "Growth and Perfections of Crystals", ed. R. H. Doremus, B. W. Roberts and D. Turnbull, J. Wiley and Sons, N. Y. (1958) p. 393.

65. G. W. Sears, "Growth and Perfections of Crystals", ed. R. H. Doremus, B. W. Roberts and D. Turnbull, J. Wiley and Sons, New York (1958) p. 441.

66. M. B. Ives and J. P. Hirth, J. Chem. Phys. 33, 517 (1960).

67. O. Kubaschewski, E. LL. Evans and C. B. Alcock, "Metallurgical Thermochemistry" with ed. 4th edition (Pergamon Press, Oxford, 1967).

68. R. W. Swalin, "Thermodynamics of Solids (J. Wiley and Sons, Inc. 1962).

69. W. Thompson, Phil. Mag. 42, 448 (1871).

70. C. Herring, "The Physics of Powder Metallurgy" ed. W. E. Kingston (McGraw-Hill, New York 1951) p. 143.

71. A. H. Cottrell and B. A. Bilby, Proc. Phys. Soc. A. 62, 49 (1949).

72. B. A. Bilby, Proc. Phys. Soc. A. 63, 191 (1950).

73. H. L. Wain and A. H. Cottrell, Proc. Phys. Soc. B. 63, 339 (1950).

74. A. H. Cottrell, "Report on Strength of Solids", (London Phys. Soc. p. 30 (1948).

75. J. R. Bailey, Supp. Al. Nouvo Cimento 1, 494 (1963).

76. L. E. Prescott, Rev. Sci. Instr. 33, 485 (1962).

77. M. Hansen, "Constitution of Binary Alloys", Second edition (McGraw-Hill Book Co., New York 1958).

78. R. P. Elliot, "Constitution of Binary Alloys" - First Supplement. (McGraw-Hill, New York 1965).

79. H. S. Rosenbaum and M. M. Saffren, J. Appl. Phys. 32, 1866 (1961).

80. J. Lozano, Anales de Fisica Y Quimica 61, 1965 (1964).

81. J. Blears, J. Sci. Instruments 28, S1, 36, (1951).

82. J. J. Gilman, Trans Met. Soc. AIME 203, 1252 (1955).

83. B. Chalmers, "Physical Metallurgy" (J. Wiley and Sons, 1959) p. 341.

84. S. Amelinckx, Phil. Mag. 1, 269 (1956).

85. M. B. Ives and D. D. McAusland, Surface Sci. 12, 189 (1968).

86. J. M. Schultz and R. W. Armstrong, "Direct Observations of Dislocations in Crystals" (Interscience Publishers, N. Y. 1962) p. 569.

87. H. Suzuki, J. Phys. Soc. Jap. 10, 981 (1955).

88. J. J. Gilman, Trans. Met. Soc. AIME 212, 310 (1958).

89. P. G. Partridge, Metallurgical Reviews 12, 169 (1967).

90. D. C. Jillson, Trans Met. Soc. AIME 188, 1009 (1952).

91. P. L. Pratt and S. F. Pugh, J. Inst. Met. 80, 653 (1952).

92. H. S. Rosenbaum, Acta Met. 9, 742 (1961).

93. A. J. Forty and F. C. Frank, J. Phys. Soc. Jap. 10, 656 (1955).

94. W. C. Dash, J. Appl. Phys. 27, 1193 (1956).

95. F. W. Young, Jr., Acta Met. 29, 760 (1958).

96. J. B. Newkirk, "Precipitation from Solid Solution" (ASM 1959) p. 46.

97. J. W. Christian, "The Theory of Transformations in Metals and Alloys" (Pergamon Press, Oxford 1965) p. 634.

98. A. R. Patel and R. P. Singh, J. Phys. D. 2, 319 (1969).

99. R. E. Honig, R.C.A. Review 23, 567 (1962).

100. A. P. Batra, Phys. Rev. 159, 487 (1961).

101. C. Kittel, "Introduction to Solid State Physics", 3rd edition. (J. Wileyand Sons Inc., New York 1966).

102. I. M. Lifshits and A. A. Chernov, Soviety Physics-Crystallography 4, 746 (1960).

103. J. J. Gilman, J. Appl. Phys. 31, 936 (1960).

104. R. L. Schoebel, J. Appl. Phys. 37, 3682 (1966).

105. M. Straumanis, Z. Phys. Chem. B13, 316 (1931).

106. B. M. W. Trapnell, Proc. Roy. Soc. 218A, 566 (1953).

107. H. H. Uhlig, Corrosion Science 7, 325 (1967).

108. T. N. Rhodin, J. Phys. Chem. 57, 143 (1953).

109. E. H. Kennard, "Kinetic Theory of Gases" (McGraw-Hill, N. Y. 1938).

110. J. T. Hurd and R. O. Adams, J. Vac. Sci. Tech. 6, 229 (1969).

111. F. Jona, J. Phys. Chem. Sol. 28, 2155 (1967).

112. L. A. Harris, J. Appl. Phys. 39, 1419 (1968).

113. J. E. Boggio and H. E. Farnsworth, Surface Science 1, 399 (1964).

114. H. E. Farnsworth, C. A. Haque, D. M. Zehner and C. Barton, Surface Science 17, 1 (1969).

115. J. J. Burton, Phys. Rev. 177, 1346 (1969).

116. M. A. H. Lanyon and B. M. W. Trapnell, Proc. Roy. Soc. A 227, 387 (1955).

117. C. J. Smithells, "Metals Reference Book", 3rd edition, vol. 2, (Butterworths, London 1962, p. 570.)

118. G. W. Simmons, D. F. Mitchell and K. R. Lawless, Surface Science 8, 130 (1967).

119. R. De Maria, P. Spinedi and E. Susi-de Maria, Corrosion 24, 237 (1968).

120. J. G. Kirkwood and F. P. Buff, J. Chem. Phys. 18, 991 (1950).

121. G. Ehrlich and F. G. Hudda, J. Chem. Phys. 44, 1039 (1966).

122. L. Onsager, Phys. Rev. 37, 405 (1931).

123. A. J. W. Moore, Acta Met. 3, 163 (1955).

TABLE 1

SOLUBILITIES OF PRINCIPAL IMPURITIES DETECTED IN ZINC CRYSTALS

Element	Solubility (77,78)	Comments
Fe	0.0009-0.0028 wt.% between 150-400°C	not very soluble
Si	eutectic at 0.04 at.% at 0.2°C below melting point of zinc	separates out below M.P. of zinc
Ni	0.03 at % at 400°C decreasing to 0.007 at.% at 100°C	relatively insoluble
Pb	possibly less than 6 x 10^{-4} wt.%	often failed to show any solubility
Sn	0.14 at. % at eutectic but separates out on coling	very restricted solubility
Al	Maximum of 2.6 at.% at 380°C 0.15 at % at room temperature	relatively soluble
Cu	Maximum of 2.77 at.% at 424°C 2.56 at % at 400°C 0.31 at % at 100°C	relatively soluble
Cd	retrograde curve with maximum of 1.5 at.% at 350°C.0.05 at 94°C	practically nil at room temperature
Mn	0.53 at. % at 417°C, decreasing with temperature to 0.02 wt% at 200°C	restricted solubility
Mg	0.45 at.% at 364°C, decreasing with temperature to 0.02 at.% at 200°C	restricted solubility

TABLE 2

RESIDUAL GAS ANALYSIS OF UNBAKED VACUUM SYSTEM

Mass (A.M.U./coul.)	Ionic Partial Pressure (x 10^9 torr.)	Probable Ion	Parent Molecule	Gas Partial Pressure (x 10^9 torr.)
2	80	H_2^+	H_2	70
15	3	CH_3^+	CH_4	-
16	6	CH_4^+	CH_4	9
17	15	OH^+	H_2O	-
18	50	H_2O^+	H_2O	65
20	6	Ne^+	Ne	6
28	12	CO^+	CO	12
32	1	O_2^+	O_2	1
35	<< 1	Cl^+	HCl	<< 1
44	2	CO_2^+	CO_2	2

Total Pressure = 1.2 x 10^{-7} torr.

TABLE 3

RESIDUAL GAS ANALYSIS OF ULTRA-HIGH VACUUM

Mass (A.M.U./coul.)	Ionic Partial Pressure ($\times 10^{11}$ torr)	Probable Ion	Parent Molecule	Gas Partial Pressure ($\times 10^{11}$ torr)
2	50	H_2^+	H_2	45
12	1	C^+	CH_4	-
14	2	CH_2^+	CH_4	-
15	4	CH_3^+	CH_4	-
16	4	CH_4^+	CH_4	11
17	3	OH^+	H_2O	-
18	10	H_2O^+	H_2O	13
20	1	Ne^+	Ne	1
28	27	CO^+	CO	27
32	1	O_2^+	O_2	1
35	5	$C\ell^+$	$HC\ell$	-
36	4	$HC\ell^+$	$HC\ell$	9
44	4	CO_2^+	CO_2	4

Total Pressure = 6.2×10^{-10} torr.

TABLE 4

RESIDUAL GAS ANALYSIS DURING ELECTRON BOMBARDMENT

Mass (A.M.U./coul.)	Ionic Partial Pressure ($\times 10^9$ torr)	Probable Ion	Parent Molecule	Gas Partial Pressure ($\times 10^9$ torr)
2	200	H_2^+	H_2	190
12	3	C^+	CH_4	-
15	5	CH_3^+	CH_4	-
16	8	CH_4^+	CH_4	16
18	2	H_2O^+	H_2O	2
20	9	Ne^+	Ne	9
28	40	CO^+	CO	40
32	$<< 1$	O_2^+	O_2	$<< 1$
35	< 1	$C\ell^+$	$HC\ell$	< 1
44	16	CO_2^+	CO_2	16

Total Pressure = 2×10^{-7} torr.

TABLE 5

RESIDUAL GAS ANALYSIS DURING EVAPORATION

Mass (A.M.U./coul.)	Ionic Partial Pressure (x 10^9 torr)	Probable Ion	Parent Molecule	Gas Partial Pressure (x 10^9 torr)
2	30	H_2^+	H_2	30
12	2	C^+	CH_4	-
16	2	CH_4^+	CH_4	4
18	6	H_2O^+	H_2O	6
20	6	Ne^+	Ne	6
28	11	CO^+	CO	11
32	< 1	O_2^+	O_2	< 1
35	2	$C\ell^+$	$HC\ell$	-
36	1	$HC\ell^+$	$HC\ell$	3
44	3	CO_2^+	CO_2	3

Total Pressure = 4 x 10^{-8} torr.

TABLE 6

RESIDUAL GAS ANALYSIS DURING OXYGEN-LEAK EXPERIMENTS

Mass (A.M.U./coul.)	Ionic Partial Pressure (x 10^8 torr)	Probable Ion	Parent Molecule	Gas Partial Pressure (x 10^8 torr)
2	7	H_2^+	H_2	7
16	6	O_2^{++}	O_2	-
18	3	H_2O^+	H_2O	3
28	7	CO^+	CO	7
32	70	O_2^+	O_2	76
44	1	CO_2^+	CO	1

Total Pressure = 7.5×10^{-7} torr.

TABLE 7

RESIDUAL GAS ANALYSIS DURING CARBON DIOXIDE-LEAK EXPERIMENTS

Mass (A.M.U./coul.)	Ionic Partial Pressure (x 10^8 torr)	Probable Ion	Parent Molecule	Gas Partial Pressure (x 10^8 torr)
2	8	H_2^+	H_2	8
12	4	C^+	C	4
15	0	CH_3^+	CH_4	0
16	8	O^+	atomic oxygen	8
18	< 1	H_2O^+	H_2O	< 1
20	6	Ne^+	Ne	6
22	2	CO_2^{++}	CO_2	-
28	15	CO^+	CO	15
32	< 1	O_2^+	O_2	< 1
44	40	CO_2^+	CO_2	42

Total Pressure = 6×10^{-7} torr.

TABLE 8

EFFECT OF OXYGEN ON EVAPORATION MORPHOLOGY

Sample Number	Experimental Conditions	Pit Density ($\times 10^4$ cm^{-2})	Observations
1	vacuum 4×10^{-8} torr	2	point-bottomed pits with ledges along <11$\bar{2}$0> directions. Very few macrokinks. Ledge height ∿1400Å. Ledge separation ∿2.0μm
9	vacuum 5×10^{-8} torr	8	same as above
2	pre-cleaved surface vacuum 5×10^{-8} torr	6	shallow, point-bottomed pits with a very irregular <11$\bar{2}$0> ledge structure. Ledge height ∿1000Å. Ledge spacing ∿1.4μm
13	oxygen partial pressure 1.5×10^{-7} torr	2	point-bottomed pits with <11$\bar{2}$0> ledges. Ledge height ∿800A. Ledge spacing ∿1μm. A small density of macrokinks were observed in the ledges.
16	oxygen partial pressure 4.5×10^{-7} torr	3	point-bottomed pits with <11$\bar{2}$0> ledges. Ledge height ∿800Å. Ledge spacing ∿1μm. Pile up of macrokinks at ledge corners.
18	oxygen partial pressure 6.5×10^{-7} torr	4	point-bottomed pits with <11$\bar{2}$0> ledges. Ledge height ∿800Å. Ledge spacing ∿1.2μm. A high density of macrokinks in the ledges.

continued ...

TABLE 8 (continued)

EFFECT OF OXYGEN ON EVAPORATION MORPHOLOGY

Sample N Number	Experimental Conditions	Pit Density ($\times 10^{4}$ cm^{-2})	Observations
15	oxygen partial pressure 8×10^{-7} torr	4	rounding of pits, with the disappearance of crystallographic ledge structure.
10	oxygen partial pressure 1.1×10^{-6} torr	1	round pits with no ledge structure.

TABLE 9

EFFECT OF BULK PURITY ON EVAPORATION MORPHOLOGY

Sample Number	Approximate Bulk Purity (% Zn)	Pit Density (x 10^4 cm^{-2})	Observations
24	99.9999	8	shallow point-bottomed pits with <5% of total density deeper than the rest. Very straight $\langle 11\bar{2}0\rangle$ ledges. Ledge height $\sim$2000Å. Ledge spacing $\sim$2μm.
1	99.999	2	density less than in 24. 10% of total density were deeper than the rest. Straight $\langle 11\bar{2}0\rangle$ ledges. Ledge height $\sim$1400Å. Ledge spacing $\sim$2μm.
25	99.99	1	deep, faceted pits with rough ledge structure. Pile up of macrokinks at intersection of $\langle 11\bar{2}0\rangle$ ledges. Ledge height $\sim$ 800Å. Ledge spacing $\sim$ 1.25μm.
26	<99.99	1	round pits on rough surface. Resolvable ledge structure in pits absent.

TABLE 10

COMPARISON OF THE DENSITIES OF CHEMICAL AND THERMAL MACROPITS

Sample	Chemical Pit Density ($\times 10^{-3}$ cm^{-2})	Thermal Pit Density ($\times 10^{-3}$ cm^{-2})	Purity (% Zn)
24	2	0.8	99.9999
1	2	2	99.999
9	3	1.2	99.999
25	16	8	99.99

TABLE 11

POSSIBLE SECOND PHASE PRECIPITATES IN Zn SINGLE CRYSTALS

Element	Phase (77, 78)	Structure (77, 78)	Stability at 390°C	Vapor Pressure at 390°C (torr) (98)
Fe	ξ	92.8 at. %.Zn(300°C) Monoclinic with 28 atoms/unit cell. Fe Zn_{13}	very stable	$<< 10^{-11}$
Si	Pure Si	Diamond structure	--	$<< 10^{-11}$
Ni	δ	89 at.% Zn at 25°C Uncertain structure Ni_4Zn_{31}	stable to 490°C	$<< 10^{-11}$
Pb	Pure Pb	F.C.C.	--	10^{-7}
Sn	Pure Sn	Tetragonal	--	10^{-13}
Mn	ξ	92.95 at.% Zn. Monoclinic, isostructural with ξ Zn-Fe	Eutectic at 416°C. Probably in solid solution above 200°C	10^{-11}
Mg	Partial System	84.62 at.% Zn. Cubic with 39 atoms/ unit cell. Mg_2Zn_{11}	Eutectic at 367°C. Probably in solid solution above 200°C	10^{-3}
Cd	Pure Cd	H.C.P.	Probably in solid solution above 100°C	1
Zn	--	H.C.P.	--	7×10^{-2}

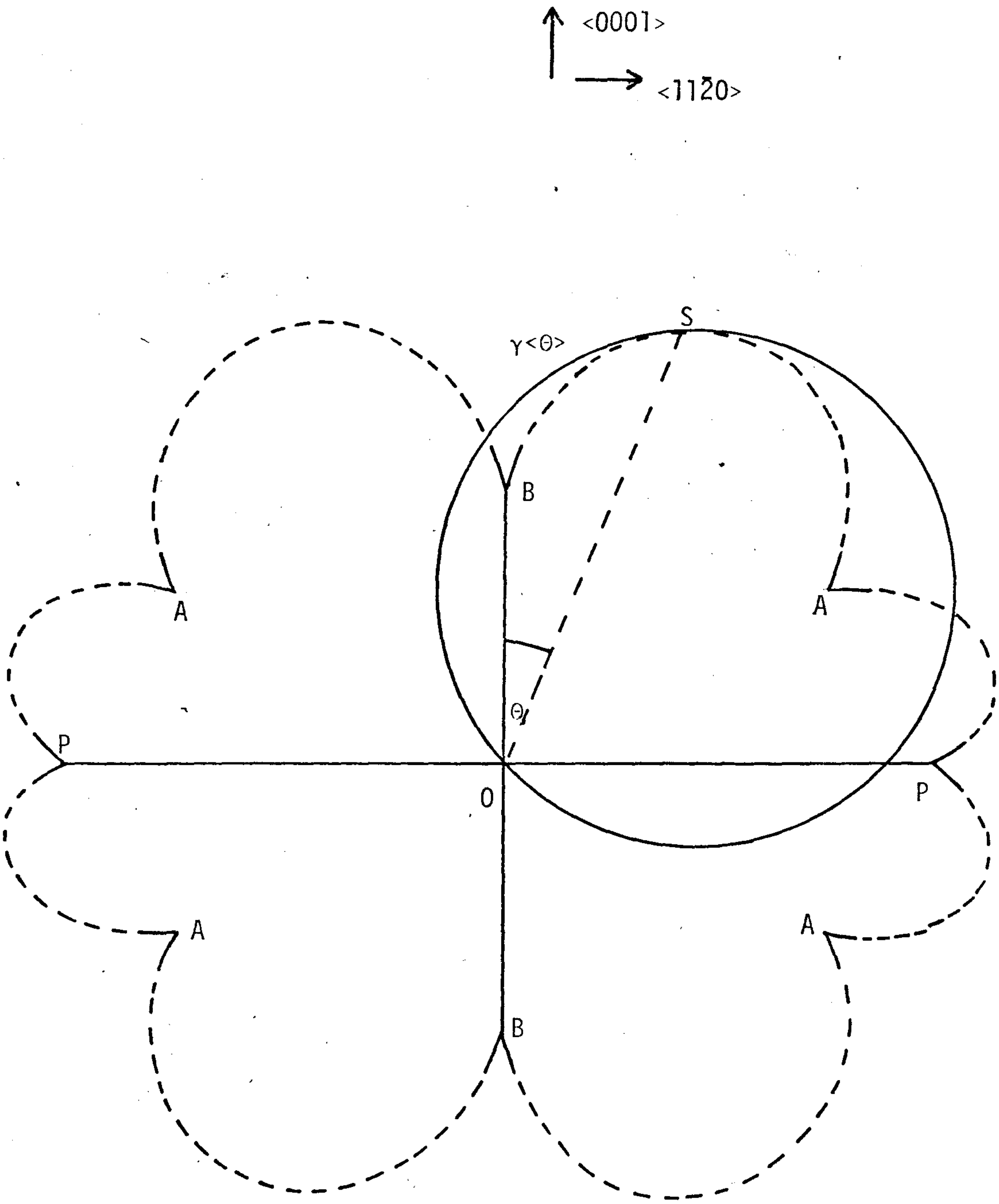

FIG. 1 - The <11$\bar{2}$0> zone of the γ-plot for zinc, based on experimental values for $\gamma_{(0001)}$, $\gamma_{(10\bar{1}1)}$ and $\gamma_{(10\bar{1}0)}$ reported by Miller et. al. (46).

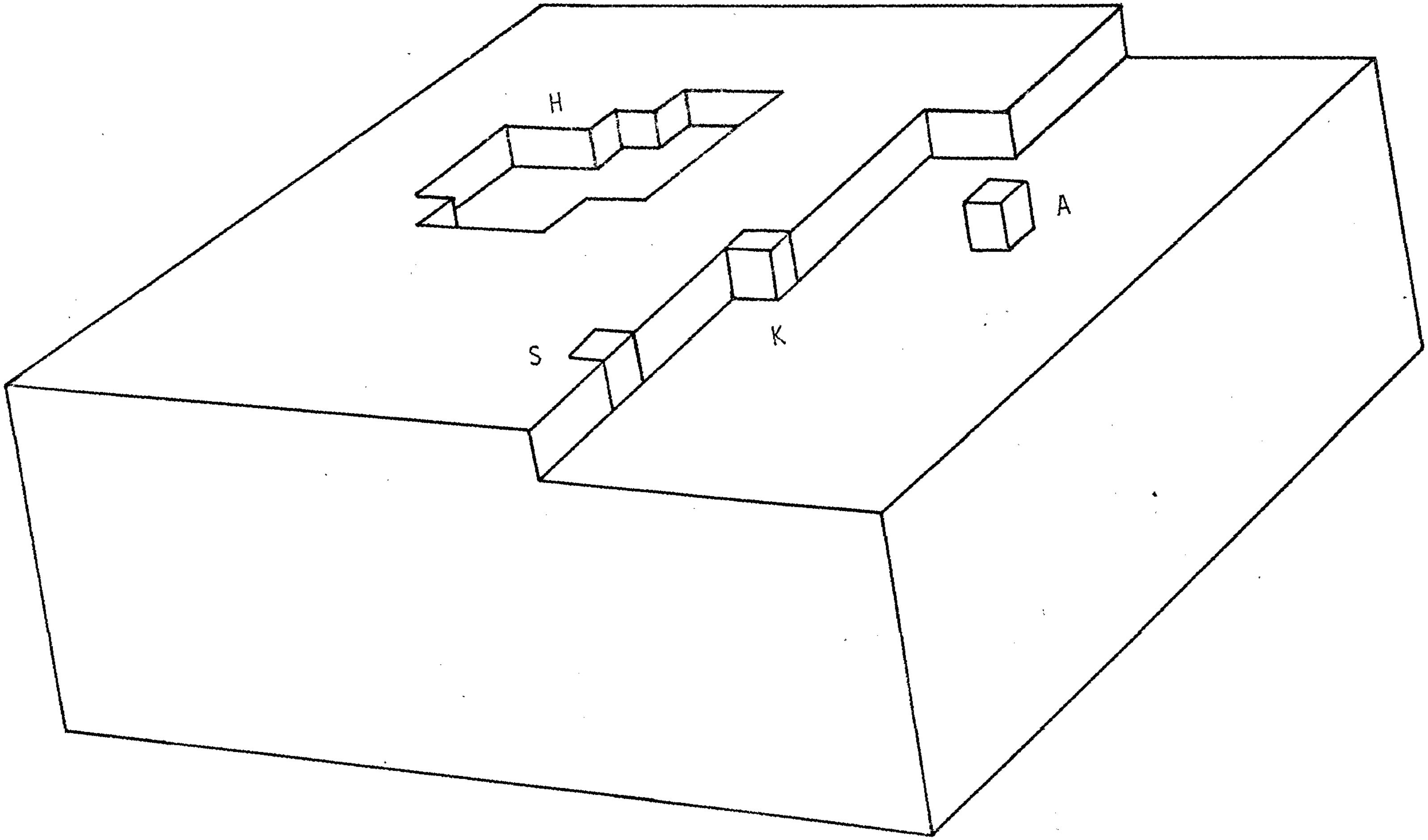

FIG. 2 - A schematic representation of an evaporating crystal surface.

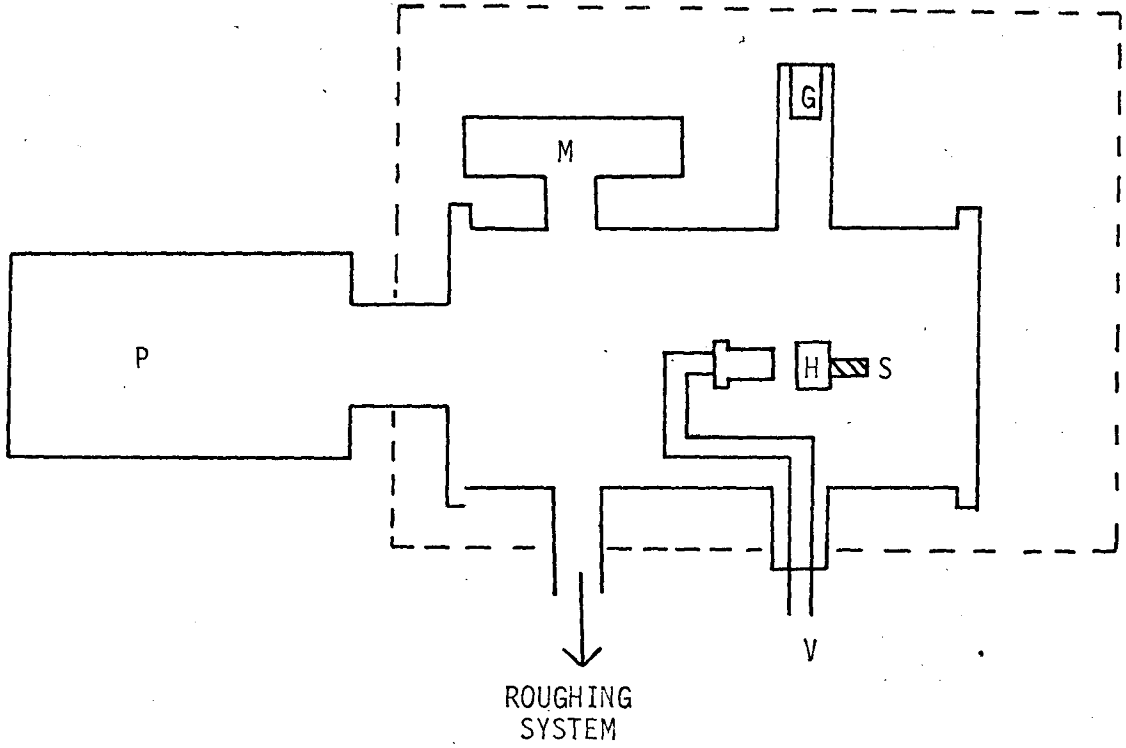

FIG. 3 - A schematic diagram of the U.H.V. system

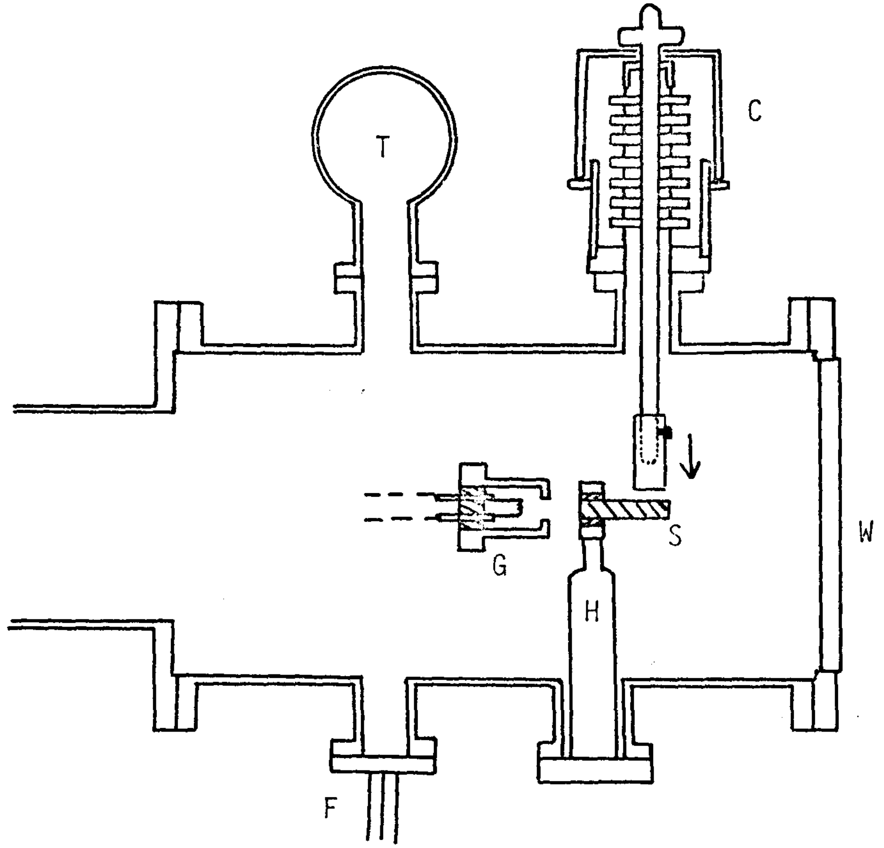

FIG. 4 - The ultra-high vacuum chamber

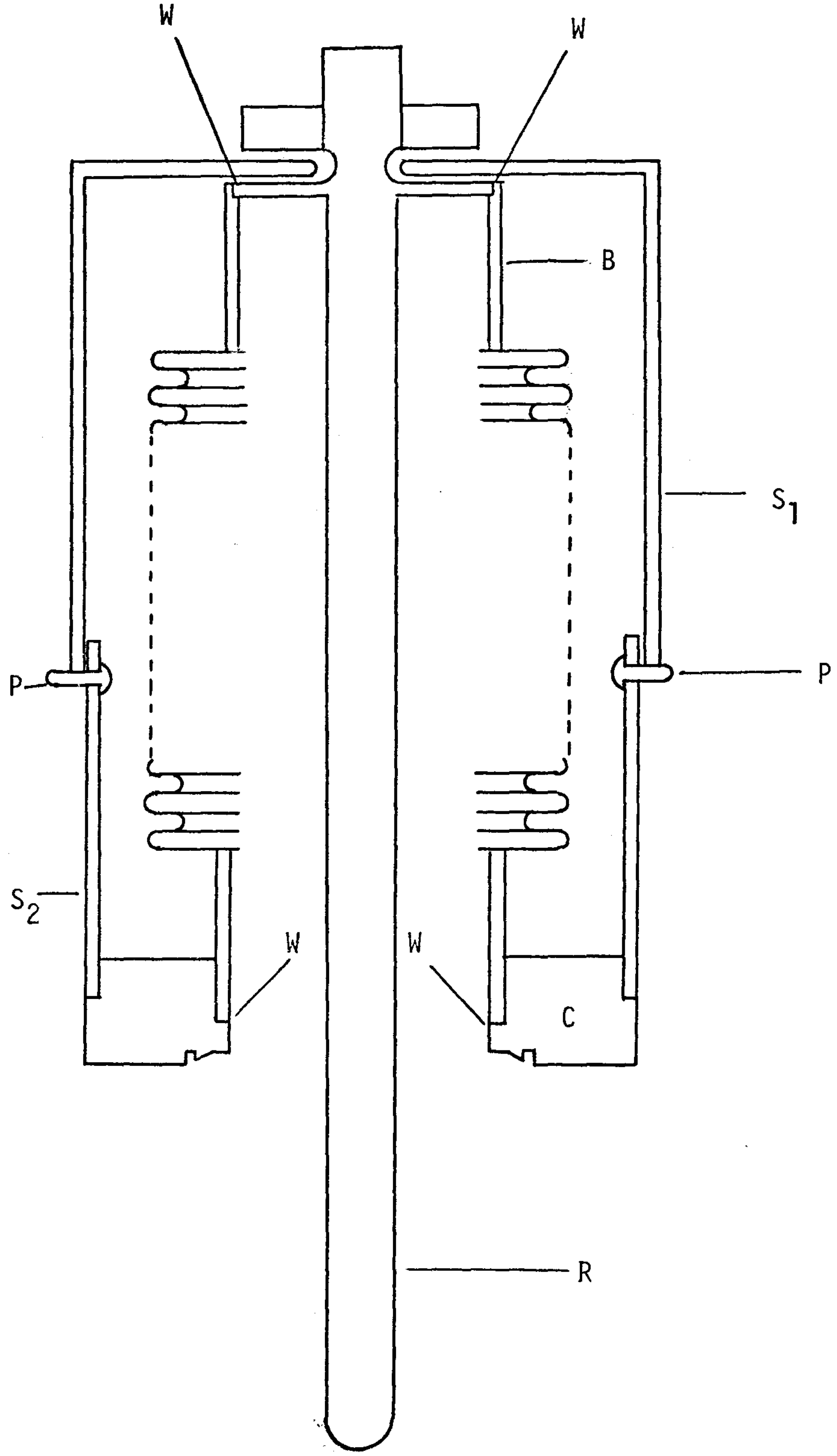

FIG. 5 - The linear motion feedthrough

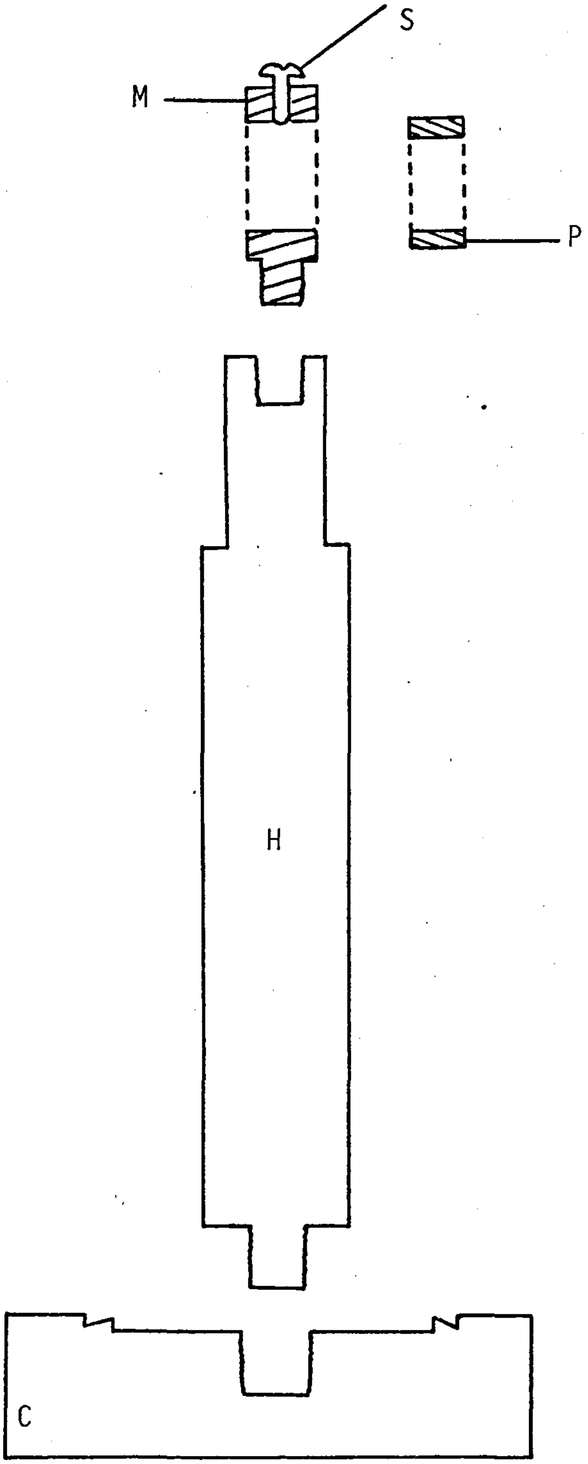

FIG. 6 - The crystal holder

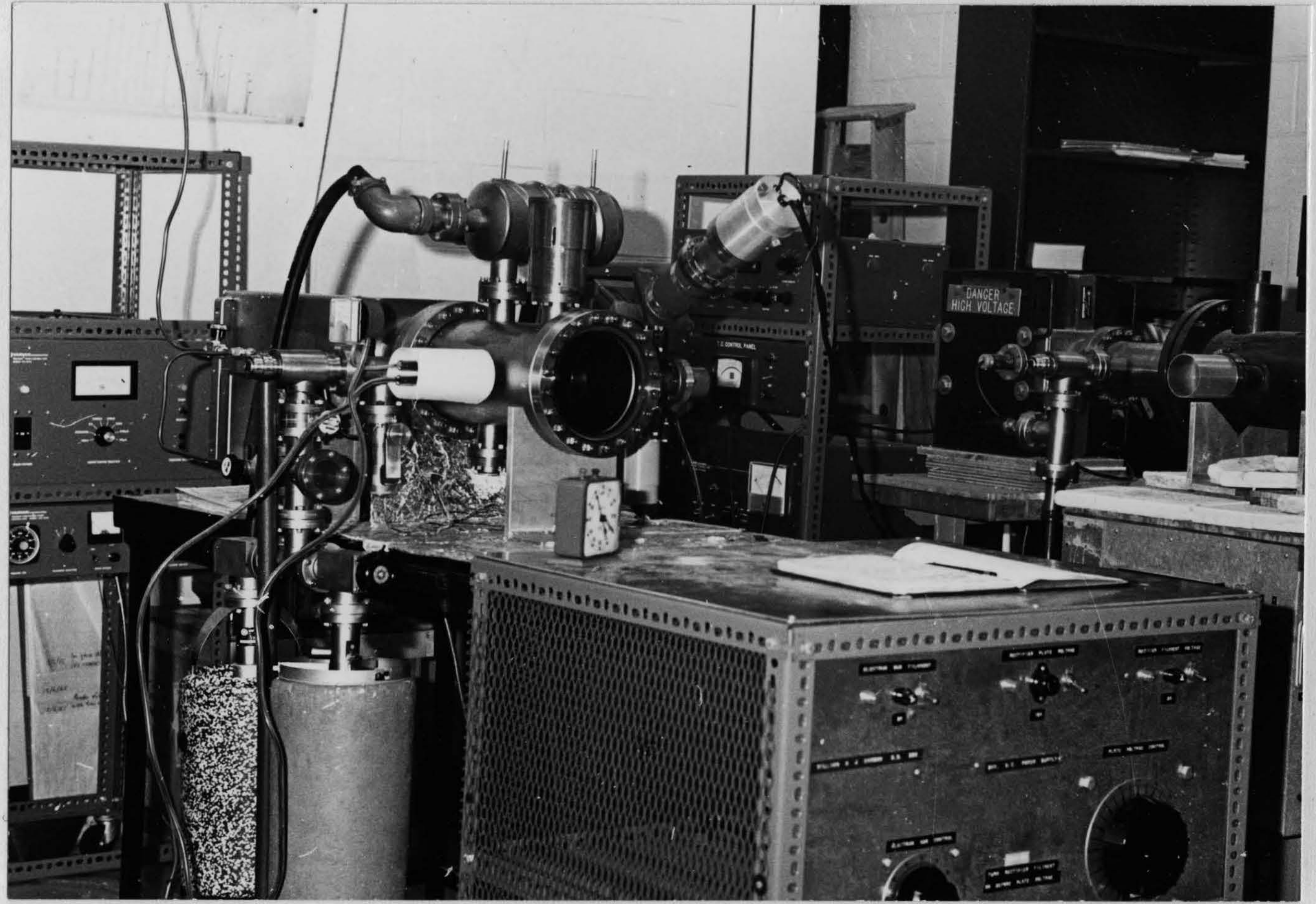

Fig 7 - Photograph of U.H.V. System

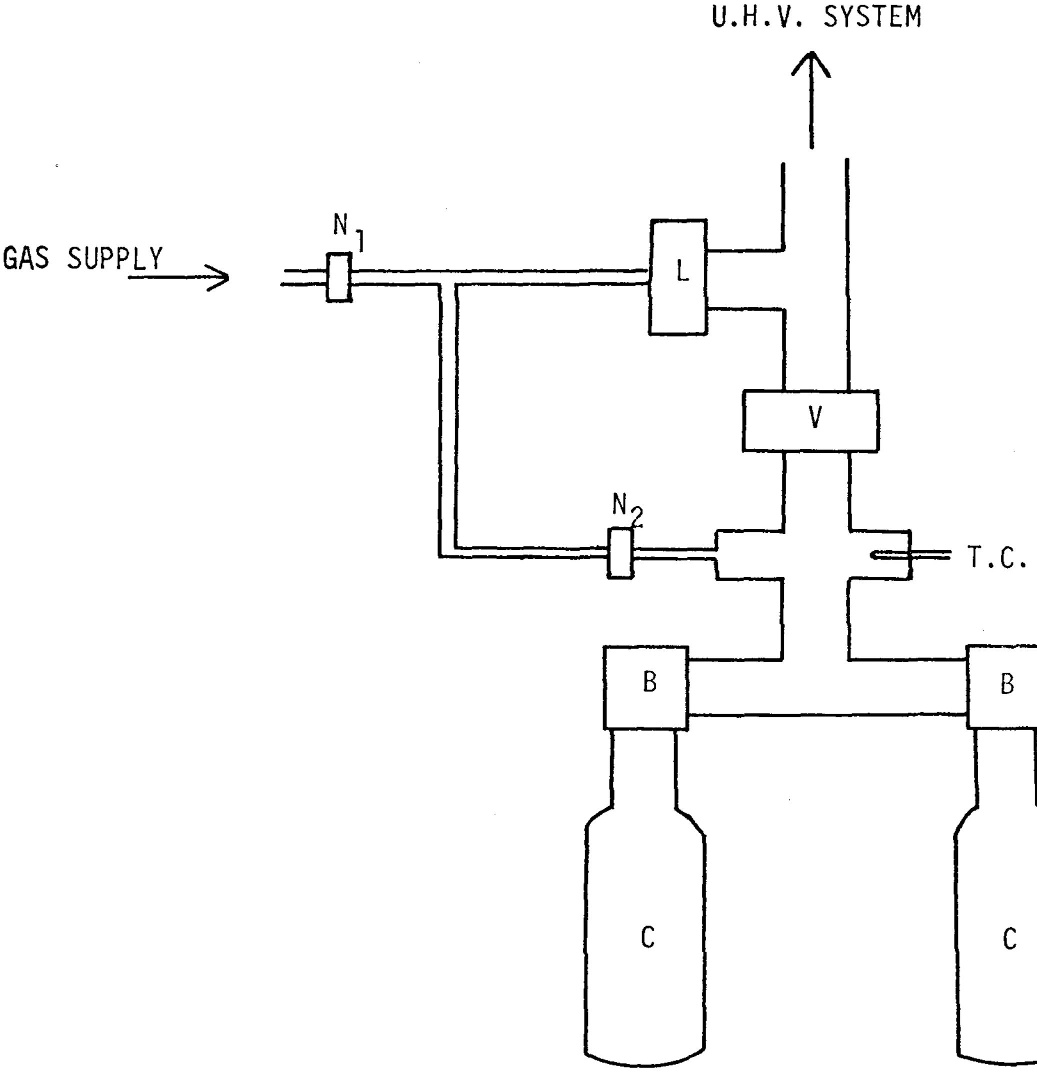

FIG. 8 - The roughing and gas-leak systems

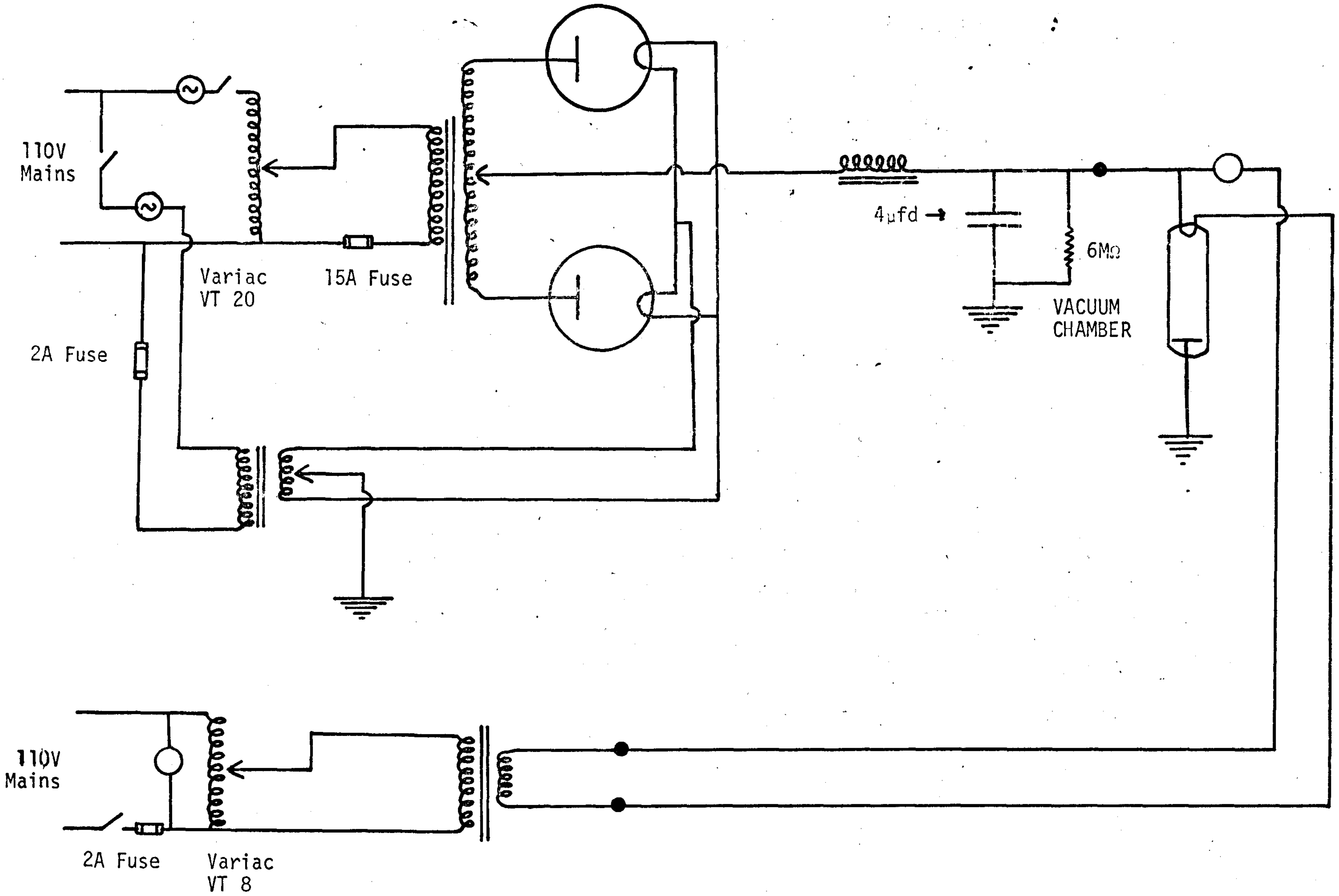

FIG. 9 - The electrical circuitry of 2K.V. D.C. power supply

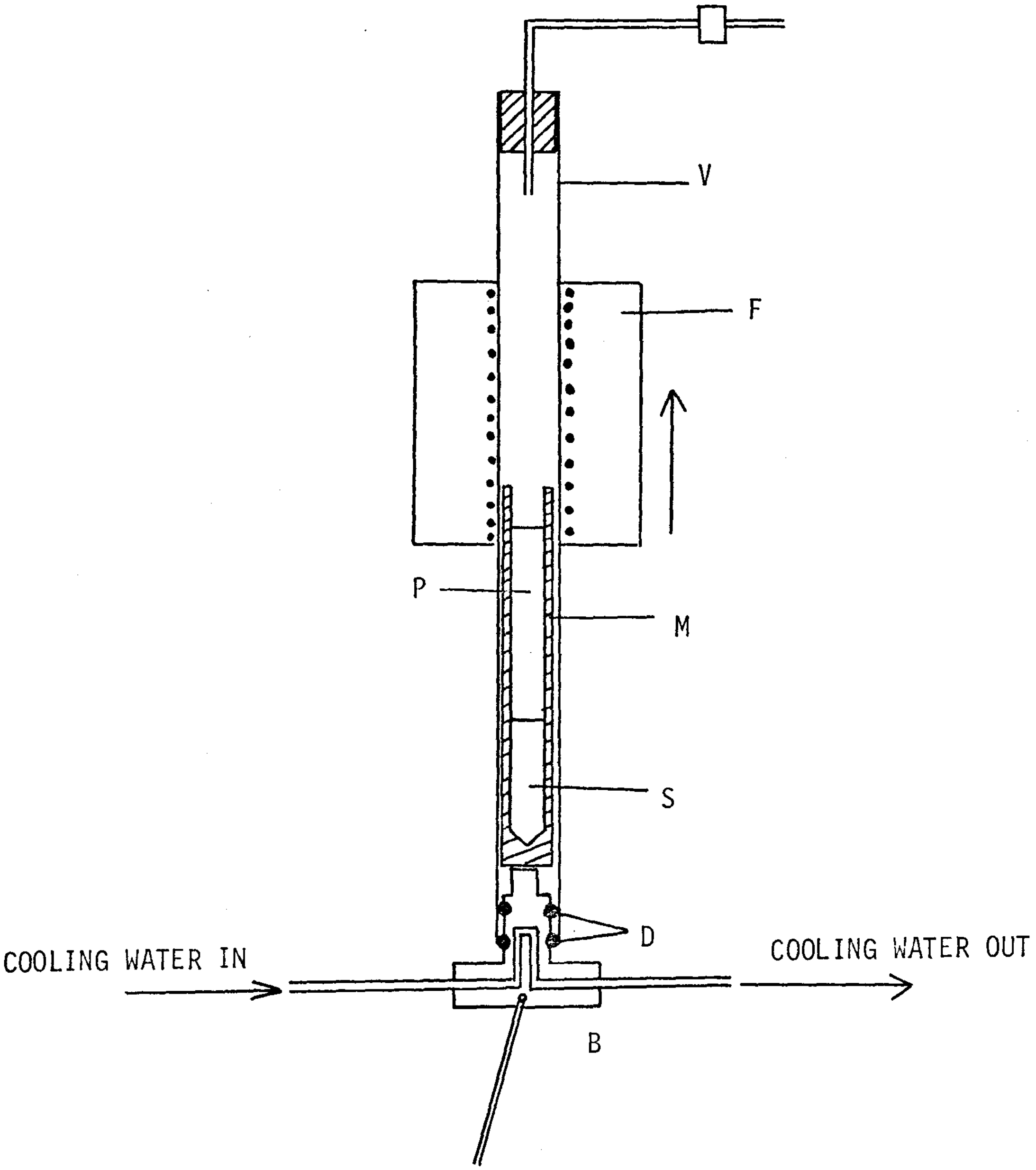

FIG. 10 - The crystal growing unit

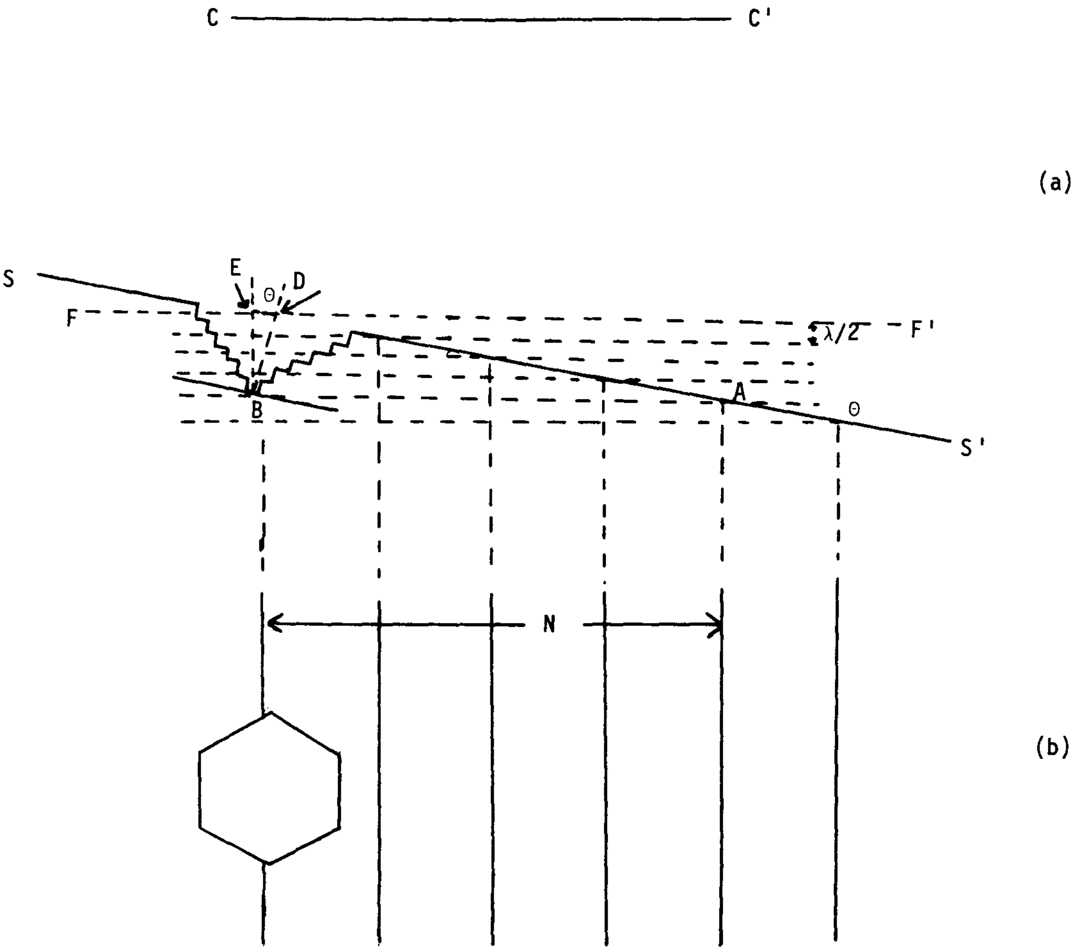

FIG. 11 - A diagrammatic representation of the method used for measuring pit depths

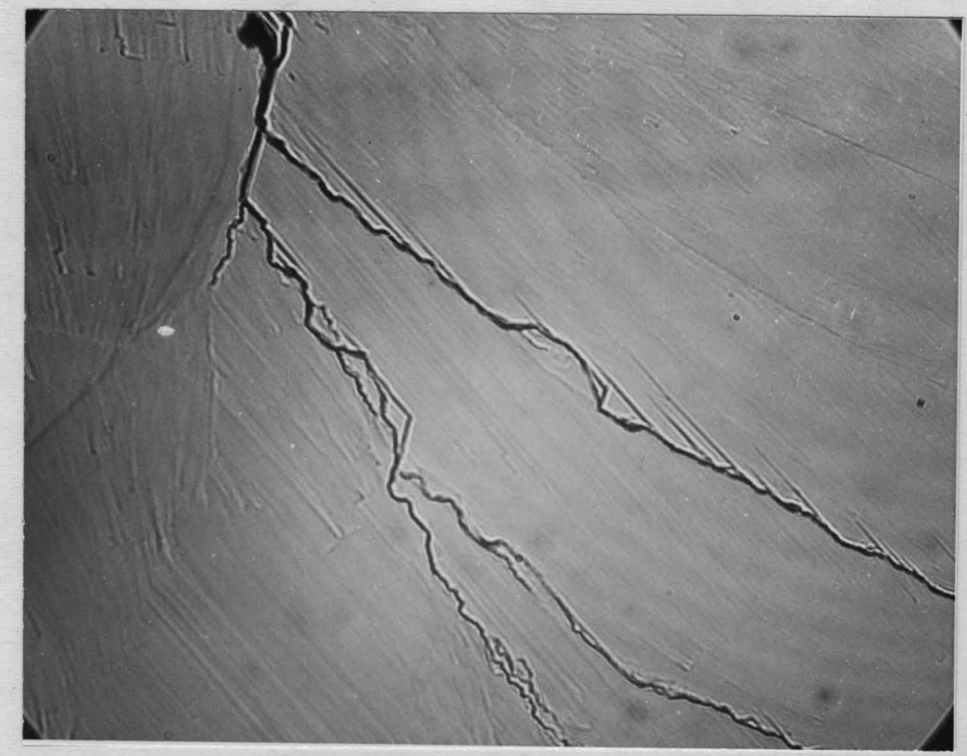

Fig. 12(a) - Optical micrograph of steps on freshly-cleaved surface (200x).

Fig. 12(b) - Interference micrograph of steps in (a) (500x).

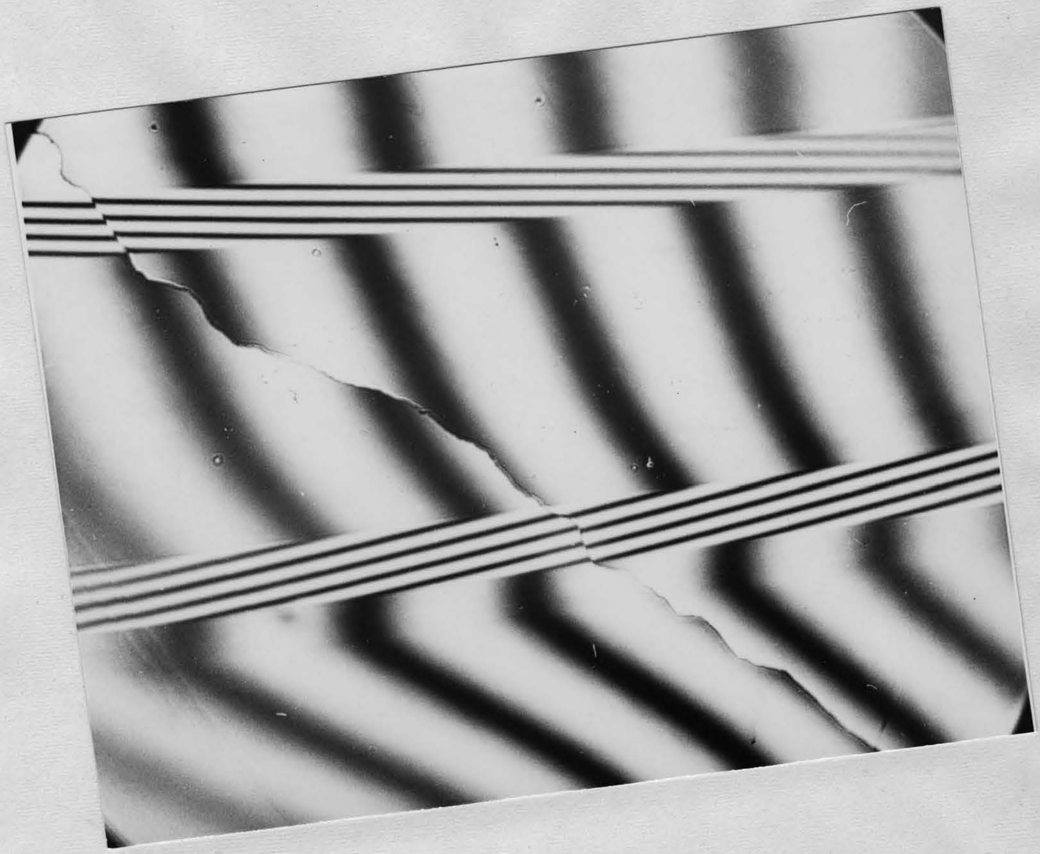

Fig. 12(c) - Interference Micrograph of deformation twins on freshly-cleaved surface (500x).

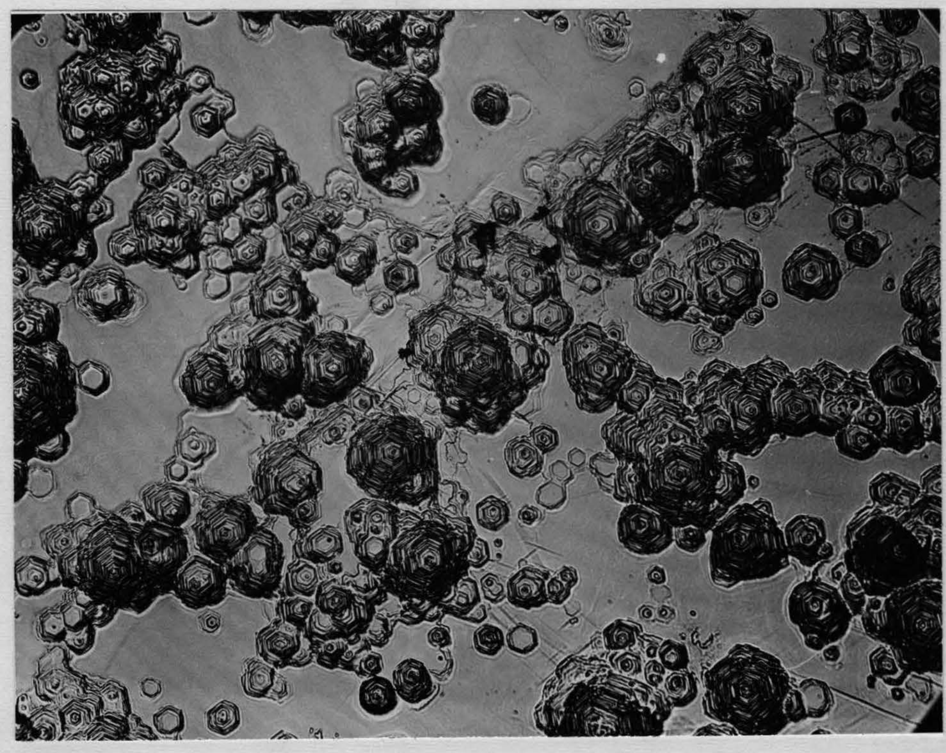

Fig. 13 - Optical micrograph of vacuum-evaporated (0001) zinc surface (100x).

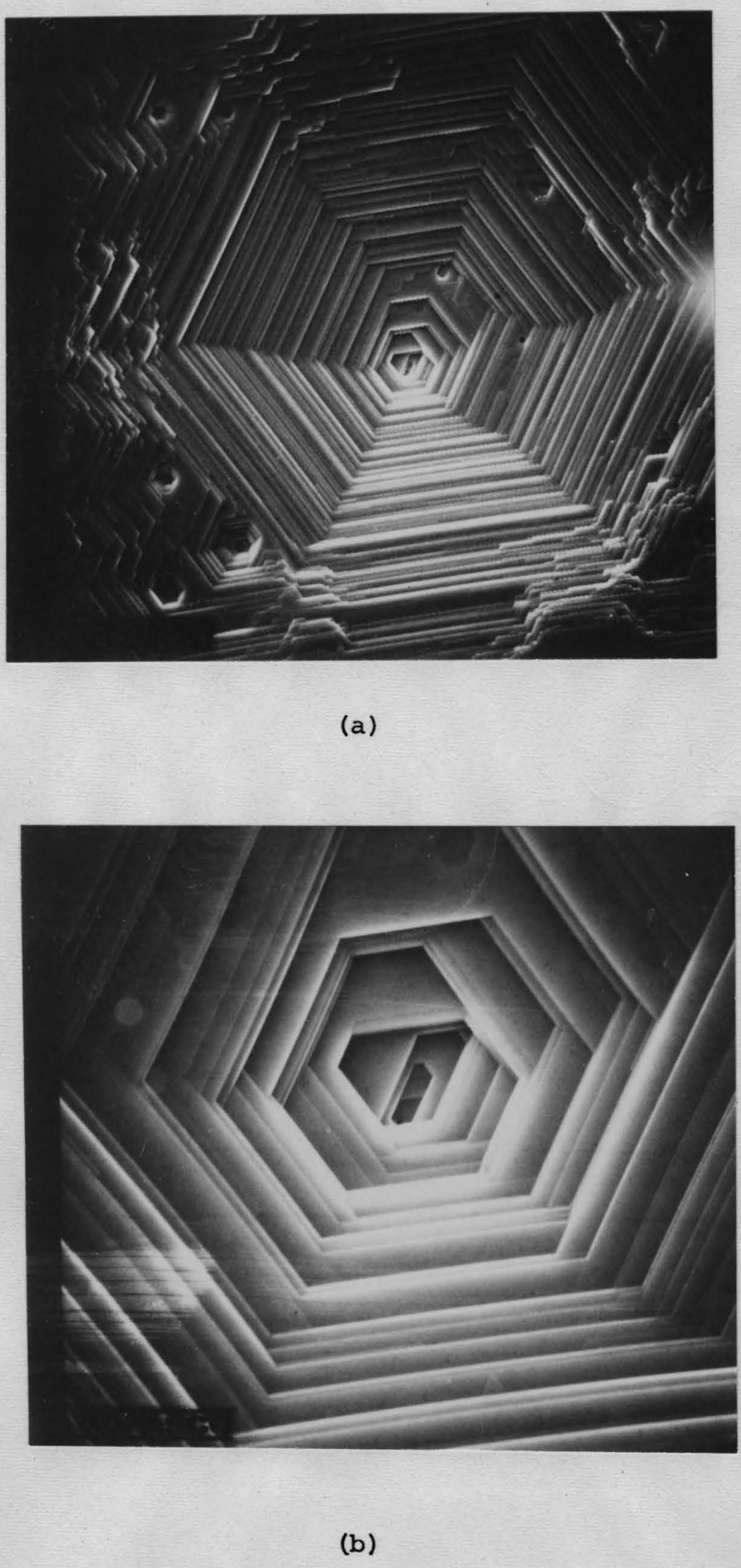

(a)

(b)

Fig. 14 - Scanning electron micrograph (S.E.M.) of evaporation pit (a) (600x; β = angle of tilt in scanning electron microscope = 0°); (b) (2400x, β = 0°)

Fig. 15 - S.E.M. of ledge structure in flat-bottomed pit (12,000x, $\beta = 35°$)

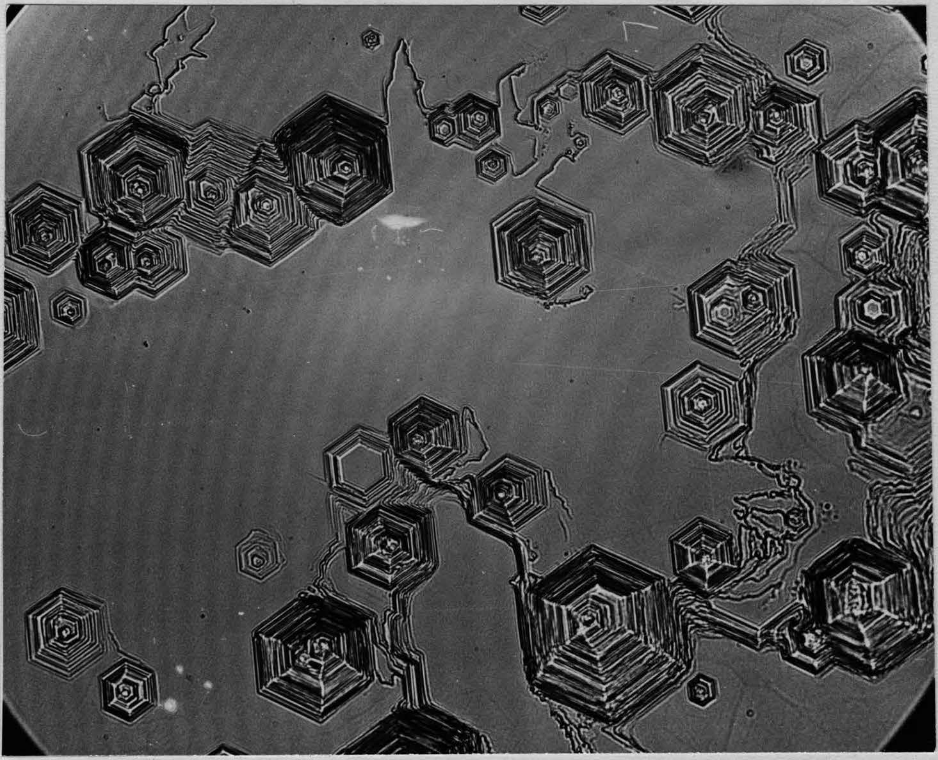

Fig. 16(a) - Optical micrograph of evaporation pits when the partial pressure of oxygen was 1.5 x 10^{-7} torr (200x).

Fig. 16(b) - S.E.M. of the ledge structure in a pit on the surface shown in (a) (2,200x, β = 35°).

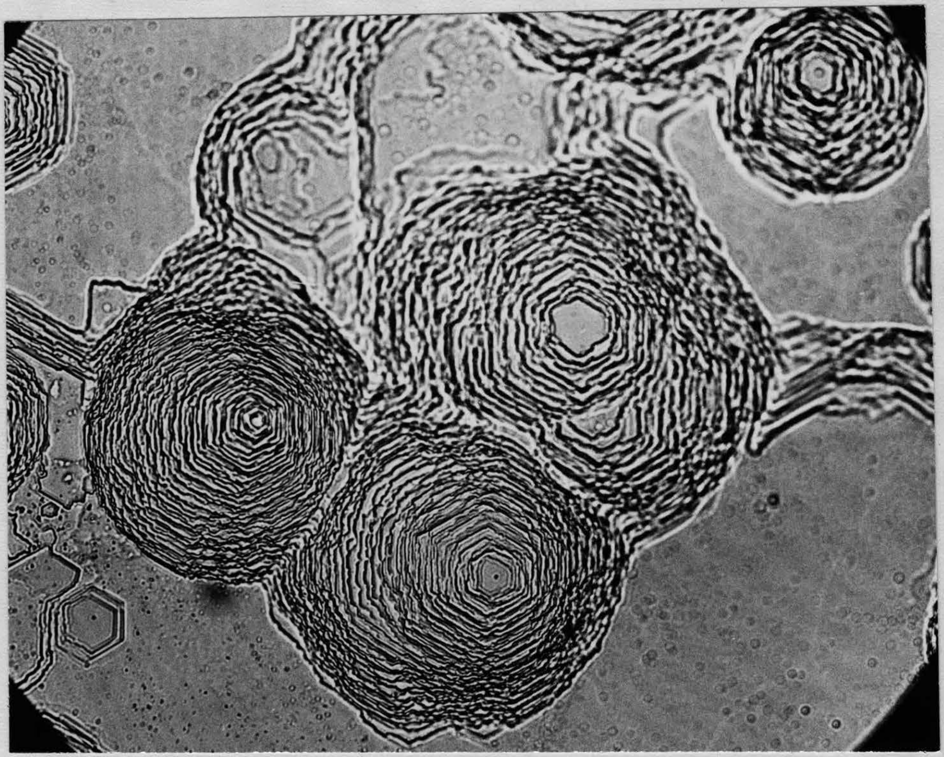

Fig. 17(a) - Optical micrograph of evaporation pits when the partial pressure of oxygen was 4.5 x 10^{-7} torr (500x).

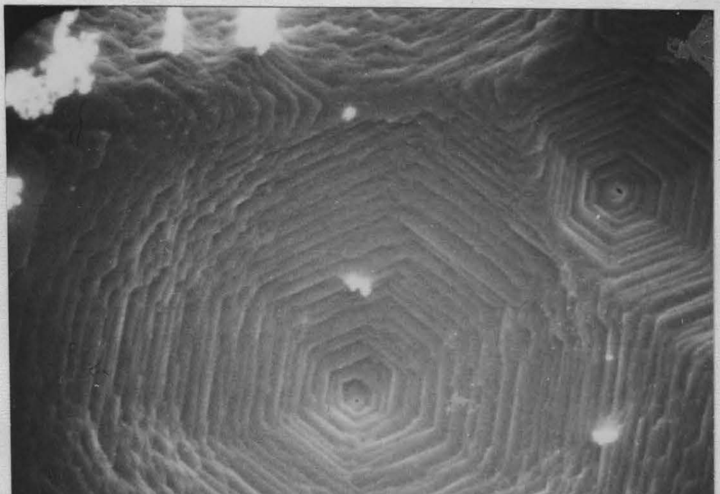

Fig. 17(b) - S.E.M. of the ledge structure in a pit on the surface shown in (a) (1,200x, β = 35°)

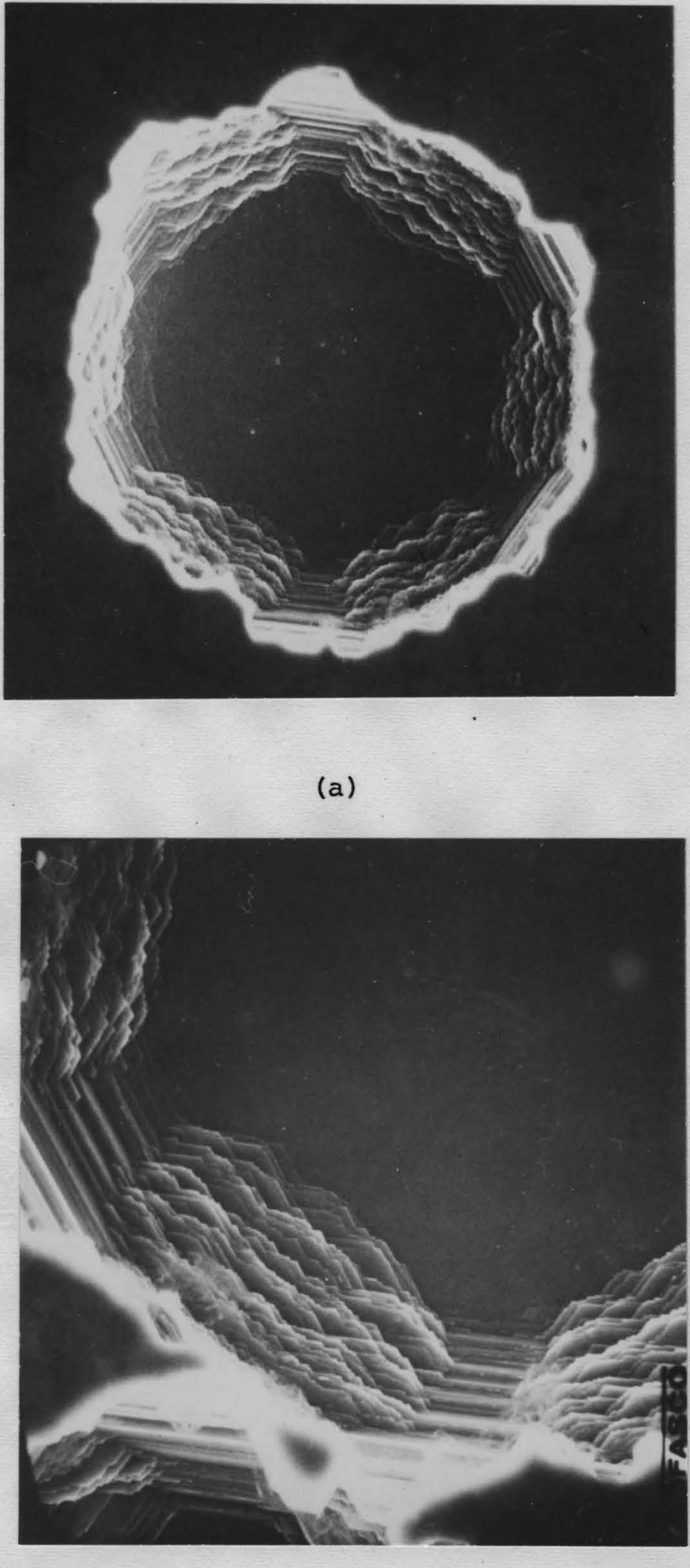

(a)

(b)

Fig. 18 - S.E.M. of macrokink "pile-up" in a flat-bottomed pit when oxygen partial pressure was 4.5×10^{-7} torr. (a) (600x, $\beta = 35°$); (b) (1,200x, $\beta = 35°$)

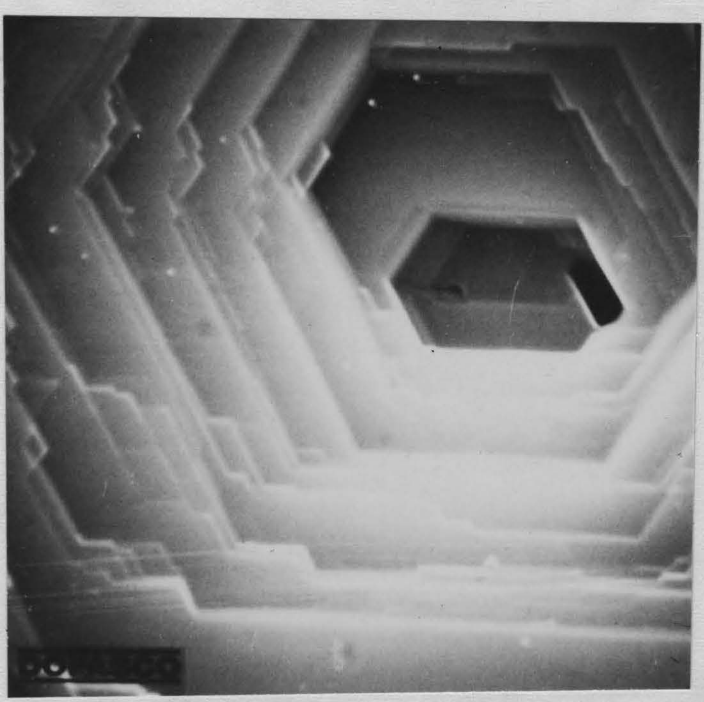

Fig. 19 - S.E.M. of the detailed ledge structure in a point-bottomed pit when the oxygen partial pressure was 4.5×10^{-7} torr (12,000x, $\beta = 45°$).

FIG. 20(a)- Low magnification S.E.M. of evaporation pits when the oxygen partial pressure was 6.5×10^{-7} torr. (240x, $\beta = 35°$).

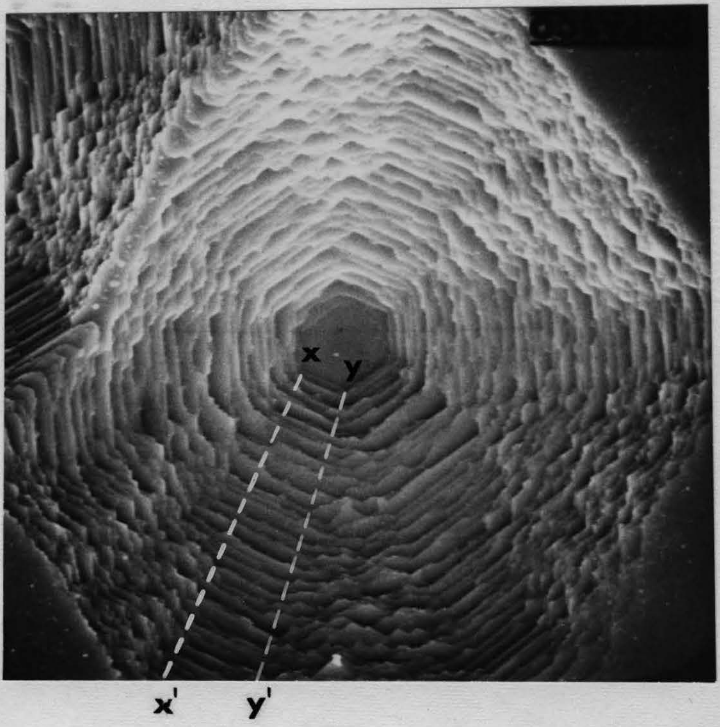

Fig. 20(b) - S.E.M. showing macrokink-ledge boundaries xx' and yy' in pit A (Fig. 20(a)) (1,200x, β ≐ 35°).

Fig. 20(c) - S.E.M. of detailed ledge structure in the pit shownin (b). (6,000x, β = 35°).

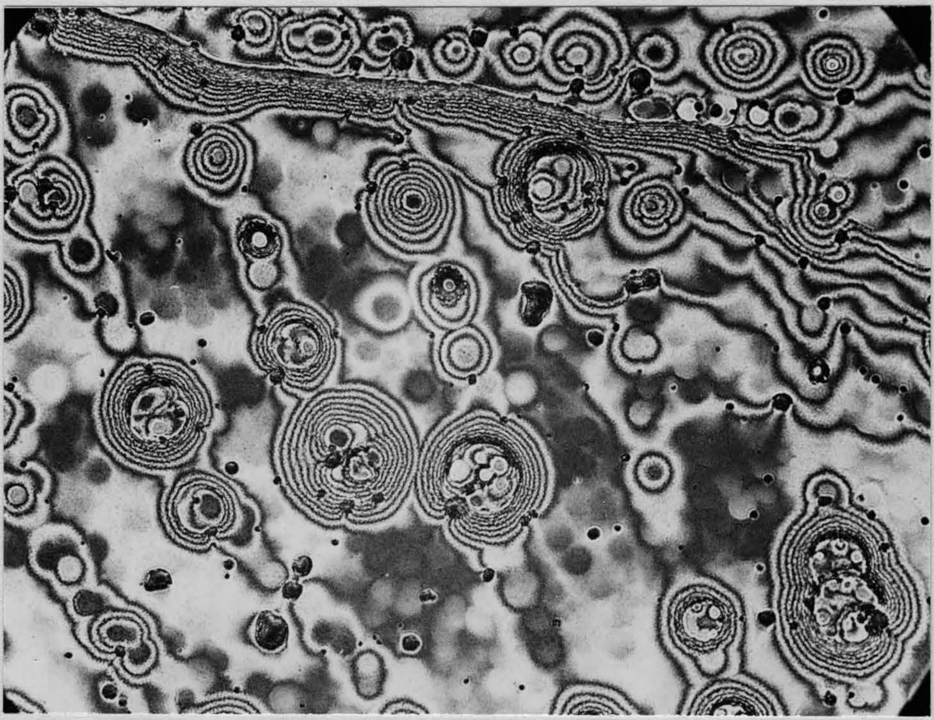

Fig. 21(a) - Interference micrograph of the evaporated surface when the oxygen partial pressure was 8×10^{-7} torr (200x).

Fig. 21(b) - Interference micrograph of a typical pit on the surface shown in (a). (500x).

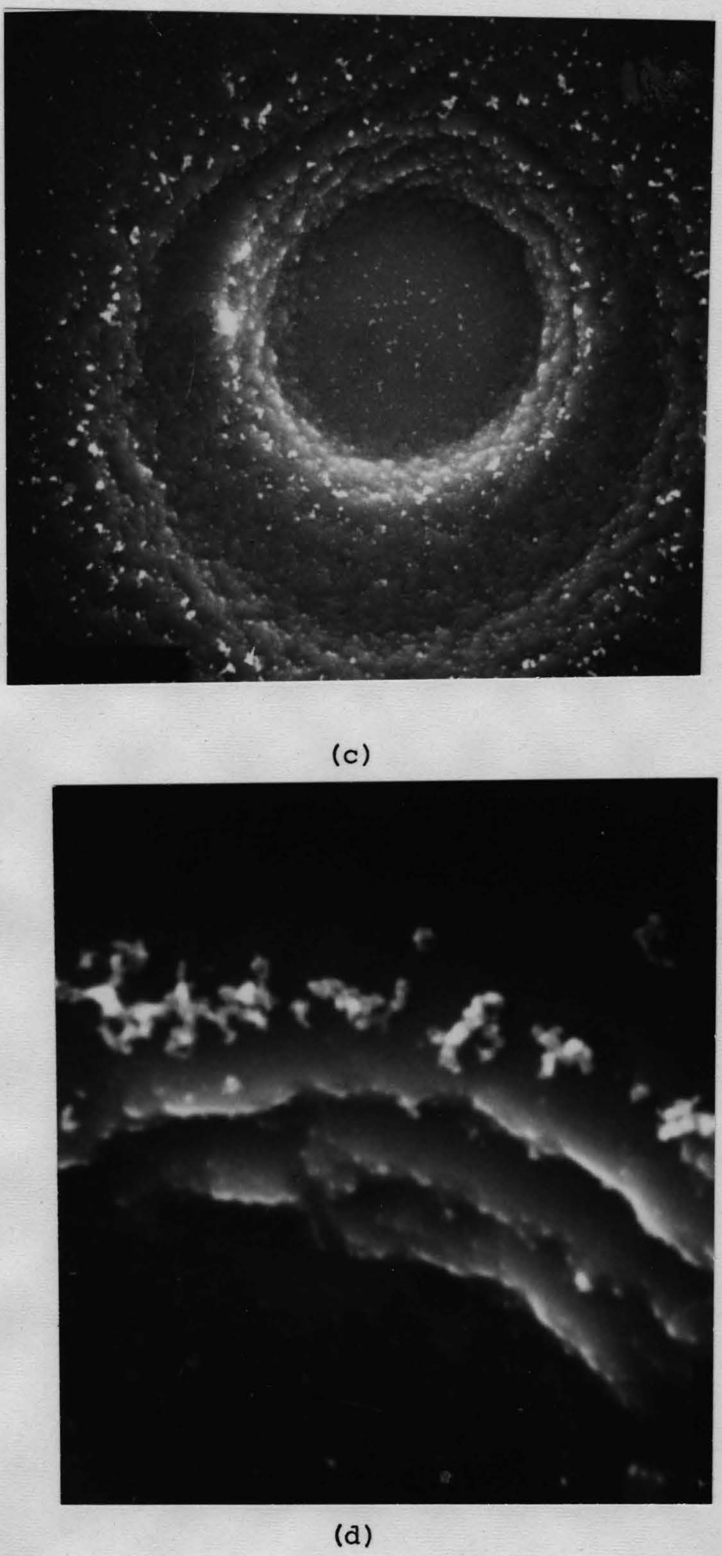

(c)

(d)

Fig. 21 - S.E.M. of the mottled ledge structure of a pit, similar to that shown in (b). (c) (2,400x, β = 35°) and (d) (12,000x, β = 35°).

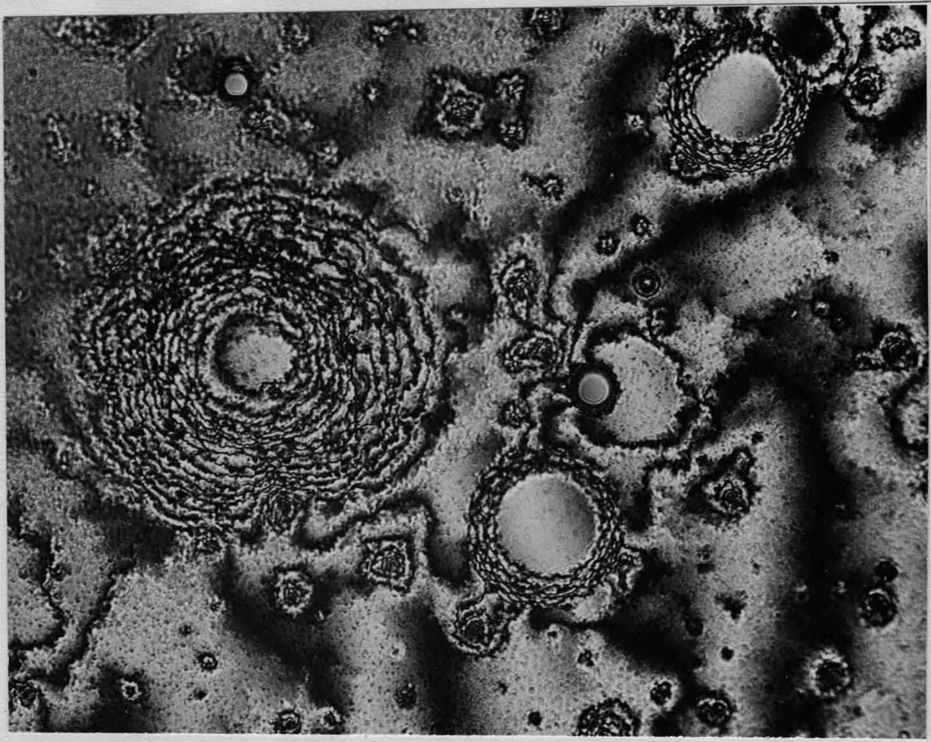

Fig. 22(a) - Interference micrograph of the evaporated surface when the partial pressure of oxygen was 1.1 x 10^{-6} torr (500x).

Fig. 22(b) - S.E.M. of the irregular morphology in a pit similar to that shown in (a) (2,400x, β = 25°).

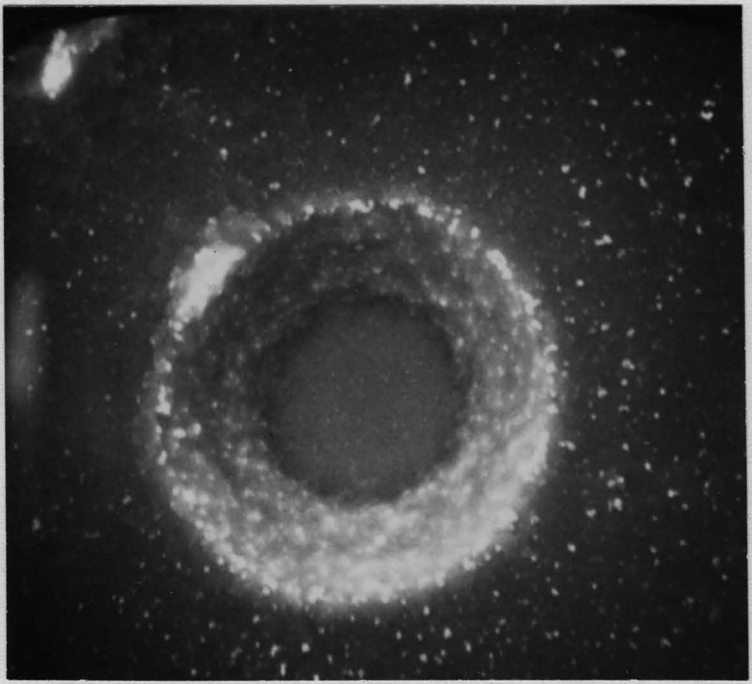

Fig. 22(c) - S.E.M. of a smooth-sided pit on the same surface (2,400x, β = 25°).

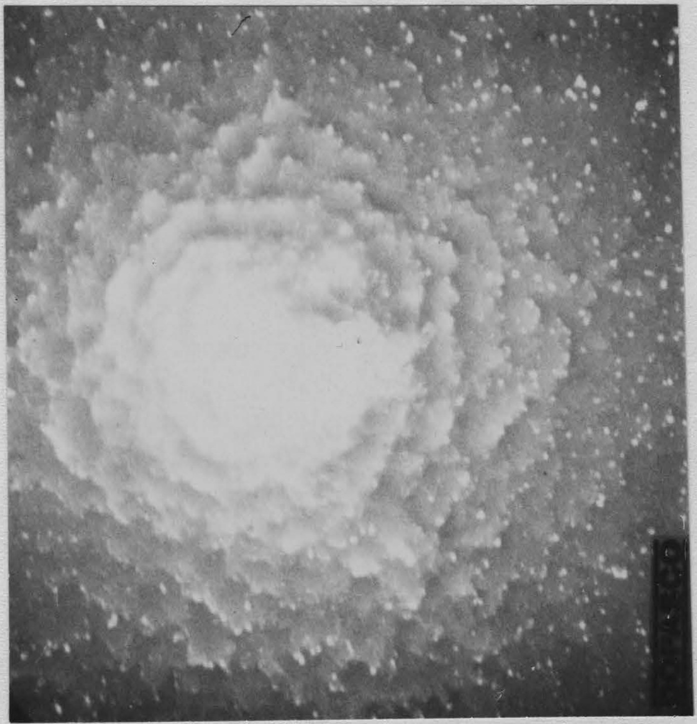

Fig. 22(d) - S.E.M. of a hillock on the surface shown in (a). (2,400x, β=25°).

Fig. 23 - S.E.M. showing the difference in contrast between point-bottomed pits and flat-bottomed pits (240x, $\beta = 35°$).

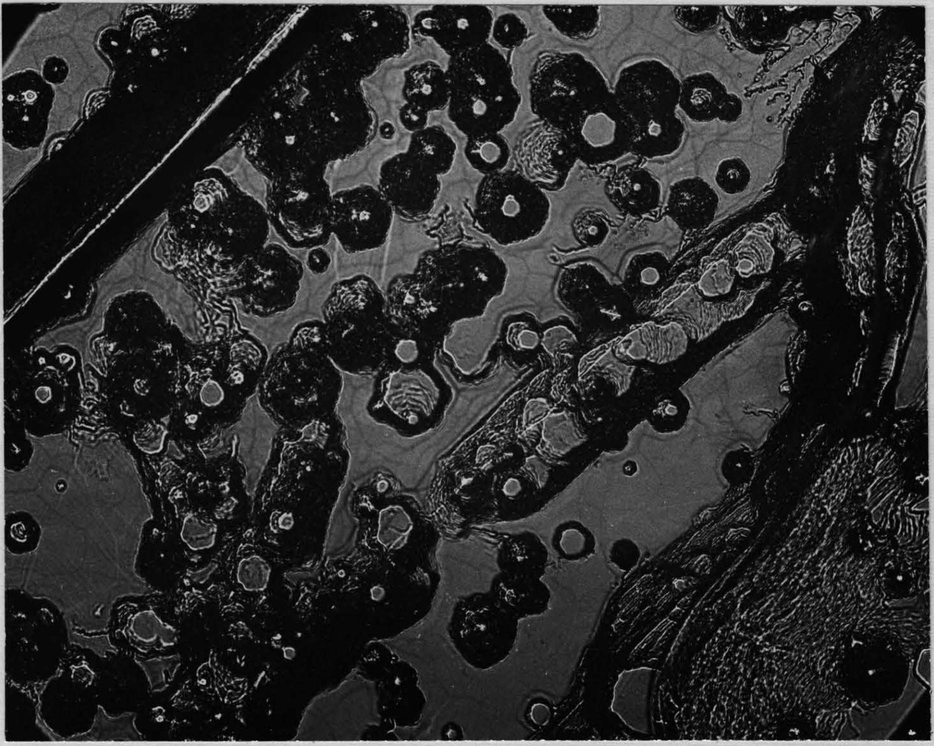

Fig. 24 - Optical micrograph showing high density of flat-bottomed pits at oxygen partial pressures > 5×10^{-7} torr (100x).

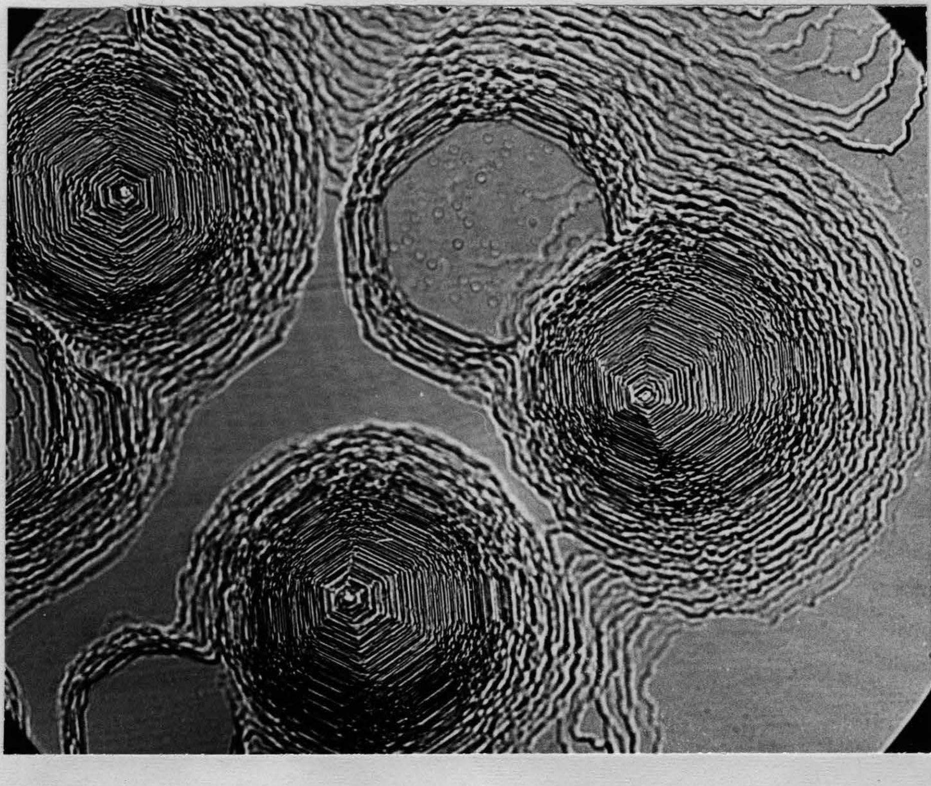

Fig. 25 - Optical micrograph of shallow "edge" in evaporation pits (500x).

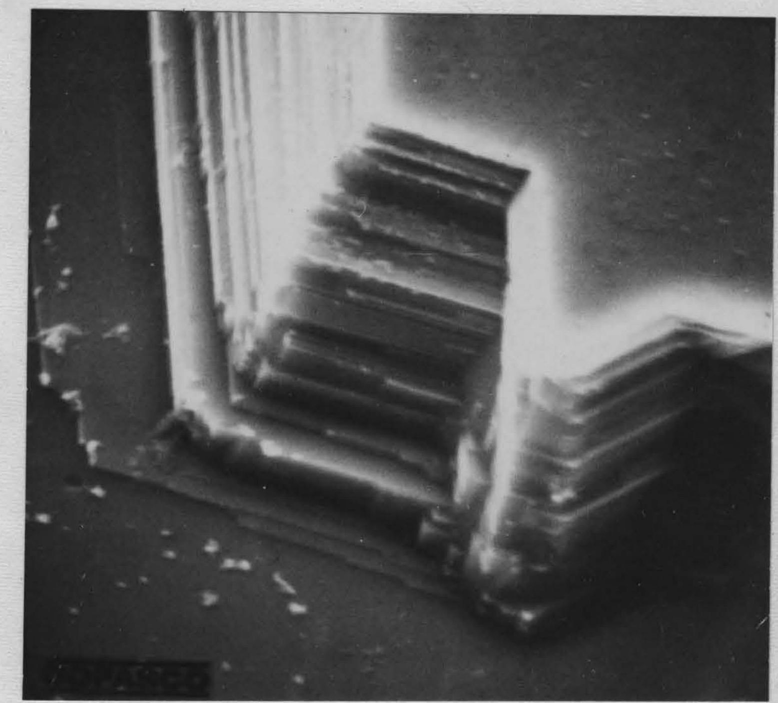

Fig. 26 - S.E.M. of unevaporated island on precleaved sample (6,000x, β = 45°).

Fig. 27(a) - Interference micrograph of evaporation pits on a precleaved sample. (500x).

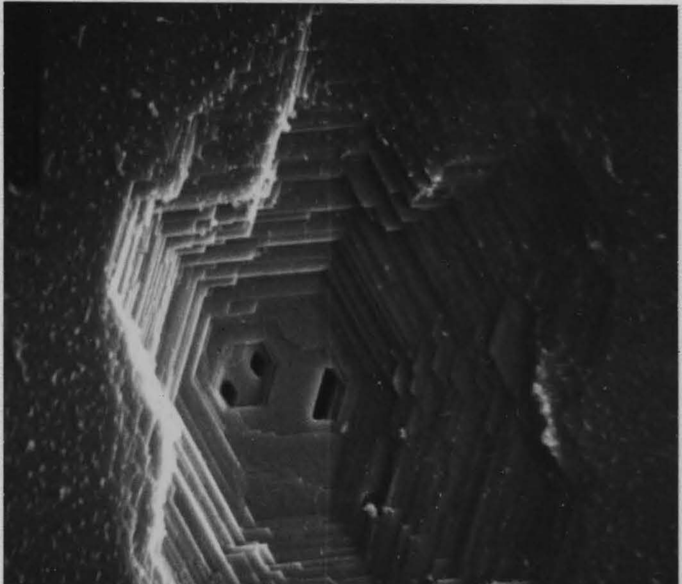

Fig. 27(b) - S.E.M. of an evaporation pit on a precleaved sample (6,000x, β = 45°).

Fig. 28 - S.E.M. of evaporation ledge structure on 99.9999% Zn sample (2,400x, β = 10°).

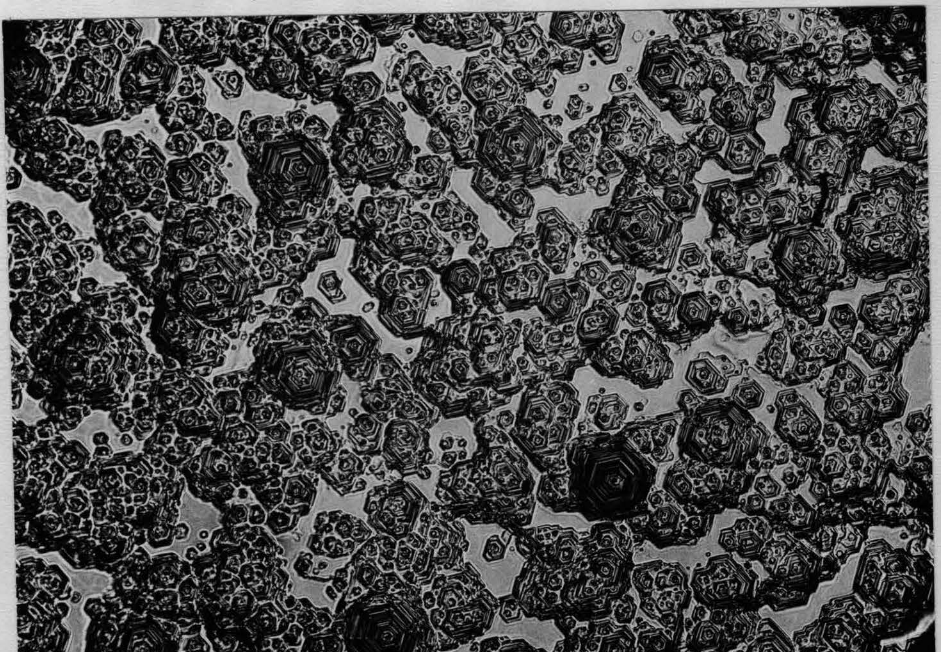

Fig. 29 - Optical micrograph, demonstrating a low density of deep pits on high purity samples (100x).

Fig. 30 - S.E.M. of evaporation ledge structure on 99.99% Zn sample (1,200x, $\beta = 10°$).

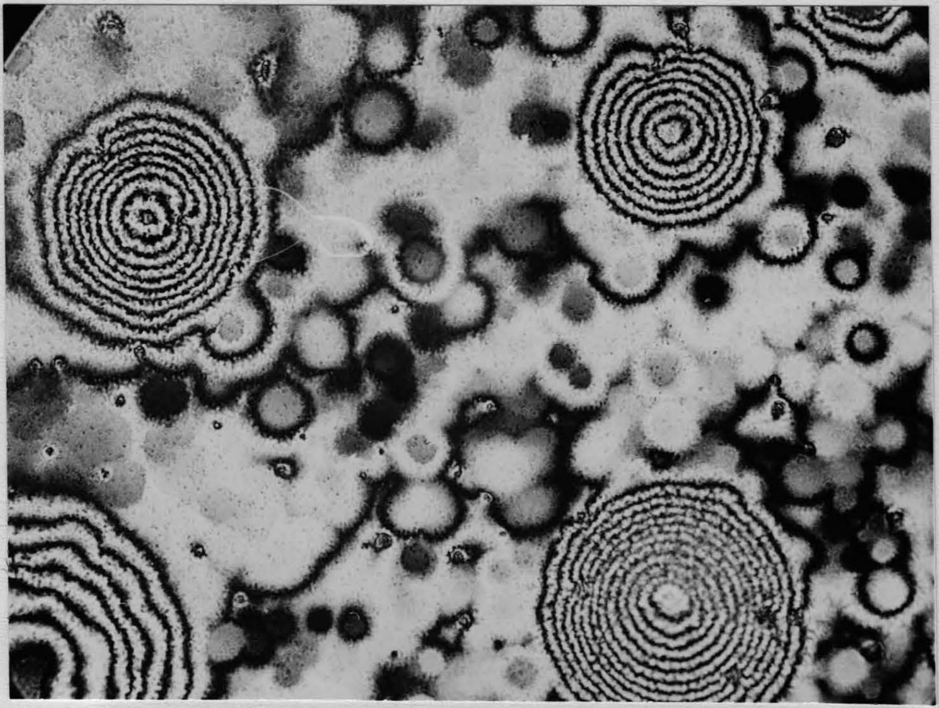

Fig. 31(a) - Interference micrograph of evaporated surface of <99.99% Zn sample (500x).

Fig. 31(b) - S.E.M. of a pit similar to those shown in (a). (2,400x, β = 10°).

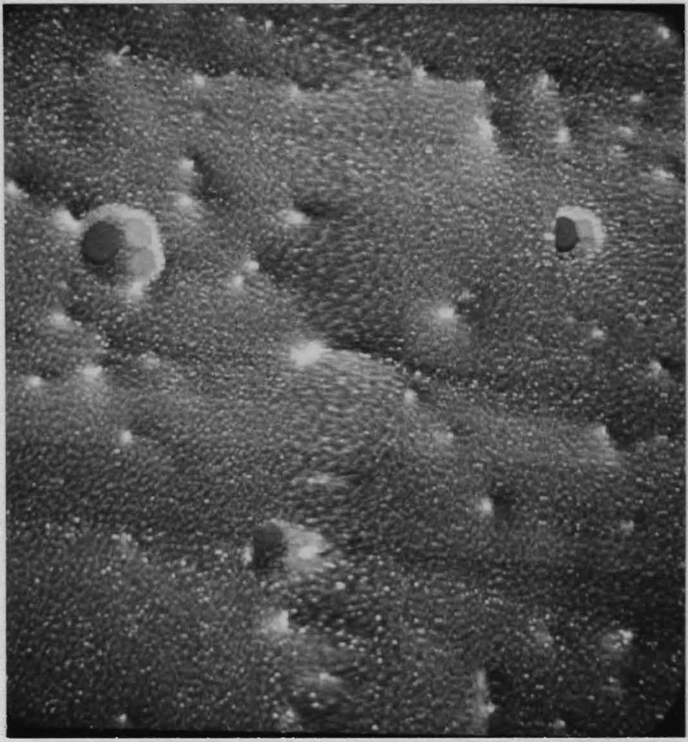

Fig. 32 - S.E.M., showing the rough evaporation morphology on a low purity Zn sample (600x, $\beta = 10°$).

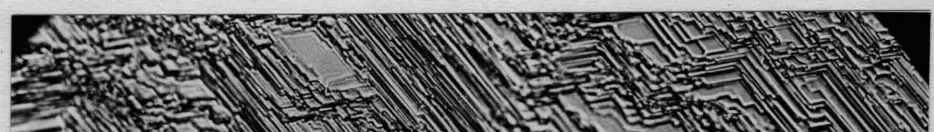

Fig. 33 - Optical micrograph of an evaporated non-basal surface (500x).

Fig. 34(a) - Optical micrograph of evaporation pits on non-basal orientations (500x).

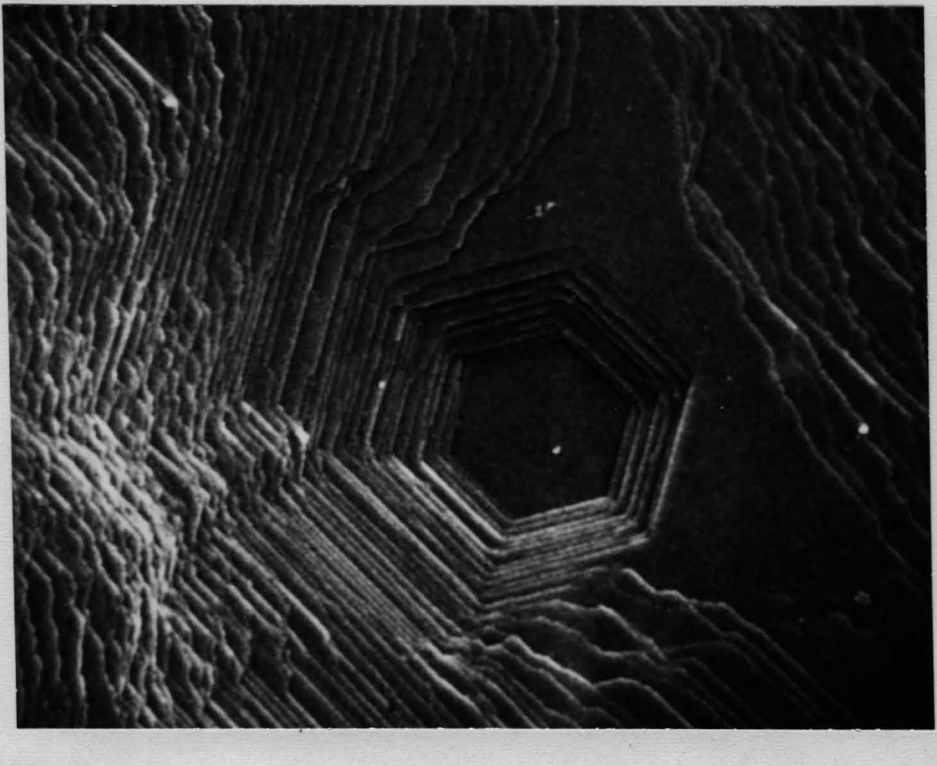

Fig. 34(b) - S.E.M. of an evaporation pit similar to those shown in (a) (1,200x, $\beta = 10°$).

Fig. 35(a) - S.E.M. of "hole" at the bottom of a deep pit.
(6,000x, β = 10°).

Fig. 35(b) - S.E.M. of "hole" at the bottom of a shallow pit.
(10,000x, β = 10°).

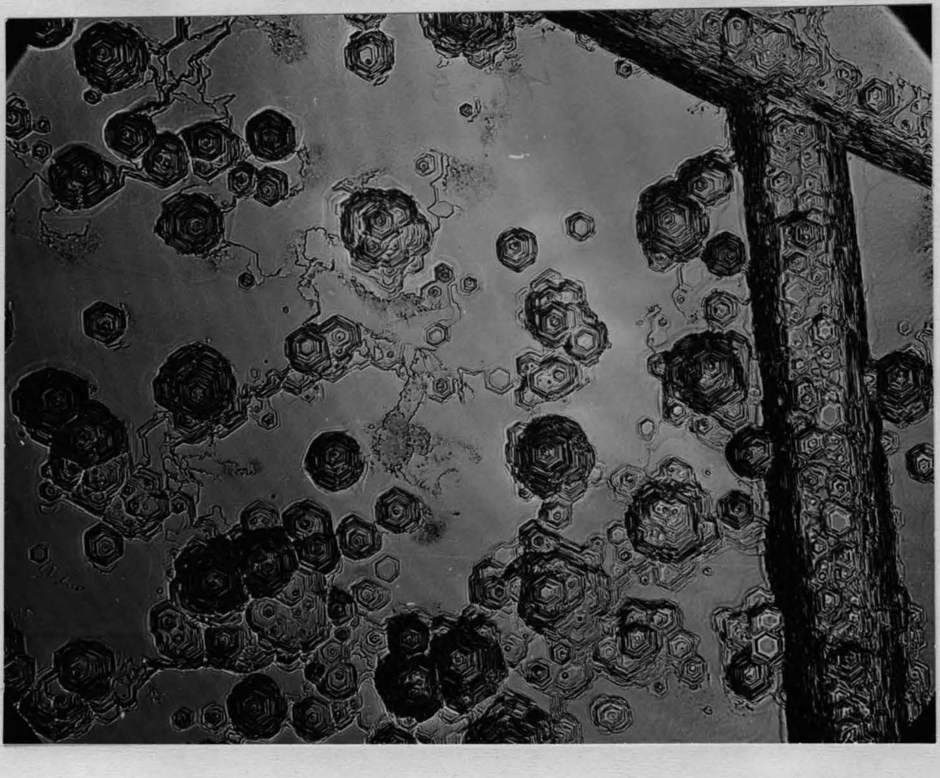

Fig. 36(a) - Optical micrograph of evaporated deformation twins (100x).

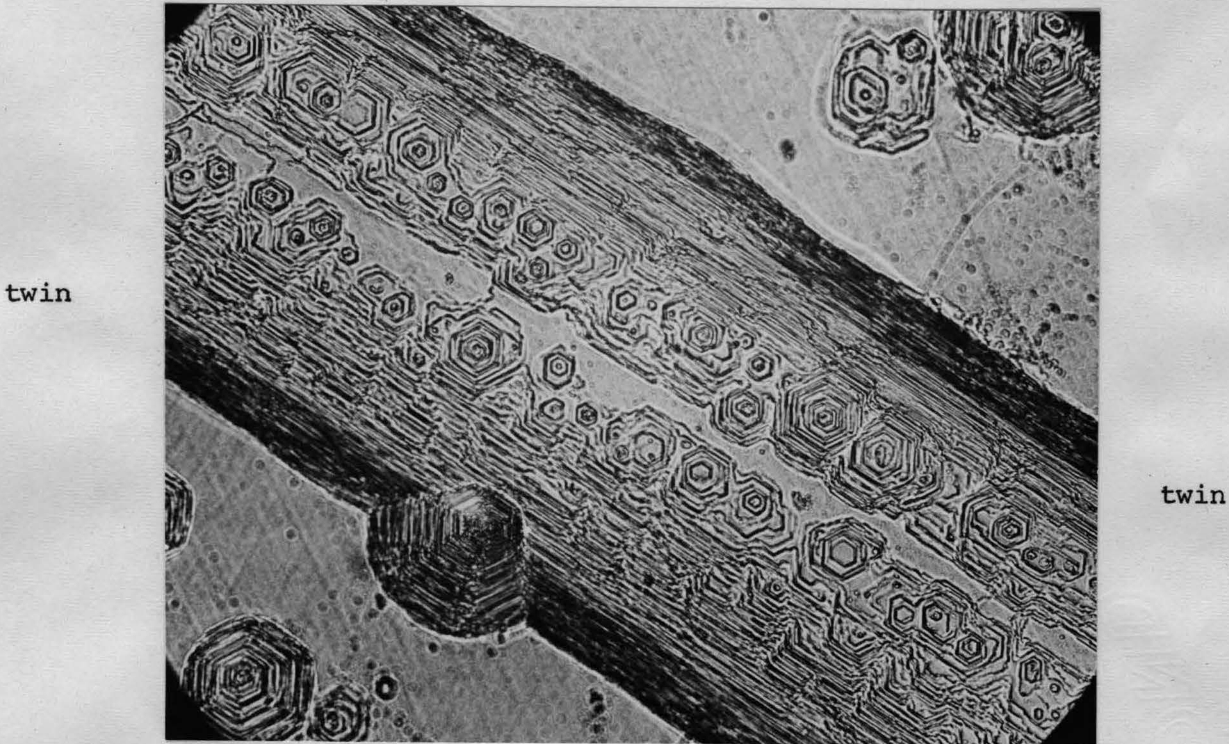

Fig. 36(b) - Optical micrograph of shallow evaporation pits at the base of deformation twins (500x).

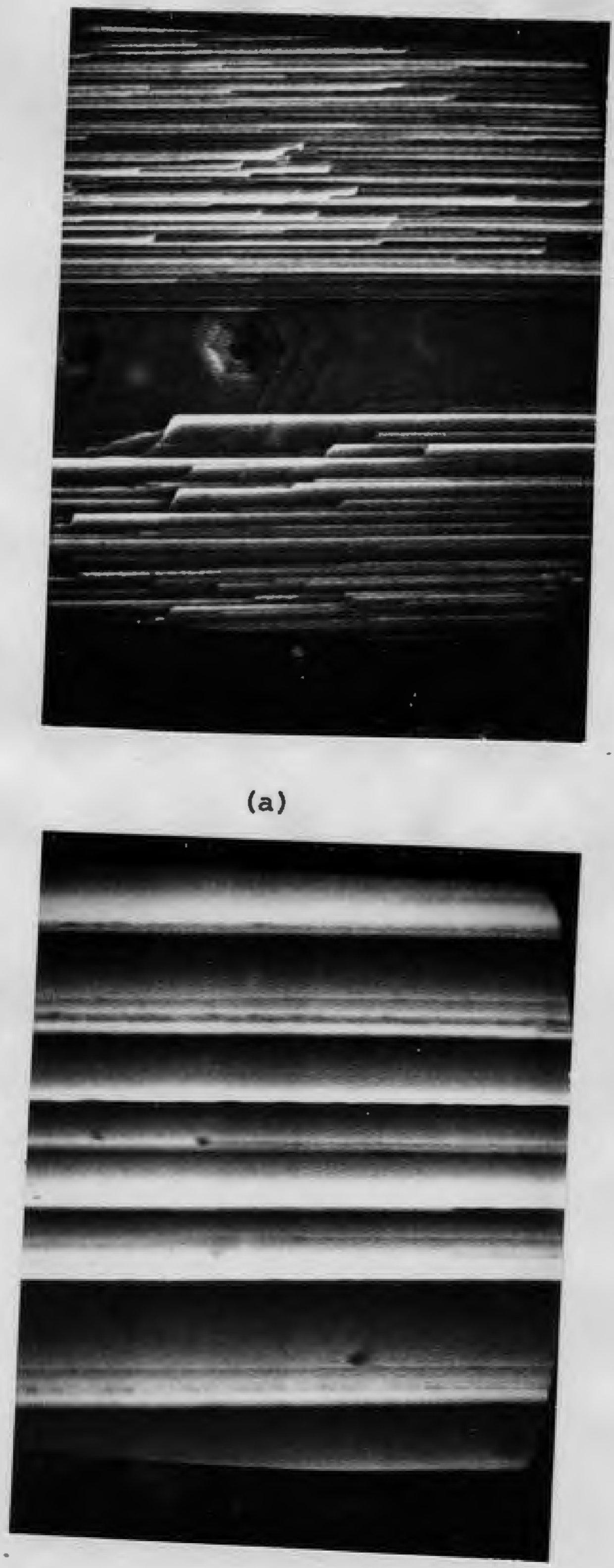

(a)

(b)

Fig. 37 - S.E.M. of evaporation ledge structure on an evaporated deformation twin. (a) (2,000x, $\beta = 35°$); (b) (10,000x, 3 = 35°).

Fig. 38 - Optical micrograph of evaporation pits at a sub-grain boundary (200x).

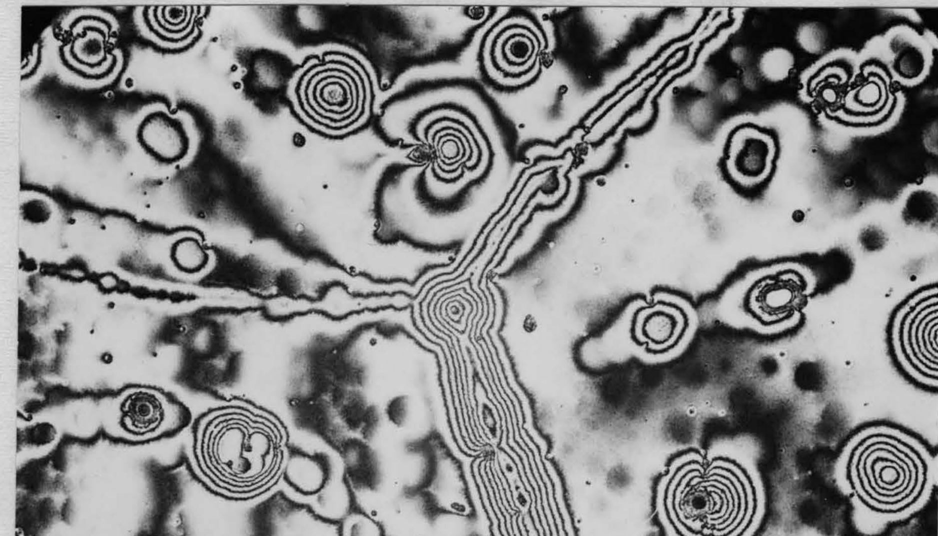

Fig. 39 - Interference micrograph of a nodal intersection of sub-grain boundaries after evaporation (200x).

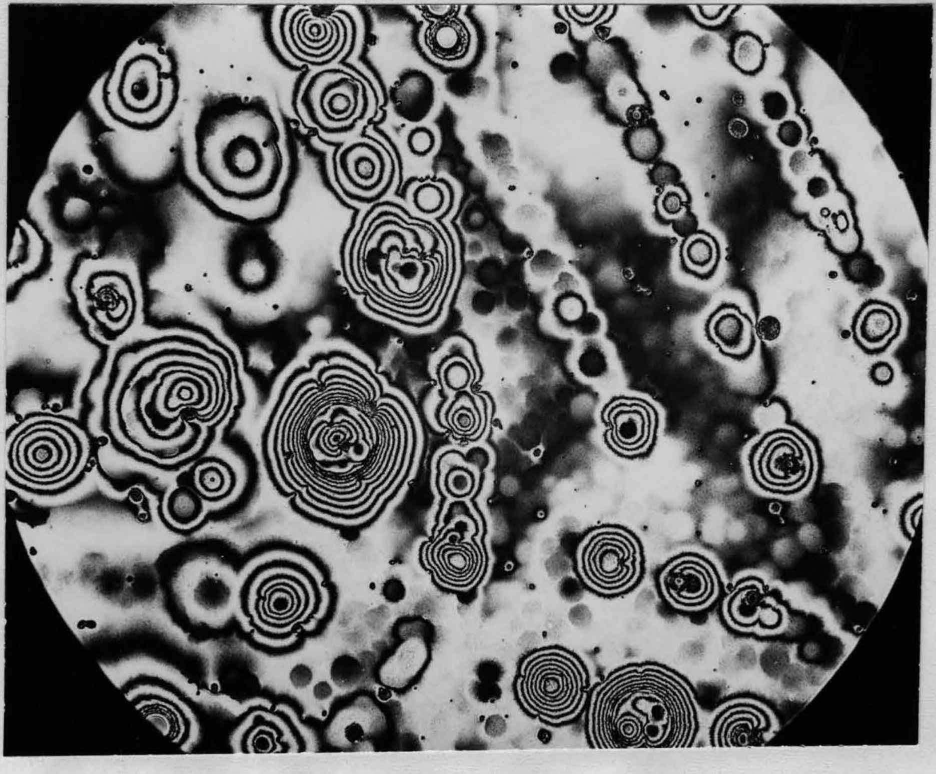

Fig. 40 - Interference micrograph of evaporation pits along glide bands. (200x).

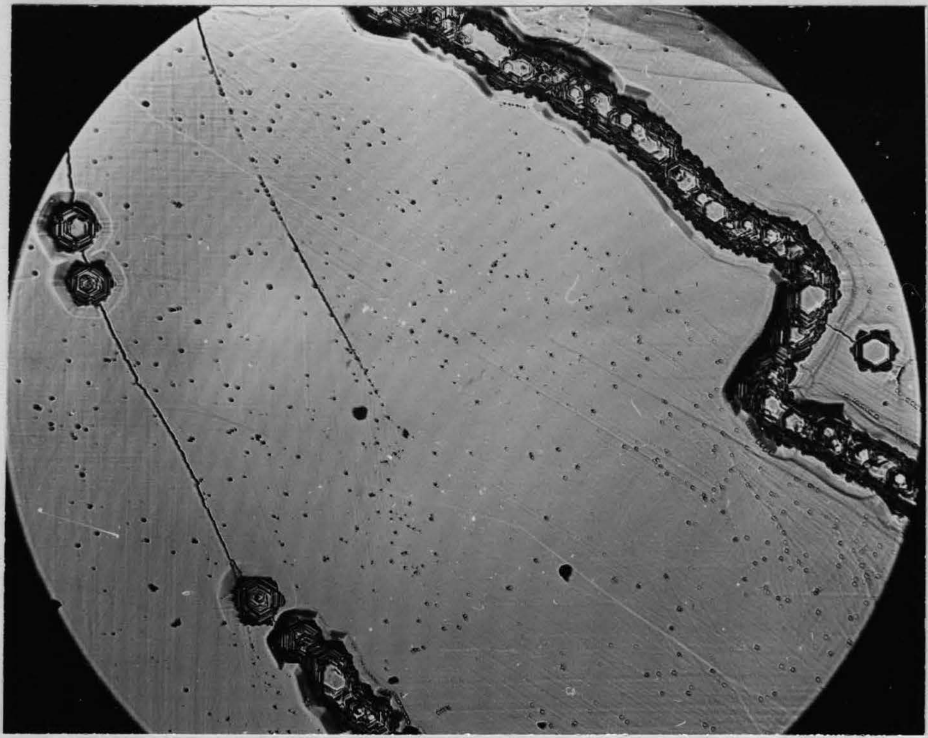

Fig. 41 - Optical micrograph of evaporation pits along cleavage steps (100x).

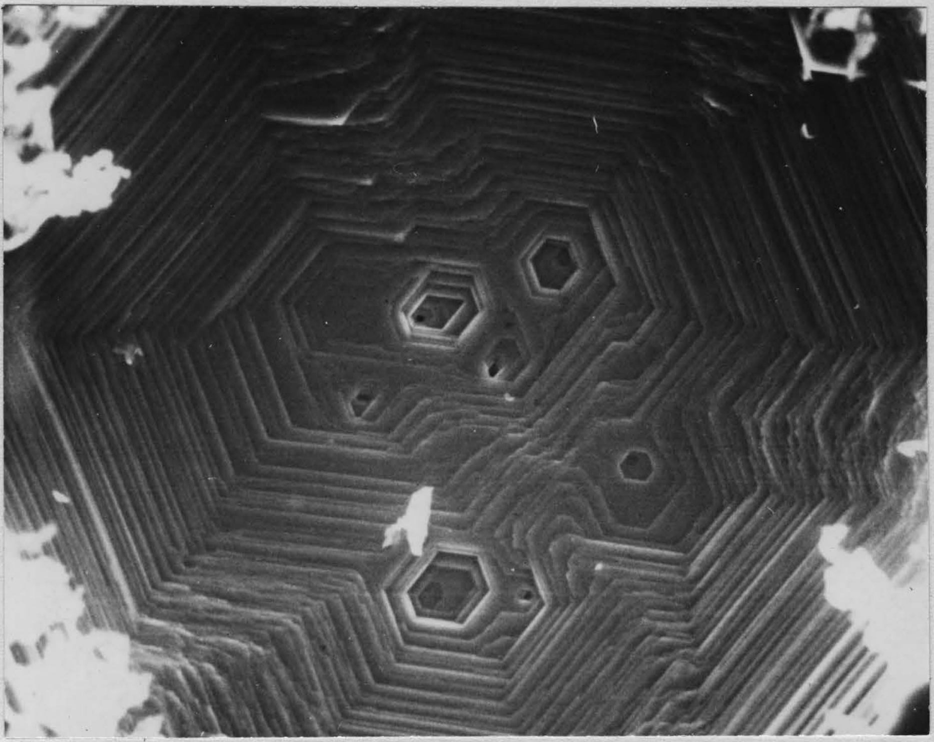

Fig. 42 - S.E.M. of deep, steep-sided evaporation "pits" on contaminated surface. (500x, $\beta = 35°$).

Fig. 43 - Optical micrograph of asymmetric pit (500x).

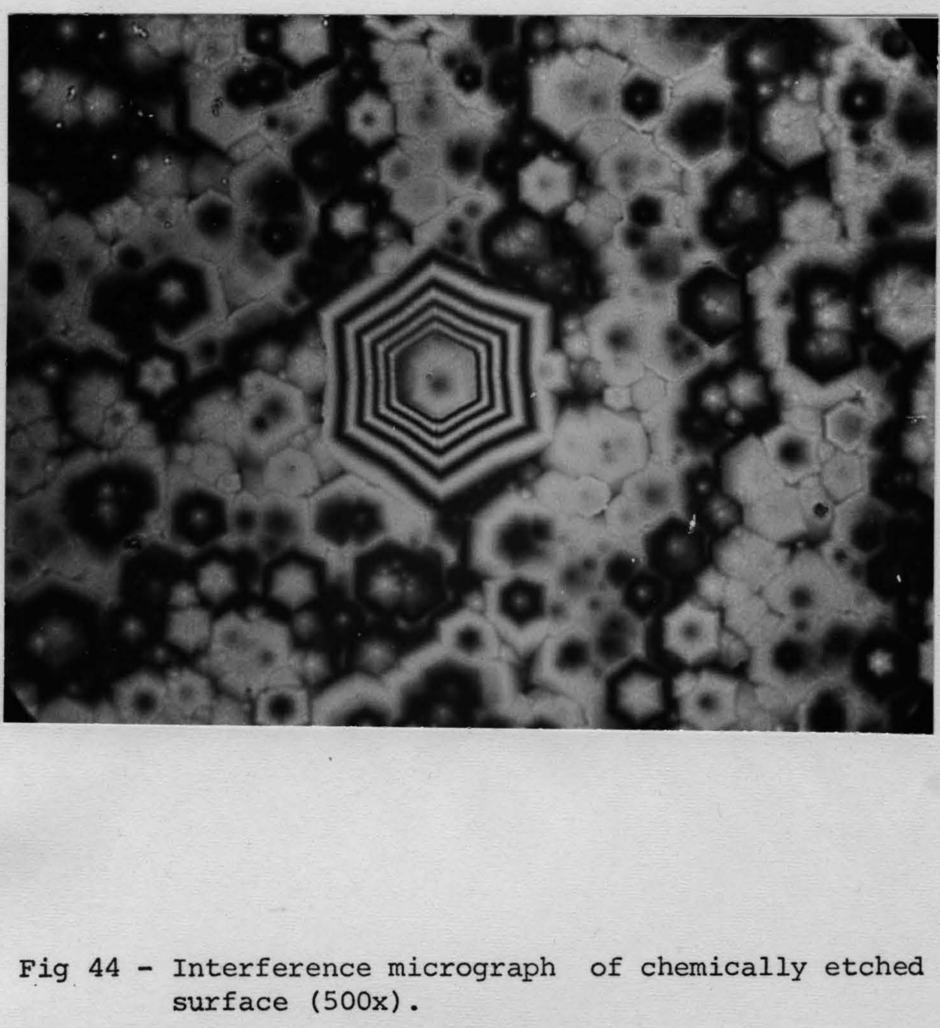

Fig 44 - Interference micrograph of chemically etched surface (500x).

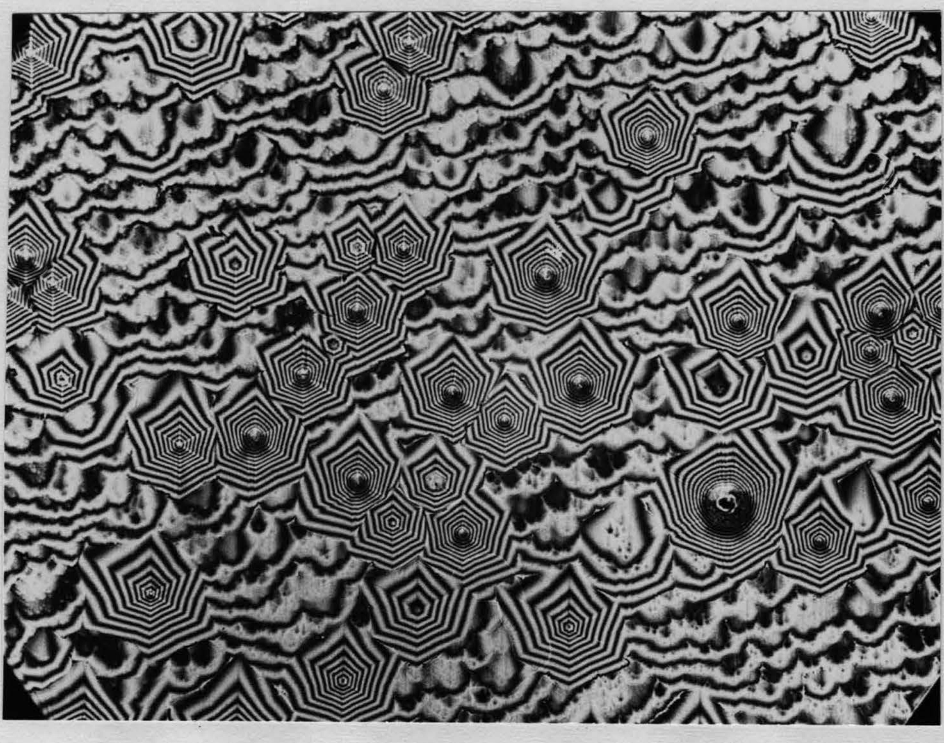

Fig. 45(a) - Interference micrograph showing high chemical etch pit density on low purity sample (200x).

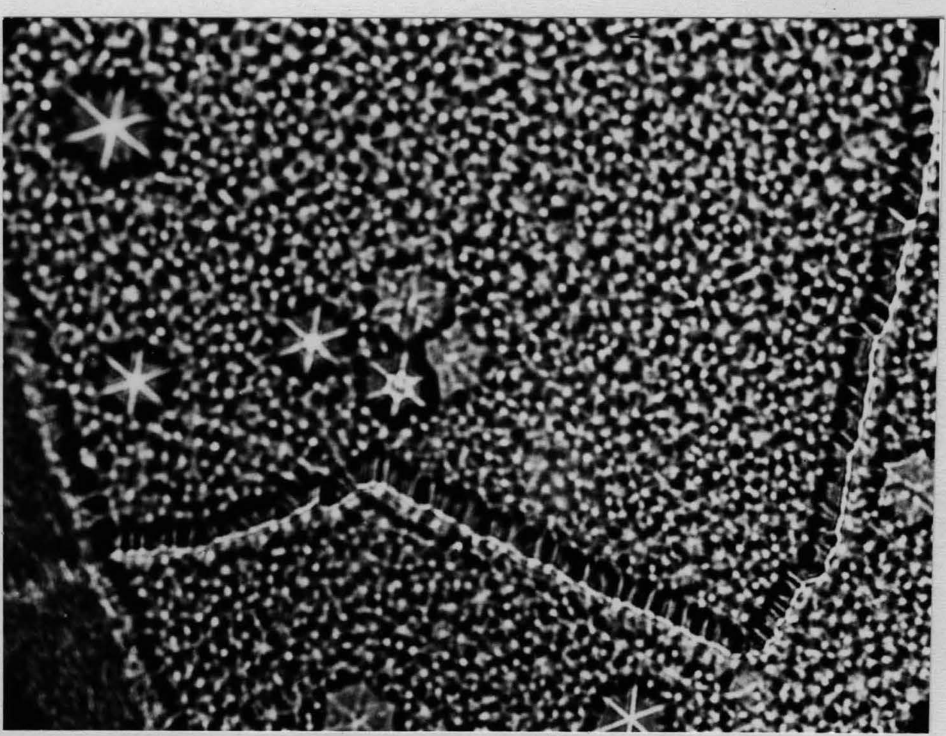

Fig. 45(b) - Optical micrograph showing low chemical etch pit density on high purity sample (200x).

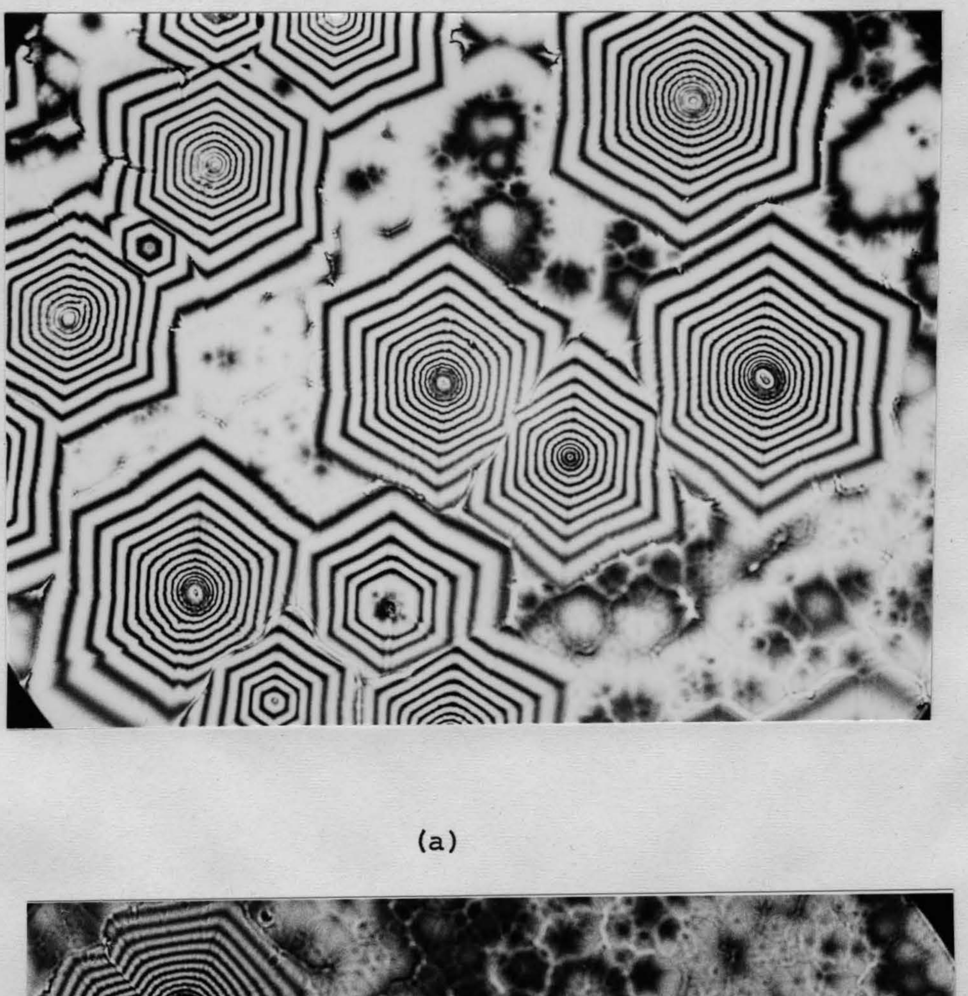

(a)

(b)

Fig. 46 - Interference micrographs showing chemical etch pit morphology on (a) low purity sample; (b) high purity sample. (500x).

(a)

(b)

Fig. 47 - Optical micrographs of cleavage steps (a) before (b) after chemical etching. (100x).

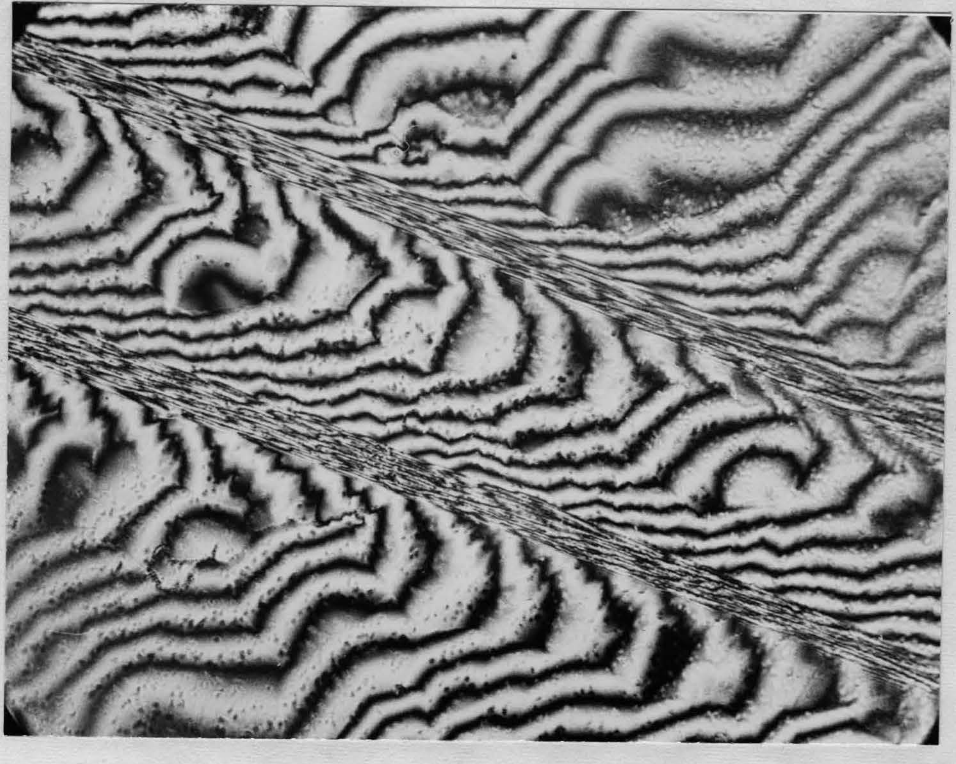

Fig. 48 - Interference micrograph of chemically etched mechanical twins (500x).

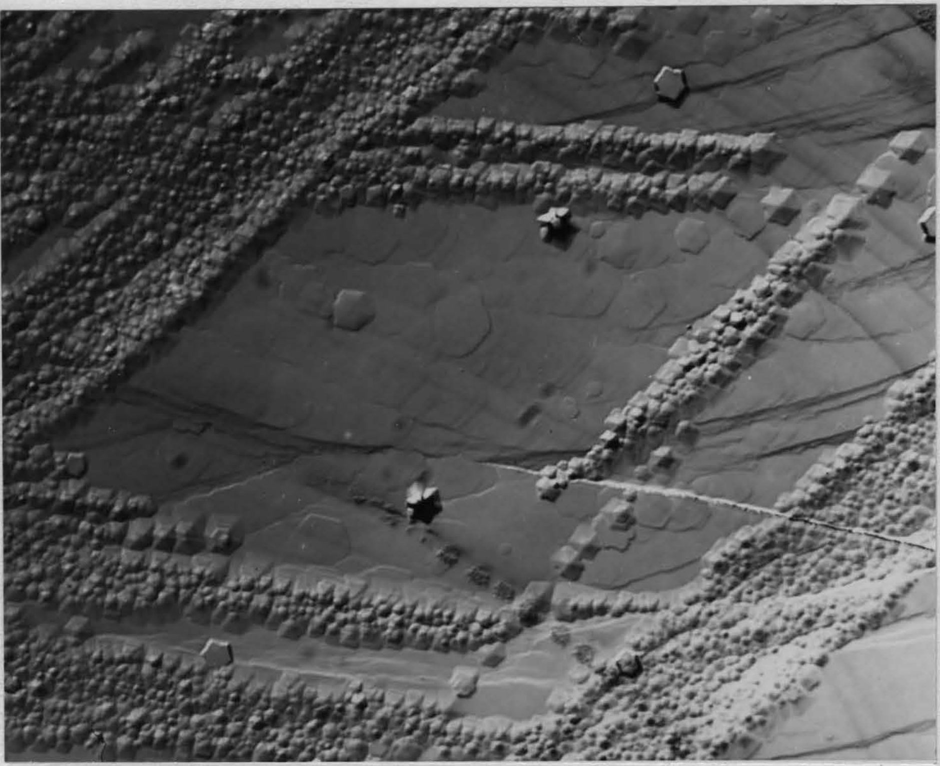

Fig. 49 - Optical micrograph showing chemical etch pits along glide bands (100x).

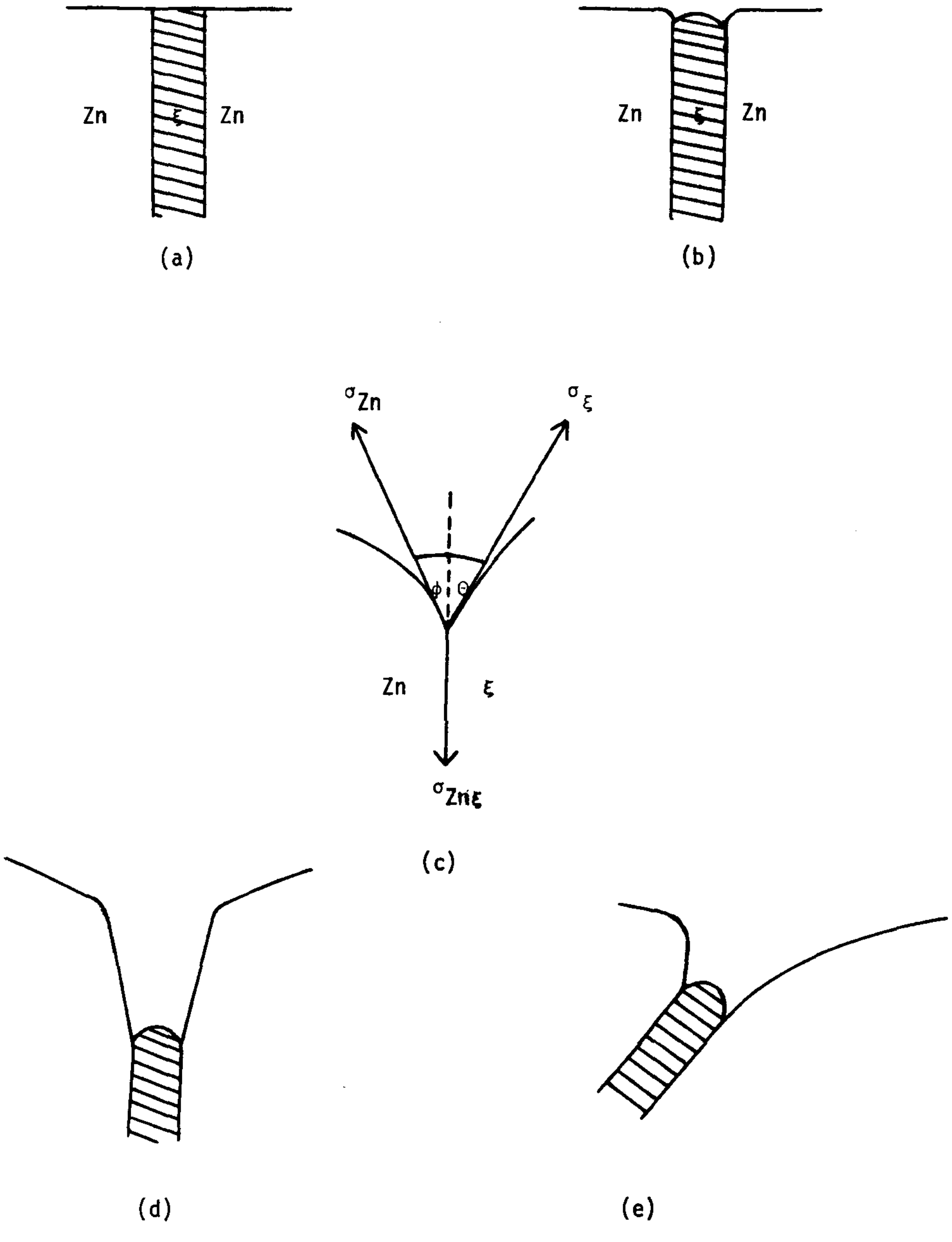

FIG. 50 - Thermal grooving at non-coherent precipitate boundaries

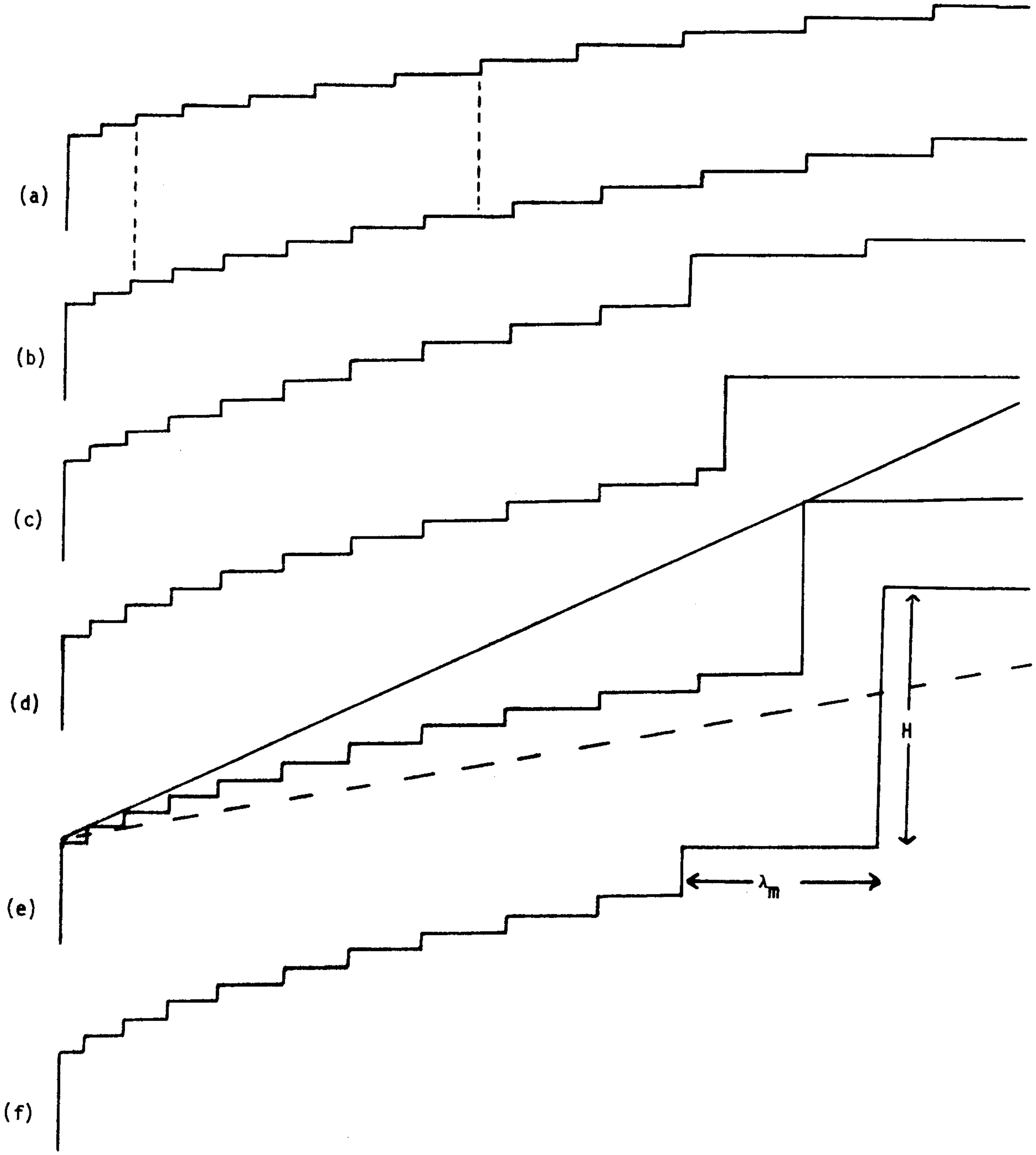

FIG. 51 - A schematic representation of the formation of a macroscopic ledge from a train of monatomic steps.

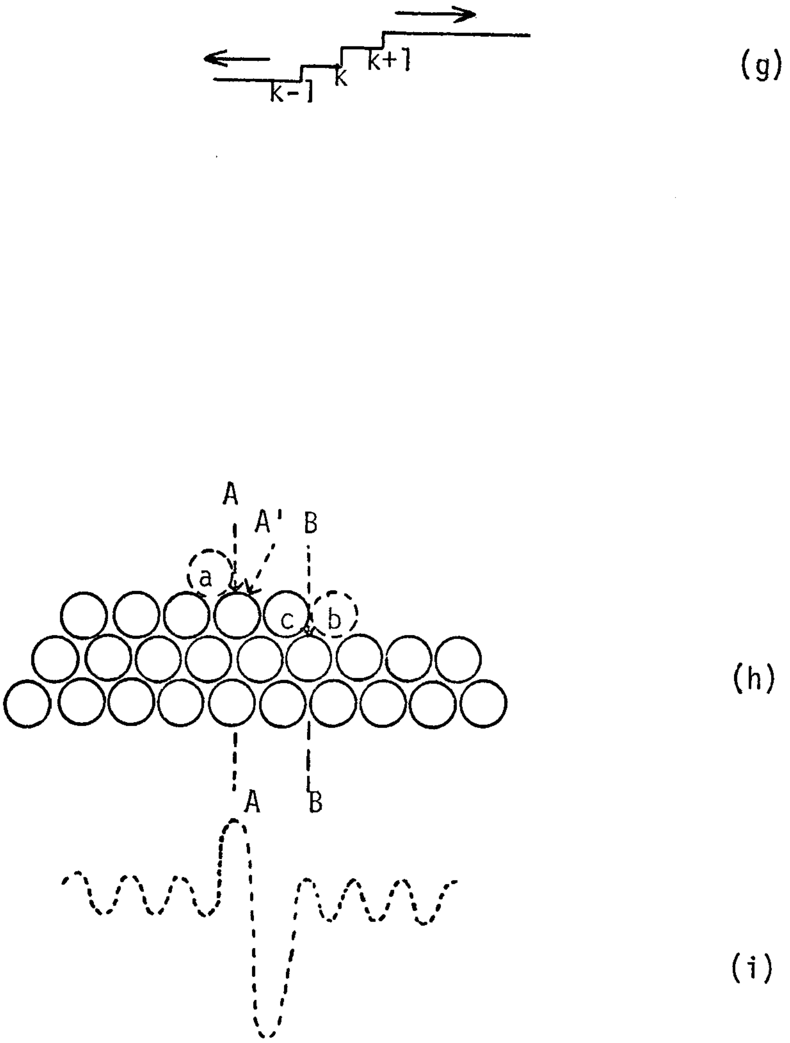

FIG. 51 - (continued)

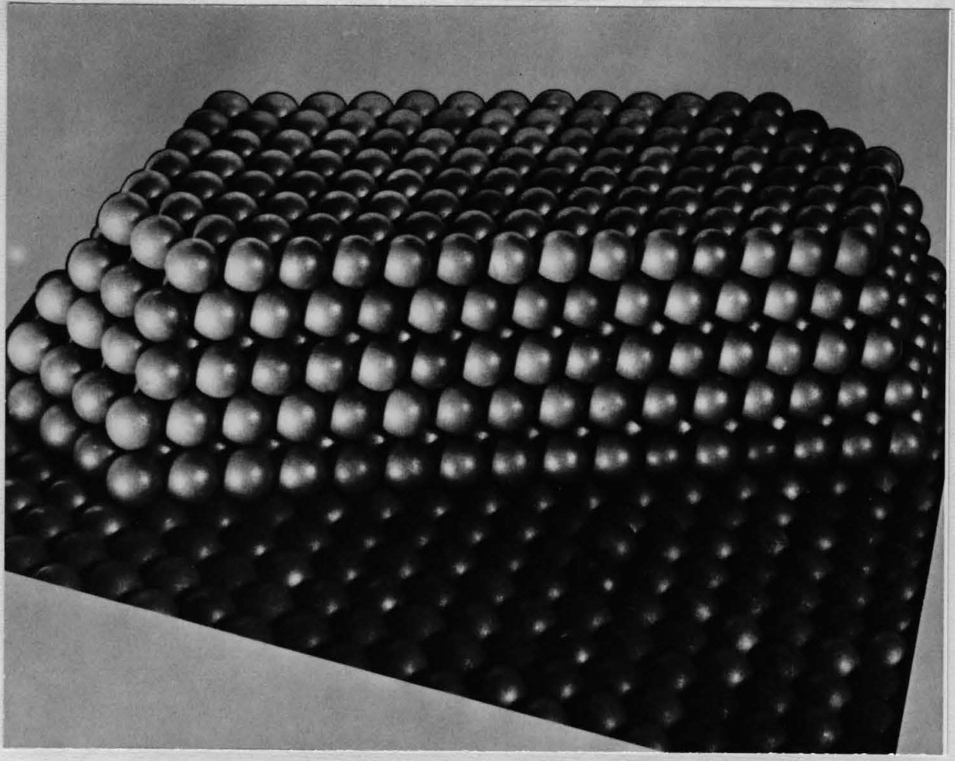

(a)

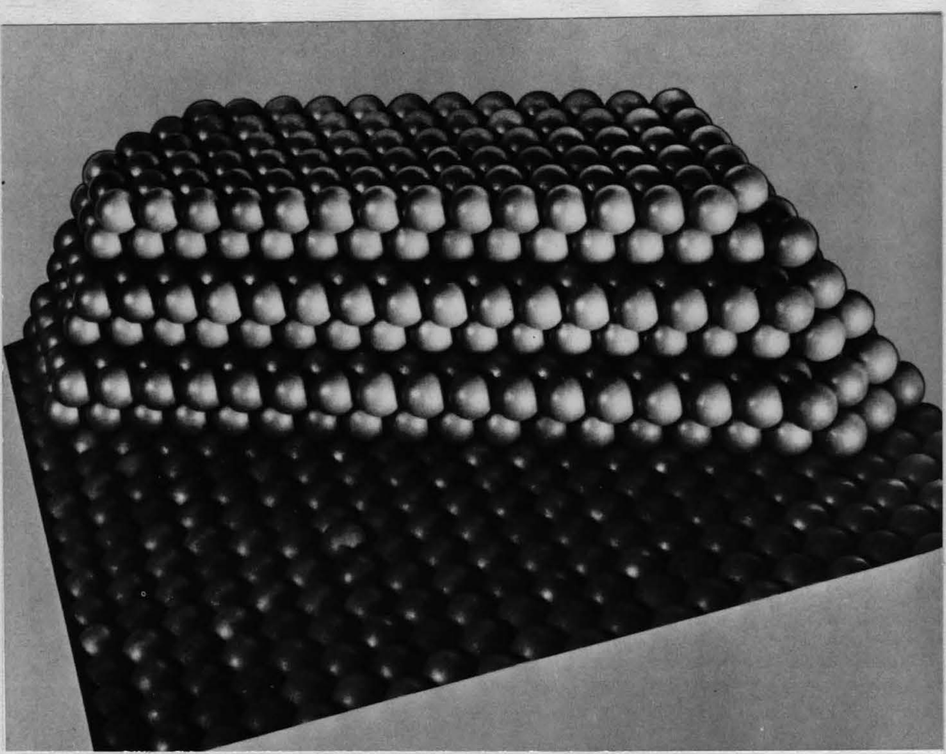

(b)

Fig. 52 - Ball model of (10$\bar{1}$1) ledge on (0001) terrace with the surface atoms having coordination numbers (a) 8; and (b) 6.

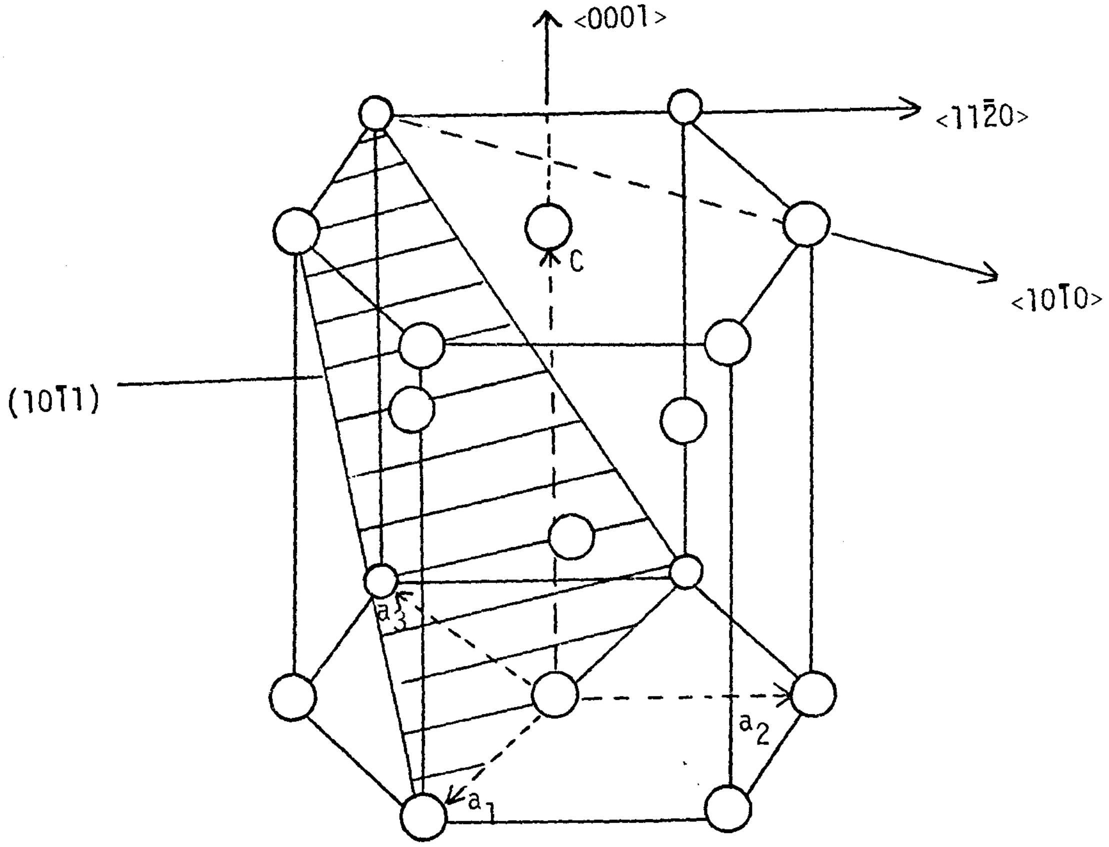

FIG. 52(c) - Hexagonal close-packed cell.

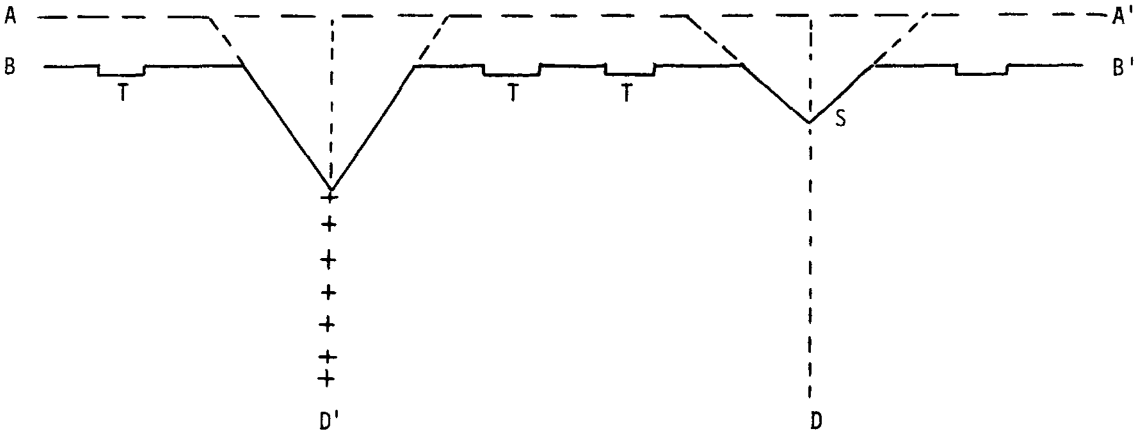

(a)
(0001) orientation

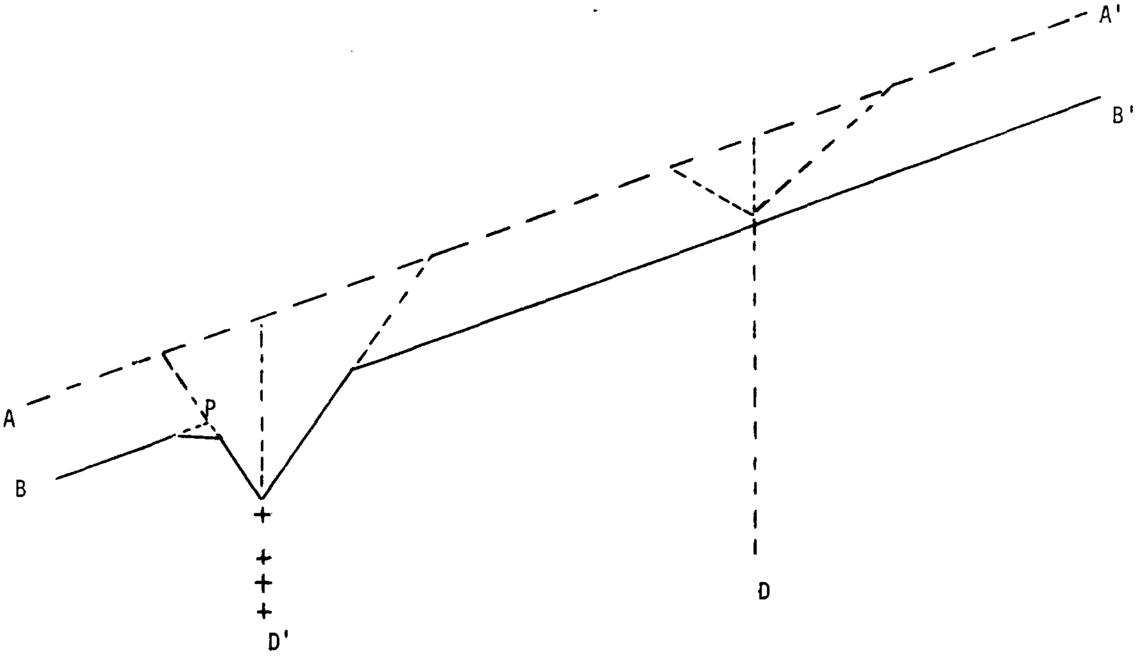

(b)
vicinal orientation

FIG. 53 - A schematic model of an evaporating surface

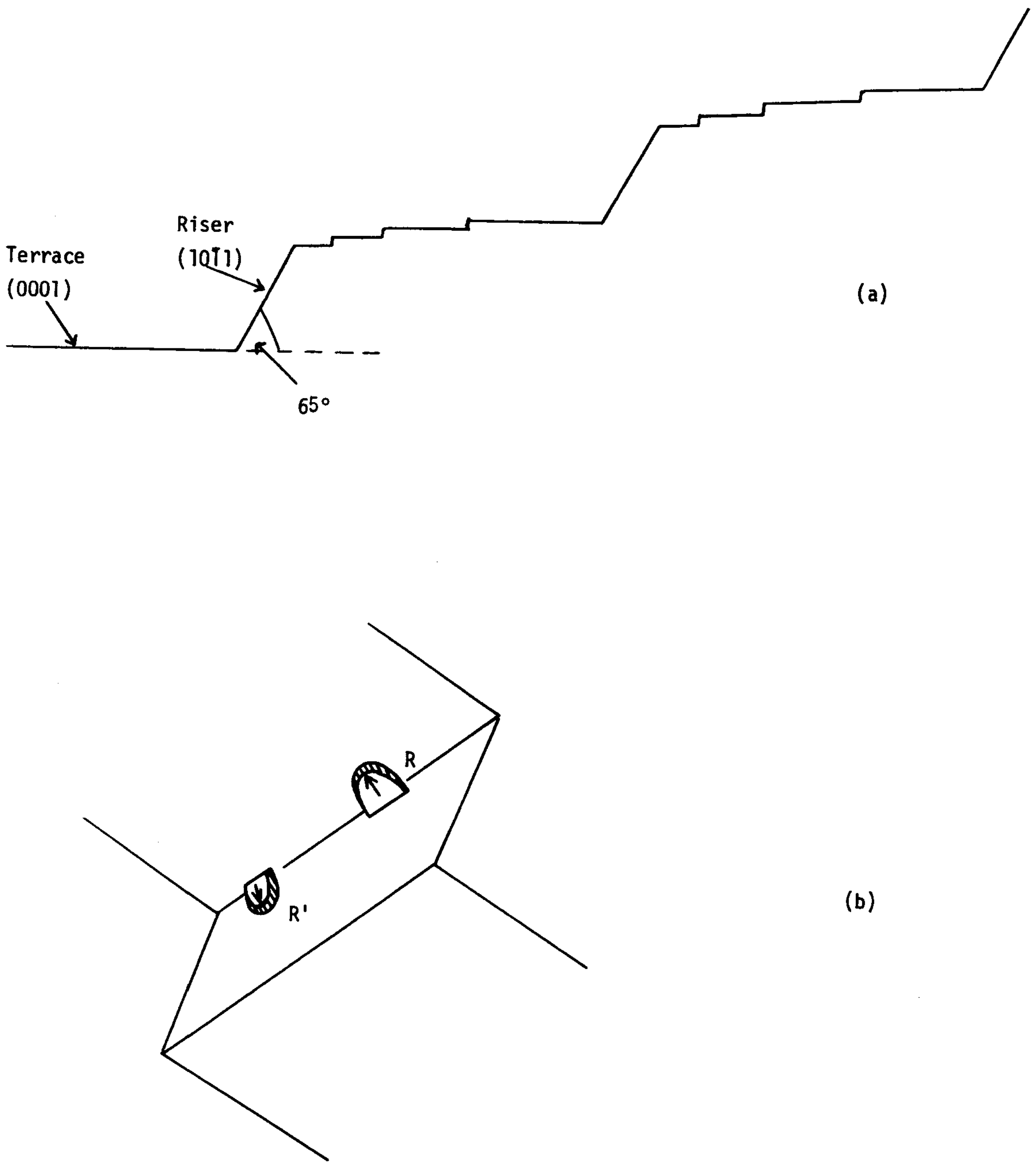

FIG. 54 - A schematic model for evaporation of a faceted surface

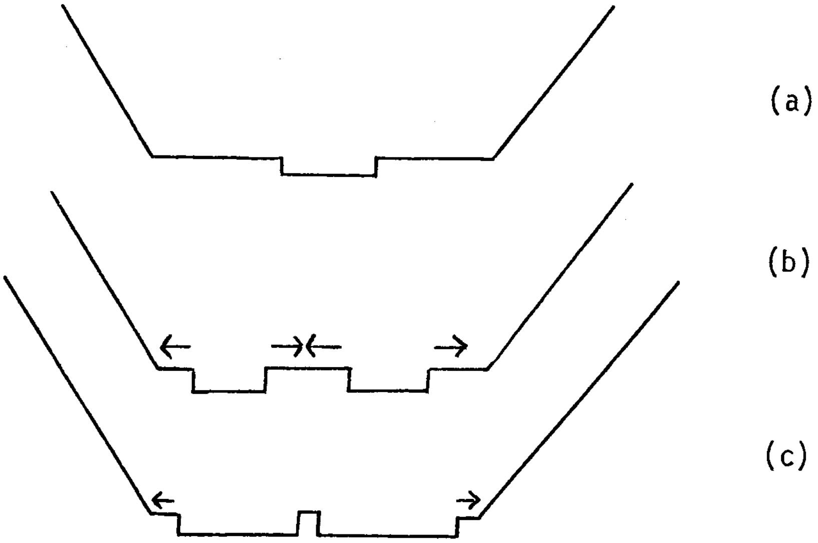

FIG. 55 - Monatomic step motion on ledge riser

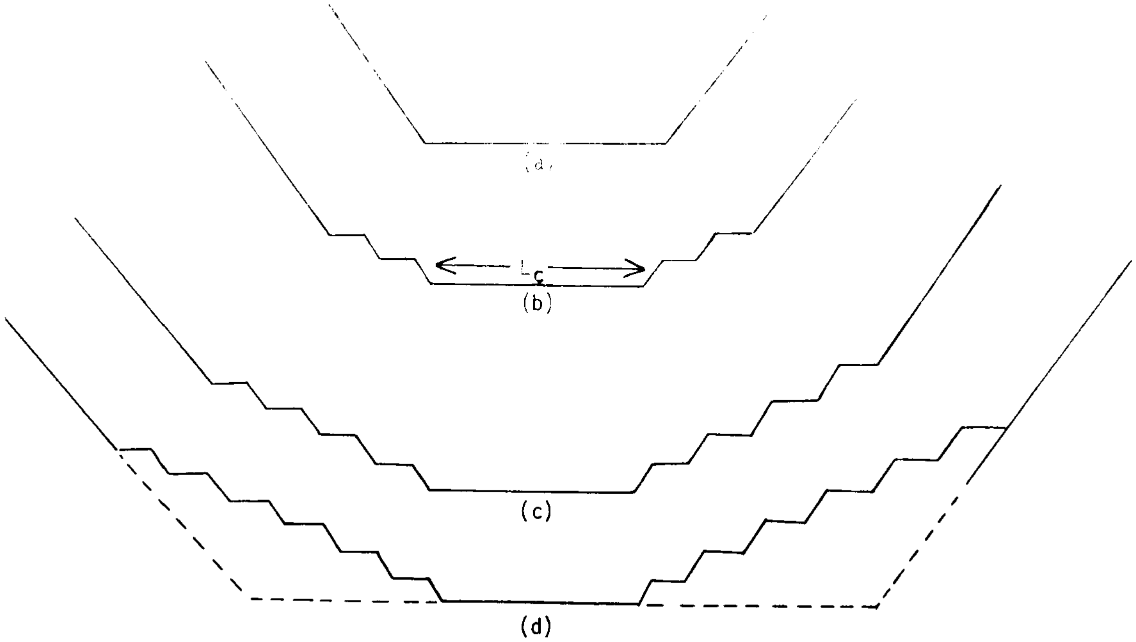

FIG. 56 - Macrokink formation in macroscopic ledge

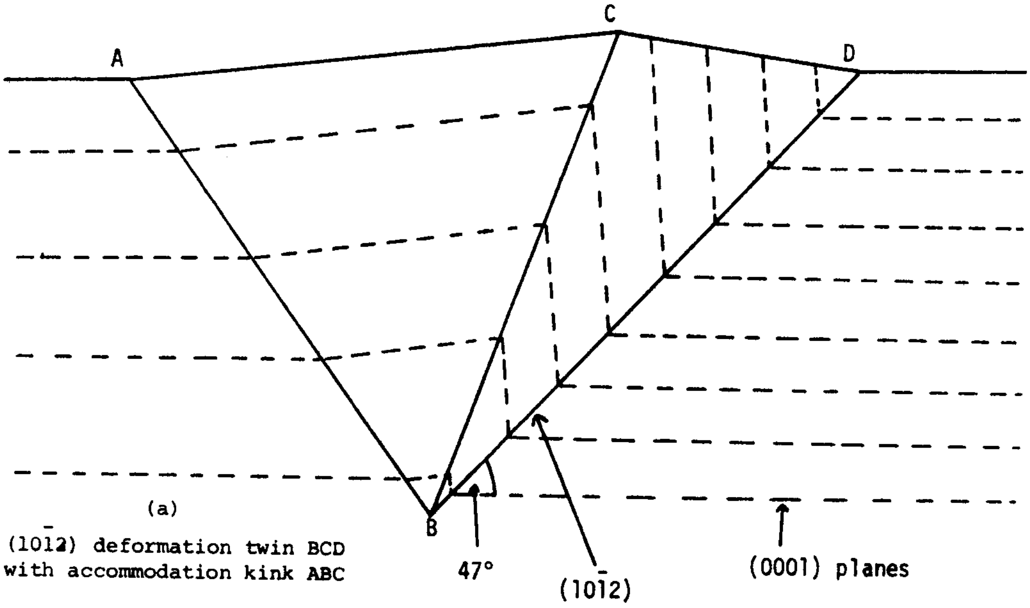

(a)

$(10\bar{1}2)$ deformation twin BCD
with accommodation kink ABC

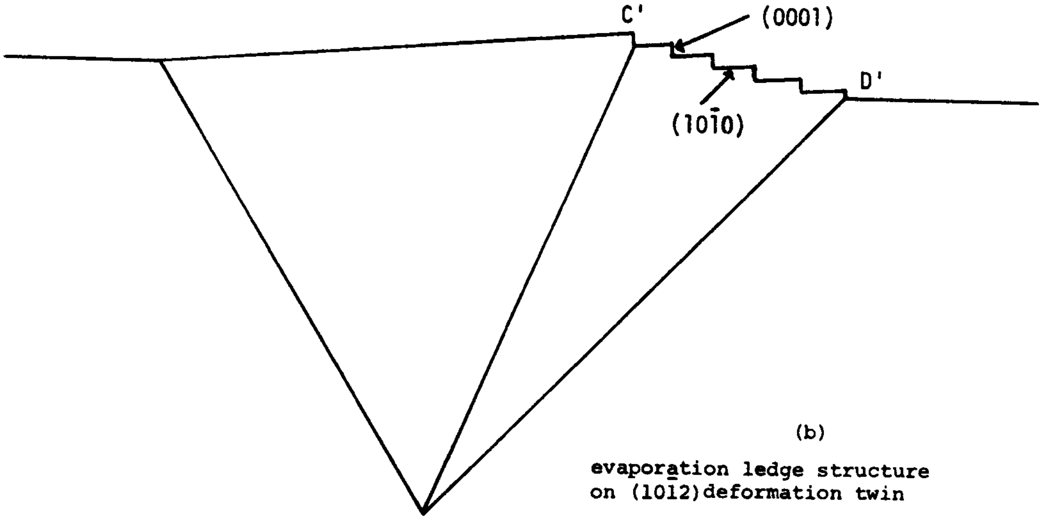

(b)

evaporation ledge structure
on (1012)deformation twin

FIG. 57 - Evaporation at $(10\bar{1}2)$ deformation twin